Structure-Function Studies of Agonist Binding to the Muscle-Type Nicotinic Acetylcholine Receptor and the Development of a Trifunctional Non-Competitive Antagonist Suitable for Activity-Dependent Profiling

by

Mathew C. Tantama

B.S. Chemistry, B.S. Mathematics
University of North Carolina at Chapel Hill, 2001

Submitted to the Department of Chemistry
in Partial Fulfillment of the Requirements for the
Degree of Doctor of Philosophy in Biological Chemistry

at the

Massachusetts Institute of Technology

July 2008

Signature of Author.....
Department of Chemistry
June 27, 2008

Certified by.....
Stuart S. Licht
Assistant Professor of Chemistry
Thesis Supervisor

Accepted by.....
Robert W. Field
Chairman, Departmental Committee on Graduate Students

ARCHIVES

This doctoral thesis has been examined by a Committee of the Department of Chemistry as follows:

Professor JoAnne Stubbe..... .....
Chairperson

Professor Stuart Licht..... .....
Thesis Supervisor

Professor Sarah O'Connor... .....
Committee Member

Structure-Function Studies of Agonist Binding to the Muscle-Type Nicotinic Acetylcholine Receptor and the Development of a Trifunctional Non-Competitive Antagonist Suitable for Activity-Dependent Profiling

By

Mathew C. Tantama

Submitted to the Department of Chemistry
in July, 2008 in Partial Fulfillment of the Requirements for the
Degree of Doctor of Philosophy in Biological Chemistry

ABSTRACT

The muscle-type nicotinic acetylcholine receptor (AChR) is a ligand-gated ion channel required for fast synaptic transmission at the neuromuscular junction. It is the archetype of the Cys-Loop superfamily of receptors and a prototypic allosteric protein. The muscle-type AChR has two distinct transmitter binding sites found in the extracellular ligand-binding domain. When acetylcholine binds these sites, a series of still unresolved conformational changes occur, leading to opening of the transmembrane pore over 40 Å distant from the binding sites. High resolution structures of the intact receptor and the acetylcholine binding protein have provided greater insight into the structural basis of the allosteric mechanism coupling agonist binding and pore opening. However, comprehensive models of the agonist-bound receptor in its closed and open states are still not available. In particular, the details describing the conformation of binding site residues and the dynamics of their interactions with agonists and competitive antagonists are still under investigation. These details are of particular importance to the design of AChR agonists, partial agonists, and competitive antagonists which may have therapeutic potential for treating neuromuscular and neurological pathologies. Using single-channel electrophysiology we investigated details of the agonist-bound open-state transmitter binding sites. Using a series of structurally related organic cations, we observed a structure-activity relationship that suggests cation-π binding interactions are important for open-state affinity. We also conducted a structure-function study to measure kinetic and thermodynamic differences in agonist binding to the two different transmitter binding sites in both the closed and open states. We observed that the two binding sites have unequal affinities for the agonist choline in the closed state and equal affinities in the open state. The state-dependent difference in affinities suggests that binding determinants from the α subunits predominantly determine open-state choline affinity at each site. In the last chapter, we exploit the state-dependent affinities of small molecules for the AChR to develop a probe for live-cell labeling. The ability of a non-competitive antagonist incorporating state-dependent AChR binding, photoreactivity, and click chemistry moieties was characterized electrophysiologically, and state-dependent photolabeling of AChRs in live cells was demonstrated. A probe with these characteristics is suitable for investigating the activity-dependent changes in AChRs associated with the complex synaptic changes associated with neuromuscular and neurological disorders.

Thesis Supervisor: Stuart Licht
Assistant Professor of Chemistry

Acknowledgments

First and foremost, I thank my family and friends for their unending support.

I thank my advisor, Professor Stuart Licht, for his patience, guidance, and mentorship which have been invaluable. I thank the members of our lab and floor for making my time in graduate school enjoyable. I thank the members of my committee, Professors JoAnne Stubbe, Sarah O'Connor, Dan Kemp, and John Essigmann, for their generosity of time and advice. I thank Professor Cathy Drennan for years of encouragement and advice. I thank Susan Brighton who has been positive and supportive force since my first day at MIT.

I also thank the scientific mentors whose guidance led me to MIT. I thank Patricia Lovarco and Gregg Bantz for cultivating my interests in science and math. I thank Professor John Bethea for his incredible mentorship and for providing an early research experience that largely inspired my academic and career goals. I thank Professor Terry Van Dyke, Dr. Dawn Tolbert, Dr. Andrew Xiao, and Dr. Phiroze Sethna for providing me with wonderful undergraduate research experiences. In addition to her friendship, I thank Dr. Christina Rudzinski for encouraging me to pursue a graduate degree.

Table of Contents

Chapter I. Introduction

I.A Summary

Nicotinic acetylcholine receptors (AChRs) are ligand-gated ion channels (LGICs) essential for signal transduction at the neuromuscular junction and at the synapses of the central nervous system (*1-4*). LGICs are integral membrane proteins with two allosterically linked functions (*2, 5*). LGICs act both as receptors for signaling molecules and gated ion channels for control of ion flux across membranes. In recent decades, data from cryoelectron microscopy (*6*) and x-ray crystallography (*7*) have produced a more detailed understanding of the structural basis of AChR function. However, many molecular details pertaining to structural dynamics during ligand binding and gating of the ion channel are still unknown. In this thesis, structure-function studies of the muscle-type AChR from the adult mouse were performed using single-channel electrophysiology. In Chapters II and III, structural dynamics involved in agonist binding at the transmitter binding sites were investigated. In Chapter IV, basic knowledge of non-competitive antagonism was used to design a chemical probe for neurobiological applications. In this first chapter, an introduction to AChR structure and function is given, and a brief introduction to single-channel electrophysiology is provided.

I.B Ion Channels at Fast Chemical Synapses

Ion channels facilitate the fast transduction of an extracellular chemical signal into a cellular response. Ion channels are pore-forming, integral membrane proteins that mediate the flow of ions across a cell membrane. In excitable cells, such as neurons and myocytes, the opening or closing of ion channels can cause a change in membrane potential. The change in membrane potential initiates a cascade of events leading to an amplified cell response on fast timescales. In contrast, signaling pathways involving second messengers are considered slow. Ion channels of excitable cells can be broadly categorized as voltage-gated or ligand-gated (**Figure I.1**) (*8*).

Voltage-gated channels include sodium (Na_v), potassium (K_v), and calcium (Ca_v) channels, and they comprise a homologous gene superfamily (*8, 9*). Voltage-gated channels contain a charged membrane spanning region, the voltage sensor. The voltage sensor changes conformation in response to changes in membrane potential. Movement of the sensor leads to opening or closing of the ion channel by an allosteric mechanism.

LGICs mediate chemical-to-electrical signal transduction at fast synapses. Binding of neurotransmitters to an LGIC is allosterically linked to the conformation of the ion channel pore. There are three homologous LGIC gene superfamilies. First, the P2X purinergic receptor family consists of ATP-sensitive ion channels. P2X receptors are thought to be trimeric (*10*). Second, the ionotropic glutamate receptor family includes N-methyl-D-aspartate receptors (NMDARs), α-amino-3-hydroxy-5-methyl-4-isoxazolepropionic acid receptors (AMPARs), and kainate receptors (KARs). These receptors are tetrameric. Third, the "cys-loop" superfamily includes AChRs (**Figure I.2**), 5-hydroxytryptamine receptors (5-HT_3Rs), γ-amino-butyric acid receptors ($GABA_A$Rs), and glycine receptors (GlyRs). These receptors are pentameric. The name "cys-loop" refers to a 13 amino acid loop flanked by a disulfide bridge that is structurally conserved across the family.

I.C Acetylcholine Receptor Biology

Physiologically, the action of muscle-type AChRs at the neuromuscular junction provides a model for synaptic transmission (**Figure I.3**). When an impulse reaches a motor neuron terminal, the presynaptic action potential causes local calcium influx. The presynaptic nerve terminal is densely populated by acetylcholine-laden vesicles. The local calcium influx causes vesicles to fuse to the presynaptic membrane, releasing acetylcholine into the neuromuscular junction. The postsynaptic, muscle-cell membrane is highly folded. Muscle-type AChRs are found on the apices of the folds, with densities of 10,000 AChRs per 1 μm^2. Released acetylcholine binds the receptors, and AChR channels open. Influx of sodium ions through the open AChRs causes local depolarization of the membrane. The depolarization is propagated by voltage-gated sodium channels. The propagated postsynaptic action potential causes opening of voltage-gated calcium channels and subsequent calcium release from the sarcoplasmic reticulum. This calcium release initiates muscle contraction.

Each AChR is made up of five homologous subunits, and seventeen different subunit homologs have been identified. There are ten α subunits named α1–α10. All α subunits contain a vicinal disulfide bridge between adjacent cysteines in the Loop C region, described in more detail below. These subunits contribute the principal components to the transmitter binding sites. Non-α subunits include the β1–β4, δ, ε, and γ subunits.

Neuronal AChRs are expressed at synapses throughout the central nervous system (*11, 12*). Homomeric neuronal AChRs are made up of α subunits. Heteromeric neuronal AChRs can be made up of α subunits only or of both α and β subunits.

Muscle-type AChRs are expressed in the peripheral nervous system. They are either fetal-type ($\alpha_2\beta\delta\gamma$) or adult-type ($\alpha_2\beta\delta\varepsilon$) channels. The muscle-type AChR is the archetype of cys-loop receptors. The muscle-type AChR was essentially the first LGIC identified and characterized (*13, 14*). Many biochemical, electrophysiological, and structural ion channel techniques were developed while studying this receptor (*15, 16*).

Functional AChRs exist in closed, open, or desensitized conformations. The closed AChR state predominates in the absence of agonist. It is a non-conducting conformation, and it is characterized by low agonist affinity compared to the other conformations. The open state is an ion-conducting conformation. It has higher agonist affinity compared to the closed AChR. The difference between closed-state and open-state affinities favors opening of the AChR in the presence of agonist. However, prolonged agonist exposure favors the desensitized AChR state. This conformation is non-conducting and has high agonist affinity. Typically, the term "gating" refers to transitions between the closed and open states.

I.D Structures of the Acetylcholine Receptor and Binding Proteins

Cryoelectron microscopy is currently the only source of images of the membrane-bound, intact AChR. LGICs have proven refractory to x-ray crystallography. However, AChRs from electric rays and electric eels are particularly amenable to high-resolution cryoelectron microscopy. The electrical current-generating organs of these fish are highly enriched in AChRs. These receptors can be frozen in tubular, crystalline arrays for electron microscopy (*17*). The most recent images provide a 4 Å resolution model for the closed, agonist-free *Torpedo marmorata* muscle-type AChR (*6, 18*). Secondary structure assignments corroborate decades of biochemistry and electrophysiology concerning the structure of the ligand binding domain and ion conduction pore (*15, 16, 19*). Cryoelectron microscopy has also provided the only images of the open AChR. By freezing receptors milliseconds after acetylcholine exposure, a 25 Å resolution model of the open receptor was obtained (*20*). However, a complete atomic-resolution image of the intact AChR is still not available.

Recently, atomic-resolution models of acetylcholine binding proteins (AChBPs) have become available (**Table I.1**). The AChBP is a soluble homolog of the AChR extracellular, ligand-binding domain. It is a pentamer with similar secondary structure as the AChR ligand-binding domain. The AChBP has a cys-loop, and several binding site residues and structures are conserved between the AChBP and AChR. The *Lymnaea stagnalis* snail AChBP was first discovered in 2001 (*7, 21*). Since then, structures of AChBPs from different species have been solved by x-ray crystallography (*7, 22-31*). Models are available for AChBPs in complex with a variety of agonists and antagonists. These models have been used to infer details about the conformation of residues in the AChR ligand-binding domain, and AChR homology modeling has been conducted (*32-37*). Recently, an atomic-resolution x-ray structure of the extracellular ligand-binding domain of the AChR α-subunit was obtained. This model confirmed the structural homology between the AChBP and AChR ligand binding domain (*38*).

There are several caveats to the use of AChBP models. The AChBP is a snail protein with a distant relationship to the mammalian AChR. It lacks an ion channel domain, and it shares only approximately 20% sequence identity to the ligand-binding domain of AChRs. It is also not clear to which AChR conformational states the AChBP structures actually correspond. AChBP models can be classified into two types. Structures of apo-AChBP or antagonist-bound AChBP are compared to the closed-state AChR ligand-binding domain. Structures of agonist-bound AChBPs are compared to the desensitized-state AChR; however, the distinction between the open state and desensitized state is not clear.

Atomic-resolution structural models of all the functional states of the intact AChR are still needed. Comparison of agonist-free, closed-state models and agonist-bound, desensitized-state models have provided some key insights described below. However, there are currently no high-resolution models of the agonist-bound closed AChR and agonist-bound open AChR. These are necessary to pinpoint gating structural changes and to define the allosteric pathway.

I.E General Description of the AChR Structure

The 4 Å resolution cryoelectron microscopy structure of the intact *Torpedo* AChR provides a model for muscle-type receptors (*6*). Muscle-type AChR subunits are arranged clockwise in the order αβδαγ (αβδαε for the adult-type receptor). They are positioned pseudo-symmetrically around the ion conduction pathway (**Figure I.2A**). The *Torpedo* AChR is

homologous to the adult mouse muscle-type AChR used for experimental studies described in this thesis. The *Torpedo marmorata* α-subunit (accession number P02711) and the *Mus musculus* α-subunit (accession number P04756) are 79% identical and 91% similar. **Figure I.4** shows an alignment of the adult mouse subunits annotated according to the homologous *Torpedo* structure. The N-terminus signal sequence is removed in the mature AChR. **Figure I.5** shows the *Torpedo* α-subunit structure color-coded according to the annotated alignment. The AChR structure has three major domains: the extracellular ligand-binding domain, the transmembrane domain, and the cytoplasmic domain.

The ligand-binding domain is formed from the first ~200 residues of the N-terminus of each subunit. It has a β-sheet core with 10 β-strands arranged in a "Greek-key" motif. There are 6 outer strands and 4 inner strands (**Figures I.4** and **I.5**). The eponymous cys-loop is between strands β6 and β7. It consists of 13 residues flanked by cysteines which form a disulfide bond. The cys-loop contains a well-conserved N-glycosylation signal sequence, N-X-S/T. N-glycosylation is essential for assembly and trafficking of the receptor (*39, 40*), and deglycosylation also attenuates the channel activity of mature receptors (*38*).

The transmembrane and cytoplasmic domains are C-terminal to the ligand-binding domain. The transmembrane domain is made up of 4 α helices labeled M1–M4. The ion conduction pore is lined by the M2 helices from each subunit. The M1, M3, and M4 helices form an outer ring, and they interact with the lipid bilayer. Between the M3 and M4 sequences, there is a cytoplasmic domain. It contains one α helix called the amphipathic helix, MA. The cytoplasmic domain is important for assembly, trafficking, phosphorylation, and interactions with other proteins (*41-44*).

I.F The N-Terminal Ligand Binding Domain

Agonists and competitive antagonists bind the transmitter binding sites (TBSs) in the extracellular ligand binding domain. In the muscle-type AChR, there are two distinct TBSs. The first site is found at the interface of the α and δ subunits. The second site is found at the interface of the α and ε subunits in the adult-type AChR or at the interface of the α and γ subunits in the fetal-type AChR. When both sites are unoccupied, the probability that the channel will open is 10^{-7}–10^{-6}. When both sites are bound with acetylcholine, the probability that the channel will open increases to nearly 1 (*45*).

When the TBSs are unoccupied, the closed-state ligand-binding domain is asymmetric because of the orientation of the α subunits. In the closed state, the α subunits' backbone carbons overlay well with one another, and the non-α subunits overlay well with one another. However, the α subunits do not overlay well with the non-α subunits. The α subunits are "distorted" in the closed AChR. Their β-sheet cores are rotated approximately 10° (**Figure I.6**) (*6, 20, 46*).

When the TBSs are occupied by agonist, the open/desensitized ligand-binding domain is highly symmetrical. Structural rearrangements were visible in cryoelectron images of the open AChR (*20, 46*). In agonist-bound open state, all the subunits overlay well. The α subunits rotate and convert to a "relaxed" conformation that is similar to the conformation of non-α subunits. It is proposed that the rotation of the α subunits is coupled to rotation of the transmembrane helices. Rotation of the transmembrane helices is thought to cause pore widening, allowing ion flux.

A hydrated pocket inside the α subunit's β-sheet core is important for conversion from the closed state to the open state. X-ray crystallography of the mouse α subunit revealed an ordered water molecule inside the ligand-binding domain (*38*). The water interacts with highly conserved residues, αThr52 and αSer126. These residues can be mutated to alanine or valine with minor effects. Mutation to bulkier hydrophobic residues does not impair surface expression, but it impairs gating. It is proposed that the hydrated pocket provides the α subunits with conformational flexibility, and the flexibility is necessary for the allosteric gating mechanism.

I.G The Transmitter Binding Sites

Each TBS is made up of a "principal face" and a "complementary face". An α subunit always contributes the principal face. α subunit binding determinants are found on three major segments, Loops A, B, and C. 75% of the binding-site residues are found on the α subunit. In the muscle-type AChR, the δ, γ, or ε subunits contribute the complementary face. Complementary binding determinants are found on four major segments, Loops D, E, F, and G (**Figure I.7**). In the adult-type AChR, sequence variations in the δ and ε subunits are correlated with the different TBSs' affinities for agonists and competitive antagonists (*47-50*).

Affinity labeling identified a reducible disulfide bond, several aromatic residues, and several acidic residues at the TBSs (*15, 16*). 4-(N-maleimido)benzyltri-[^{3}H]-methylammonium iodide is an electrophilic alkylating reagent. It was used to affinity label residues αC192 and αC193 in Loop C. These cysteines form the vicinal disulfide pair that is characteristic of all α subunits (*51*). The photoaffinity reagent [^{3}H]-p-(dimethylamino)-benzenediazonium fluoroborate was used to identify several residues on the principal face: in Loop A, αTyr93 (*52*); in Loop B, αTrp149 and αTyr151; in Loop C, αTyr190, αCys192, and αCys193 (*53*). Photolabeling with [^{3}H]-nicotine identified several residues on both the principal and complementary face: in Loop C, αTyr190, αCys192, and αTyr198 (*54, 55*); in Loop E, γTrp55 (*54*). Chemical crosslinking identified several acidic residues on the complementary face in Loop F: δAsp165, δAsp180, δGlu182, γAsp174 (*56-58*).

Conserved aromatic residues at the TBSs form an "aromatic cage" where ammonium groups bind. The aromatic cage consists of five conserved residues: αTyr93 in Loop A; αTrp149 in Loop B; αTyr190 and αTyr198 in Loop C; and δTrp57, εTyr55, or γTyr55 in Loop E. Mutagenesis and functional studies implicate all of these residues in AChR function (*15, 16*). Atomic-resolution structures of the mouse α subunit and AChBPs further corroborated the identification of residues in the aromatic cage (*7, 22*).

Acidic residues in and around the TBSs are thought to mediate long range electrostatic interactions with positively charged ligands. AChR agonists and competitive antagonists are most commonly ammonium compounds. For example, acetylcholine is a quaternary ammonium, nicotine is a tertiary ammonium, and epibatidine is a secondary ammonium at physiological pH (**Figure I.8**). The TBSs exhibit a net negative electrostatic potential of approximately -10 mV, measured by accessibility to charged affinity labeling reagents (*59*) and diffusion-enhanced fluorescence energy transfer (*60*). Electrostatic steering at the TBSs contribute approximately -1 kcal/mol binding energy by increasing association rate constants (*60*). However, acidic residues do not make direct contacts with agonists (*22, 27*). Direct charge neutralization and ion pairing are not as important to binding as hydrogen bonding and other interactions.

It is proposed that a critical factor in AChR pharmacology is the ability of agonists and competitive antagonists to form a cation-π interaction at the TBSs (*61*). For example, cation-π interactions between agonists and αTrp149 are important for AChR activation. Unnatural amino

acid mutagenesis was used to introduce fluorinated analogs into the muscle-type AChR at position α149 (*61-63*). Fluorination of αTrp149 in Loop B attenuates activation of the receptor by the potent agonists acetylcholine and epibatidine. It increases the concentration required for half-maximal activation, EC_{50}. The change in EC_{50} correlated well with the calculated cation-π binding potential of the fluorinated analogs (*63, 64*). In contrast to the strong agonists acetylcholine and epibatidine, the weak agonist nicotine does not form a cation-π interaction with αW149 (*62*). Structural studies show that αW149 is positioned at the TBS by a redundant network of hydrogen bonds. Residue αD89 is a part of this network, and substitution with standard or unnatural amino acids at this position can disrupt binding of acetylcholine (*65, 66*). Thus, cation-π interactions with αW149 are critical for AChR activation and are sensitive to the conformation of αW149.

TBS conformational changes associated with AChR activation have been inferred from AChBP structures (*67*), and the most notable change is the movement of Loop C (**Figure I.9**) (*7*). Several structures of AChBPs with no ligand bound, bound to a competitive antagonist, or bound to an agonist have been published (*22-31*). The apo- or antagonist-bound AChBP structure corresponds to the closed conformation of the AChR ligand binding domain. In the closed state, Loop C is positioned away from the binding site in an "uncapped" conformation. When agonist is bound to the TBS, Loop C "caps" the site. There is an approximately 10 Å change in position. In the capped conformation, the binding site and aromatic cage are arranged more compactly around the agonist. It is not clear whether the agonist-bound AChBP represents the agonist-bound open (*68*) or desensitized state (*34*) of the AChR ligand-binding domain, but movement of Loop C is likely a key event in the coupling of agonist binding to pore gating.

I.H The Ion Conduction Pore

Affinity labeling and mutagenesis originally determined that the ion conduction pore is lined by the M2 helices. Residues in the M2 transmembrane segment were affinity labeled, using the non-competitive antagonists chlorpromazine (*59, 69, 70*), triphenylmethylphosphonium (*71*), meproadifen mustard (*72*), 3-(trifluoromethyl)-3-(m-[^{125}I]iodophenyl)diazirine (*73*), and tetracaine (*74*). Labeling patterns implied α-helical secondary structure, with hydrophobic residues predominantly facing the pore lumen. Mutagenesis demonstrated that the M2 segments determine the magnitude of the current flow, called the conductance, through the open channel.

Chimeric receptors were made with M2 segments interchanged between bovine and *Torpedo* AChRs. The conductances of the chimeras were determined by the species which donated the M2 segment (*75*). Subsequently, several acidic and glutamine residues were identified which control conductance and cation selectivity (*76*). These residues are arranged in three rings of equivalent positions in the pore. The "inner" and "intermediate" rings are near the intracellular end of the pore, and the "outer" ring is at the extracellular end. (**Figure I.10**) In the intermediate ring, mutagenesis indicated that αGlu241 and its equivalent positions have the greatest impact on conductance and cation selectivity. Chemical labeling experiments later identified M1 residues that also line the pore (*77-80*). The residues are at the extracellular end of the M1 helices. It was proposed that the pore is wider at the extracellular side, which would require M1 residues to line the pore.

The 4 Å resolution model of the *Torpedo* AChR transmembrane domain suggests a mechanism for pore opening (**Figure I.10**) (*6, 18*). In agreement with biochemical studies, the model includes a funnel-like transmembrane region that narrows at intracellular end. The M1, M3, and M4 helices form an outer ring, interacting with the lipid bilayer. The M2 helices form an inner ring, lining the pore. The M2 helices extend approximately 10 Å above the lipid bilayer, and the axial ion conduction path is approximately 40 Å long. The pore constricts at its middle and remains constricted to its intracellular end. The constriction creates a hydrophobic zone approximately 8 Å long. This zone may prevent ion flow in the closed state, acting as the "resting gate". The zone is narrowest at residues αLeu251 and αVal255 where the channel diameter is approximately 6–7 Å. Sodium and potassium cations would be required to lose their solvation shell to pass through this barrier. However, desolvation is energetically unfavorable in the absence of acidic and polar residues. Gating would therefore entail widening of the channel in this region. When agonist binds, the α-subunits' ligand binding domains may rotate. The rotation may be coupled to the transmembrane domain by the loop between the β1 and β2 strands. Movement of the loop could then rotate the M2 helices. Rotation of the M2 helices could reposition hydrophobic residues away from the pore axis, widening the conduction pathway and opening the resting gate (*18*).

The substituted-cysteine accessibility method (SCAM) has been used to identify the resting gate and an analogous desensitization gate. In SCAM, a pore residue of interest is mutated to a cysteine. If the residue is surface/water exposed, then it can be modified by a

methanethiosulphonate reagent. Modified residues may interrupt the flow of ions through the pore, and therefore reactivity can be monitored using electrophysiology. SCAM can assay changes in the environment of a residue in the absence and presence of acetylcholine and has been used to identify the resting and desensitization gates (*81, 82*). The resting gate is located at the intracellular end of the pore from residues αGly240 to αThr244 and the equivalent positions in the non-α subunits (*82*). SCAM experiments and other functional studies suggest that there is a desensitization gate that is distinct from the resting gate (*83, 84*). The desensitization gate is located at residue αLeu251, more extracellular to the resting gate (*85*).

More recently, functional studies have suggested pore gating involves subtle changes in pore residues rather than large rotations of the M2 helices. Similar to SCAM, a pore residue of interest can be mutated to an ionizable residue, Lys, Arg, or His. Protonation of the substituted residue may interrupt ion flow, allowing protonation to be monitored by electrophysiology. The pKa at each position can then be estimated specifically for the open channel. Residues throughout the M1, M2, and M3 helices have been probed (*86, 87*). The residues identified as facing the lumen of the open pore are the same as those identified as facing the lumen of the closed pore by affinity labeling. Thus, gating involves only subtle changes in pore residue conformations, and opening involves only slight widening of the pore. Theoretical studies suggest that even a 1.5 Å increase in radius is sufficient for opening. This small increase in radius is calculated to significantly decrease the energetic barrier to ion conduction across the hydrophobic gate region (*88, 89*). Together, protonation and SCAM experiments suggest that the resting gate is located at the narrow, hydrophobic intracellular end of the pore, and small conformational movements in gate residues are sufficient to widen the pore enough for solvent accessibility and ion conduction.

I.I Coupling of Agonist Binding to Channel Gating

The central mechanistic question about AChR function is how agonist binding is allosterically linked to channel gating. The TBSs are approximately 40 Å away from the pore resting gate. When agonists bind to the TBSs, three large scale conformational changes are apparent. First, Loop C moves approximately 10 Å and caps the agonist-bound site. Second, the α subunits rotate approximately 10°. Third, the pore widens at the hydrophobic gate region, permitting ion flux. While this model of the coupling between TBS and pore is consistent with

recent structural data, the exact details of the structural basis for the allosteric linkage are still being investigated. The AChBP structures have been particularly useful on this front. At atomic resolution, AChBP models and homology models have permitted specific interactions to be proposed and investigated. As a result, several loops and interacting residues have been shown to be a part of the AChR allosteric pathway.

Three loops at the interface of the ligand-binding domain and transmembrane domain are important to the coupling mechanism, and optimization of these loops can rescue the activity of initially non-functional chimeric receptors (*90*). The ligand-binding domain of the serotonin 5-HT_{3A} receptor, a homomeric AChR-type channel, was replaced with the AChBP. The AChBP can bind agonist, but it lacks the structural elements required for allosteric coupling. Thus, the chimera exhibited normal surface expression and ligand-binding properties, but binding of agonist did not cause channel opening. The β1-β2 loop, cys-loop, and β8-β9 loop were then mutated from the AChBP residues to the corresponding residues of the 5-HT_{3A} receptor. Replacement of these loops rescued the allosteric coupling, and the chimeric channels opened in response to agonist binding. It is hypothesized that these three loops propagate conformational changes by interacting directly with the transmembrane helices or with the M2-M3 loop.

Subsequently, three other "triggers" were identified which couple agonist binding to gating (**Figure I.11**) (*91-93*). The first trigger is proximal to the TBS. It consists of three residues, αTyr190, αAsp200, and αLys145 (*93*). In the resting agonist-free state, αAsp200 and αLys145 form a salt bridge (*7*). When agonist binds, movement of Loop C brings the hydroxyl group of αTyr190 within 2-3 Å of αAsp200. Because of the interaction between αTyr190 and αAsp200, the αAsp200–αLys145 salt bridge is weakened. This causes a conformational change in αLys145. αLys145 is part of the β7 strand, adjacent to the cys-loop which has already been implicated in the coupling mechanism.

The second trigger is also proximal to the TBS, and it consists of an intersubunit pair of spatially adjacent residues. The pair consists of αTyr127 on the principal face and δAsn41 (or εAsn39) on the complementary face (*92*). αTyr127 is adjacent to the cys-loop, δAsn41 is adjacent to the β1-β2 loop, and both loops are already implicated in the allosteric mechanism. αTyr127 and δAsn41 are energetically coupled, and disruption of their interaction attenuates fast gating.

The third trigger has been called a principal pathway for coupling of agonist binding and channel gating because it makes a much larger contribution to the allosteric linkage than the other identified pathways (*91*). This trigger consists of five residues at the domain interface of the α-subunits. αArg209 is between the β10 strand and the M1 helix. It interacts with αGlu45 in the β1-β2 loop. αGlu45 is adjacent to αVal46. αVal46 interacts with αPro272 and αSer269 in the M2-M3 linker. When agonist binds, movement of Loop C may be transmitted through the β10 strand and the M2-M3 linker through these five residues. These residues are energetically coupled, and disruption of their interactions attenuates gating more severely than disruption of the other triggers. These triggers demonstrate that a principal pathway for coupling of agonist binding to pore opening exists, but there are also several redundant interactions. Both principal and redundant allosteric linkages are functionally important and conserved for AChRs. However, they are not conserved across the cys-loop superfamily. Instead, the coupling elements are tuned to the specific purpose of each receptor (*61*).

I.J The Gating Transition State and Conformational Dynamics

Rate-equilibrium free energy relationships have been used to probe the dynamics and transition state of AChR gating (*94*). Structural data have provided static models of the closed, open, and desensitized states (*16, 61, 67, 95*); however, it remains a challenge to obtain dynamic information about gating conformational changes. Probing the details of the short-lived open state has been particularly difficult. Recently, a linear free energy relationship approach derived from physical organic chemistry has been used to address channel dynamics. Residues throughout the AChR are probed through mutagenesis. The effects of mutations on gating are assessed by single-channel electrophysiology. By assessing several mutations of a particular position, a linear free-energy relationships is observed. The Φ-value is the slope of linear relationship between the logarithm of opening rate and the logarithm of gating equilibrium. Measuring Φ-values for positions throughout the receptor creates a map of the conformational wave linking agonist-binding and pore opening (**Figure I.12**) (*96-107*).

The Φ-value is a measure of transition state structure and timing of conformational changes during gating. The Φ-value is between 0 and 1. For $\Phi = 1$, changes in the gating equilibrium are due entirely to changes in the opening rate. A Φ-value approaching 1 indicates that a residue's conformation in the gating transition state is similar to its open-state

conformation. It also implies that, during gating, changes in this residue's conformation occur early in the reaction. Conversely, for $\Phi = 0$, changes in gating equilibrium are due entirely to changes in the closing rate. A Φ-value approaching 0 indicates that a residue's conformation in the gating transition state is similar to its closed-state conformation. It also implies that, during gating, changes in this residue's conformation occur late in the reaction. For the AChR, binding site residues exhibit Φ-values close to 1, consistent with an allosteric reaction initiated by agonist binding. Residues at the interface of the ligand-binding domain and the transmembrane domain exhibit intermediate Φ-values. Residues in the pore region exhibit low Φ-values (*107*). AChR gating involves sequential conformational changes of distinct Φ-value regions, transducing agonist binding into pore opening.

I.K The Desensitized State

The desensitized state is a non-conducting conformation that is thermodynamically favored in the presence of agonist. For the muscle-type AChR, it is known that there is a desensitization gate distinct from the resting gate (*81, 83, 84*); however, it has also been observed that there are several kinetically resolvable desensitized states (*108*). Desensitization kinetics vary widely across LGICs, and desensitization is known to be important in shaping the synaptic currents of neuronal AChRs and other LGICs (*109, 110*). In the case of the normal neuromuscular junction, it is unlikely that desensitization influences endplate currents because the muscle-type AChR desensitizes slowly compared to the half-life of acetylcholine in the synaptic cleft. However, desensitization likely plays a role in shaping endplate currents of diseased neuromuscular junctions, such as in slow-channel myasthenic syndromes (*111*). One of the major unresolved questions is what differences there are between the open-state and desensitized-state ligand-binding domains. Both states are high agonist-affinity conformations. It has been proposed that the desensitized conformation involves formation of short-range electrostatic interactions between the binding site and the agonist (*112*).

I.L Single-Channel Patch-Clamp Electrophysiology

Patch-clamp electrophysiology is one of the most widely used techniques for the functional characterization of AChRs and ion channels in general (*8, 113*). It allows measurement of current flow through open channels expressed at a cell surface. To obtain a

patch-clamp recording, a glass pipette is first used to isolate a membrane patch containing one or several ion channels. By applying gentle suction when the pipette contacts the membrane, a tight seal is formed between the glass and the membrane. The pipette contains an electrolyte solution and an electrode. The cells are bathed in an appropriate electrolyte solution containing a ground electrode. This configuration creates a circuit, allowing open channel currents to be detected. Because single-channel currents have picoampere magnitudes, these currents require specialized amplifiers to achieve adequate signal-to-noise ratios.

The three main modes of patch-clamp electrophysiology are the cell-attached, inside-out, and outside-out modes (**Figure I.13**) (*114*). In the cell-attached mode, the pipette is sealed to the membrane, and the cell is left intact during recording. In the inside-out mode, the pipette and isolated membrane patch are pulled away from the cell. This action leaves the intracellular membrane face exposed to the bathing solution. The extracellular surface faces the inside of the pipette. In the outside-out mode, the isolated membrane patch is ruptured, and then the pipette is pulled away from the cell. The ruptured membrane reforms, exposing the extracellular membrane face to the bathing solution. The intracellular surface faces the inside of the pipette. In all three modes, single-channel recordings can be obtained.

The patch-clamp amplifier can be used both to record currents and to control transmembrane voltage. Under normal physiological conditions, the interior of an excitable cell is at a potential of -40 to -70 mV relative to the extracellular solution. In cell-attached patches, a "command" voltage between the pipette and bath electrodes is applied by the amplifier. The command voltage is additive with the natural transmembrane voltage. Using the command voltage, the total circuit voltage is held constant, or "voltage-clamped". Current flow through open channels in the patch is usually detected under voltage clamp. The opening conformational change occurs on microsecond timescales, much faster than the patch-clamp recording bandwidth. Therefore, single-channel currents appear as all-or-nothing binary events. The currents are detected and amplified by the patch-clamp amplifier. The analog current data is digitized and recorded directly to a computer for single-channel analysis.

I.M Single-Channel Kinetic Analysis

Channel conductance and reversal potential are two channel properties that can be investigated by single-channel electrophysiology. Channel conductance, g, defines the

magnitude of the open-channel current at a particular transmembrane voltage. The reversal potential, V_R, is the transmembrane potential at which current flow reverses. It indicates the ion selectivity of a channel. For a channel selective to Na^+, the reversal potential equals the Nernst potential for Na^+. For a non-selective channel, the reversal potential is approximately 0. These two properties are measured by recording single-channel currents over a range of applied voltages. According to Ohm's law, the observed current-voltage relationship is $I = g \cdot (V - V_R)$, where V is the applied voltage.

Single-channel electrophysiology also provides information about the kinetics associated with channel conformational changes. Single-channel electrophysiology is a single-molecule technique, and the observed channel openings are stochastic in nature. When analyzing single-channel data, microscopic rate constants can be treated as probabilities. They are the transition probabilities for changes from one conformational state to another. For example, consider an ion channel that has only three conformations. It has closed and desensitized conformations which are non-conducting and an open conformation which is ion-conducting. Suppose that the conformational transitions are described by the kinetic model in **Scheme I.1** where rate constants have units s^{-1}. The closed channel can either open or remain closed. The open channel can either close or desensitize. The desensitized channel can re-open or remain desensitized.

Microscopic rate constants are measured by analyzing the distributions of the durations of conducting and non-conducting events (**Figure I.14**). In a single-channel record, a series of conducting and non-conducting periods are observed. The dwell times, the lengths of these periods, are measured. The open state can be unambiguously assigned to conducting periods. The mean open dwell time is inversely proportional to the total probability of leaving the open state. The total probability of leaving the open state equals the probability for the open-to-closed transition plus the probability for the open-to-desensitized transition. Therefore, the mean open dwell time for the system described by **Scheme I.1** is $\langle t_{open} \rangle = (k_{-1} + k_{+2})^{-1}$. Because single-molecule conformational changes are stochastic processes, the open dwell times will be exponentially, not normally, distributed. In contrast to open events, non-conducting periods cannot be unambiguously assigned to either the closed or the desensitized state. However, the distribution of non-conducting dwell times will be the sum of two exponential functions. The two exponentials have respective decay times $\langle t_{closed} \rangle = k_{+1}^{-1}$ and $\langle t_{desensitized} \rangle = k_{-2}^{-1}$. If k_{+1} and k_{-2} are sufficiently different, the two non-conducting states will be distinct (**Figure I.14**).

When k_{+1} and k_{-2} are very different, the events have a characteristic "clustered" appearance (**Figure I.15**). When clustered events are observed, the non-conducting periods can be attributed to the closed and desensitized states with relatively high probability. For example, assume activity from exactly one channel is recorded, and let $k_{+1} = 2000\ s^{-1}$, $k_{-1} = 1000\ s^{-1}$, $k_{+2} = 1\ s^{-1}$, and $k_{-2} = 0.1\ s^{-1}$ in **Scheme I.1**. Clusters of short conducting and non-conducting periods will be observed. These periods can be assigned to the open and closed states, respectively. The "intracluster" closed dwell times will be exponentially distributed with a mean lifetime of $1/k_{+1} = (2000\ s^{-1})^{-1} = 0.5$ ms. The intracluster open dwell times will be exponentially distributed with a mean lifetime of $1/k_{-1} = (1000\ s^{-1})^{-1} = 1$ ms. Clusters will be separated by long non-conducting periods that can be assigned to the desensitized state. Desensitized dwell times will be exponentially distributed with a mean lifetime of $1/k_{-2} = (0.1\ s^{-1})^{-1} = 10$ s. There are no direct transitions between the closed and desensitized states. Therefore, the total intracluster open time will be exponentially distributed with a mean lifetime of $1/k_{+2} = (1\ s^{-1})^{-1} = 1$ s. If a physically relevant kinetic model is available, single-channel kinetic analysis can provide estimates for microscopic rate constants that would be otherwise difficult to determine with ensemble methods.

There are physically relevant kinetic models that can accurately describe and predict the activity of muscle-type AChRs . The AChR is generally described using a concerted Monod-Wyman-Changeux allosteric model (*115*). The AChR has three distinct functional states in this model, the closed, open, and desensitized states. The channel can bind zero, one, or two agonist molecules leading to states termed unliganded, monoliganded, or diliganded, respectively. Ligand binding favors opening and desensitization.

AChR kinetic models (**Scheme I.2** and **I.3**) are more complex than the example given in **Scheme I.1**, but single-channel kinetic analysis of these models is quite tractable because of well-developed statistical methods. Single-channel records are first idealized. Unprocessed records consist of a time-ordered list of current amplitudes. To idealize these records, each data point is classified as conducting or non-conducting. A time-ordered list of conducting and non-conducting dwell times is produced. When a kinetic model is proposed, it predicts what the distribution of dwell times will be. The rate constants in a proposed kinetic model can be varied until the predicted distributions best fit the observed data. A maximum-interval likelihood algorithm is used for this fitting procedure. Fitting produces two results: estimated microscopic

rate constants and a likelihood score for the estimation. The likelihood score is the probability that the observed data is a result of the proposed model and is useful for discriminating between models.

Single-channel kinetic analysis is sensitive to the omission of short-lived events due to finite recording bandwidth, but methods to correct for these missed events are available. When an event is very short in duration, it may be missed or truncated because it is too short to be detected by the patch-clamp amplifier. This missed-event problem can be described analytically and incorporated into fitting algorithms. Software is available which uses a mathematically exact solution to compensate for missed events, but this method requires significant computational time (*116*). Software is also available which uses an approximate solution to correct for missed events (*117*). The approximate method estimates microscopic rate constants with comparable accuracy to the exact method and requires less computing time. In the approximate solution, the total duration of missed events is assumed to be small compared to observed events. A "dead time" is defined, and events shorter than the dead time are considered undetected. Adjacent events are concatenated. The dead time is then used to make a first-order correction to the dwell-time distributions predicted by the proposed model. The maximum interval likelihood and approximate missed event correction algorithms are incorporated in the QuB software suite (*117-119*). This software package was used to analyze data presented throughout this thesis.

I.N Conclusions

Recent high-resolution AChR and AChBP structures have enhanced our understanding of the allosteric coupling between agonist binding and pore opening. However, it still remains a challenge to provide atomic-level details for all of the functionally relevant AChR conformations and to probe the structural dynamics involved in AChR allosteric transitions. Models for the agonist-bound closed AChR and agonist-bound open AChR are still unavailable. A better understanding of the nature of agonist and antagonist binding interactions is still needed to define AChR pharmacology. In this thesis, the conformation, interactions, and dynamics at the TBSs were investigated in structure-function studies, utilizing single-channel kinetic analysis. In Chapter II, an agonist structure-activity relationship is explored. Calculated cation-pi binding energies are shown to correlate with gating efficiency. This parameter may be useful for

predicting and designing agonists and antagonists. In Chapter III, the contributions of the TBS principal and complementary faces to agonist binding in the closed and open state are compared. Results suggest that the open state, like the desensitized-state model, is highly symmetric. At the TBSs, structural and functional symmetry are increased by decreasing the contribution of the complementary face to binding.

Chapter IV describes efforts to exploit the channel conformation-dependence of small-molecule binding to the AChR to develop chemical probes for use in living cells. A non-competitive antagonist incorporating pore binding, photolabeling, and click chemistry moieties was synthesized. The candidate probe's ability to inhibit the AChR was characterized electrophysiologically, and state-dependent photolabeling by the probe was demonstrated in living cells. The probe could be a useful chemical tool in investigations of activity-dependent changes in AChR biology associated with neuromuscular diseases or nicotine addiction.

I.O References

1. Changeux, J. P., and Taly, A. (2008) Nicotinic receptors, allosteric proteins and medicine. *Trends Mol. Med. 14*, 93-102.
2. Changeux, J. P., and Edelstein, S. J. (1998) Allosteric receptors after 30 years. *Neuron 21*, 959-980.
3. Colquhoun, D., and Sakmann, B. (1998) From muscle endplate to brain synapses: a short history of synapses and agonist-activated ion channels. *Neuron 20*, 381-387.
4. Kalamida, D., Poulas, K., Avramopoulou, V., Fostieri, E., Lagoumintzis, G., Lazaridis, K., Sideri, A., Zouridakis, M., and Tzartos, S. J. (2007) Muscle and neuronal nicotinic acetylcholine receptors. Structure, function and pathogenicity. *FEBS J. 274*, 3799-3845.
5. Colquhoun, D. (1998) Binding, gating, affinity and efficacy: the interpretation of structure-activity relationships for agonists and of the effects of mutating receptors. *Brit. J. Pharmacol. 125*, 924-947.
6. Unwin, N. (2005) Refined structure of the nicotinic acetylcholine receptor at 4A resolution. *J. Mol. Biol. 346*, 967-989.
7. Brejc, K., van Dijk, W. J., Klaassen, R. V., Schuurmans, M., van Der Oost, J., Smit, A. B., and Sixma, T. K. (2001) Crystal structure of an ACh-binding protein reveals the ligand-binding domain of nicotinic receptors. *Nature 411*, 269-276.
8. Hille, B. (2001) *Ion channels of excitable membranes*, 3rd ed., Sinauer, Sunderland, Mass.
9. Yu, F. H., Yarov-Yarovoy, V., Gutman, G. A., and Catterall, W. A. (2005) Overview of molecular relationships in the voltage-gated ion channel superfamily. *Pharmacol. Rev. 57*, 387-395.
10. Khakh, B. S., and North, R. A. (2006) P2X receptors as cell-surface ATP sensors in health and disease. *Nature 442*, 527-532.
11. Dani, J. A., and Bertrand, D. (2007) Nicotinic acetylcholine receptors and nicotinic cholinergic mechanisms of the central nervous system. *Ann. Rev. Pharmacol. Toxicol. 47*, 699-729.
12. Gotti, C., Zoli, M., and Clementi, F. (2006) Brain nicotinic acetylcholine receptors: native subtypes and their relevance. *Trends Pharmacol. Sci. 27*, 482-491.
13. Langley, J. N. (1907) On the contraction of muscle, chiefly in relation to the presence of "receptive" substances. *J. Physiol. 36*, 347-384.
14. Katz, B., and Thesleff, S. (1957) A study of the desensitization produced by acetylcholine at the motor end-plate. *J. Physiol. 138*, 63-80.
15. Corringer, P. J., Le Novere, N., and Changeux, J. P. (2000) Nicotinic receptors at the amino acid level. *Ann. Rev. Pharmacol. Toxicol. 40*, 431-458.
16. Karlin, A. (2002) Emerging structure of the nicotinic acetylcholine receptors. *Nat. Rev. Neurosci. 3*, 102-114.
17. Unwin, N. (1993) Nicotinic acetylcholine receptor at 9 A resolution. *J. Mol. Biol. 229*, 1101-1124.
18. Miyazawa, A., Fujiyoshi, Y., and Unwin, N. (2003) Structure and gating mechanism of the acetylcholine receptor pore. *Nature 423*, 949-955.
19. Sine, S. M. (2002) The nicotinic receptor ligand binding domain. *J. Neurobiol. 53*, 431-446.

20. Unwin, N. (1995) Acetylcholine receptor channel imaged in the open state. *Nature 373*, 37-43.
21. Smit, A. B., Syed, N. I., Schaap, D., van Minnen, J., Klumperman, J., Kits, K. S., Lodder, H., van der Schors, R. C., van Elk, R., Sorgedrager, B., Brejc, K., Sixma, T. K., and Geraerts, W. P. (2001) A glia-derived acetylcholine-binding protein that modulates synaptic transmission. *Nature 411*, 261-268.
22. Celie, P. H., van Rossum-Fikkert, S. E., van Dijk, W. J., Brejc, K., Smit, A. B., and Sixma, T. K. (2004) Nicotine and carbamylcholine binding to nicotinic acetylcholine receptors as studied in AChBP crystal structures. *Neuron 41*, 907-914.
23. Celie, P. H., Kasheverov, I. E., Mordvintsev, D. Y., Hogg, R. C., van Nierop, P., van Elk, R., van Rossum-Fikkert, S. E., Zhmak, M. N., Bertrand, D., Tsetlin, V., Sixma, T. K., and Smit, A. B. (2005) Crystal structure of nicotinic acetylcholine receptor homolog AChBP in complex with an alpha-conotoxin PnIA variant. *Nat. Struct. Mol. Biol. 12*, 582-588.
24. Celie, P. H., Klaassen, R. V., van Rossum-Fikkert, S. E., van Elk, R., van Nierop, P., Smit, A. B., and Sixma, T. K. (2005) Crystal structure of acetylcholine-binding protein from Bulinus truncatus reveals the conserved structural scaffold and sites of variation in nicotinic acetylcholine receptors. *J. Biol. Chem. 280*, 26457-26466.
25. Ulens, C., Hogg, R. C., Celie, P. H., Bertrand, D., Tsetlin, V., Smit, A. B., and Sixma, T. K. (2006) Structural determinants of selective alpha-conotoxin binding to a nicotinic acetylcholine receptor homolog AChBP. *Proc. Natl. Acad. Sci. U.S.A. 103*, 3615-3620.
26. Dutertre, S., Ulens, C., Buttner, R., Fish, A., van Elk, R., Kendel, Y., Hopping, G., Alewood, P. F., Schroeder, C., Nicke, A., Smit, A. B., Sixma, T. K., and Lewis, R. J. (2007) AChBP-targeted alpha-conotoxin correlates distinct binding orientations with nAChR subtype selectivity. *EMBO J. 26*, 3858-3867.
27. Hansen, S. B., Sulzenbacher, G., Huxford, T., Marchot, P., Taylor, P., and Bourne, Y. (2005) Structures of Aplysia AChBP complexes with nicotinic agonists and antagonists reveal distinctive binding interfaces and conformations. *EMBO J. 24*, 3635-3646.
28. Bourne, Y., Talley, T. T., Hansen, S. B., Taylor, P., and Marchot, P. (2005) Crystal structure of a Cbtx-AChBP complex reveals essential interactions between snake alpha-neurotoxins and nicotinic receptors, *EMBO J. 24*, 1512-1522.
29. Hansen, S. B., and Taylor, P. (2007) Galanthamine and non-competitive inhibitor binding to ACh-binding protein: evidence for a binding site on non-alpha-subunit interfaces of heteromeric neuronal nicotinic receptors. *J. Mol. Biol. 369*, 895-901.
30. Talley, T. T., Harel, M., Hibbs, R. E., Radic, Z., Tomizawa, M., Casida, J. E., and Taylor, P. (2008) Atomic interactions of neonicotinoid agonists with AChBP: molecular recognition of the distinctive electronegative pharmacophore. *Proc. Natl. Acad. Sci. U.S.A. 105*, 7606-7611.
31. Ihara, M., Okajima, T., Yamashita, A., Oda, T., Hirata, K., Nishiwaki, H., Morimoto, T., Akamatsu, M., Ashikawa, Y., Kuroda, S., Mega, R., Kuramitsu, S., Sattelle, D. B., and Matsuda, K. (2008) Crystal structures of Lymnaea stagnalis AChBP in complex with neonicotinoid insecticides imidacloprid and clothianidin. *Invert. Neurosci. 8*, 71-81.
32. Schapira, M., Abagyan, R., and Totrov, M. (2002) Structural model of nicotinic acetylcholine receptor isotypes bound to acetylcholine and nicotine. *B.M.C. Struc. Biol. 2*, 1.
33. Fruchart-Gaillard, C., Gilquin, B., Antil-Delbeke, S., Le Novere, N., Tamiya, T., Corringer, P. J., Changeux, J. P., Menez, A., and Servent, D. (2002) Experimentally

based model of a complex between a snake toxin and the alpha 7 nicotinic receptor. *Proc. Natl. Acad. Sci. U.S.A. 99*, 3216-3221.

34. Le Novere, N., Grutter, T., and Changeux, J. P. (2002) Models of the extracellular domain of the nicotinic receptors and of agonist- and Ca2+-binding sites. *Proc. Natl. Acad. Sci. U.S.A. 99*, 3210-3215.
35. Sine, S. M., Wang, H. L., and Bren, N. (2002) Lysine scanning mutagenesis delineates structural model of the nicotinic receptor ligand binding domain. *J. Biol. Chem. 277*, 29210-29223.
36. Law, R. J., Henchman, R. H., and McCammon, J. A. (2005) A gating mechanism proposed from a simulation of a human alpha7 nicotinic acetylcholine receptor. *Proc. Natl. Acad. Sci. U.S.A. 102*, 6813-6818.
37. Cheng, X., Wang, H., Grant, B., Sine, S. M., and McCammon, J. A. (2006) Targeted molecular dynamics study of C-loop closure and channel gating in nicotinic receptors. *PLoS Comp. Biol. 2*, e134.
38. Dellisanti, C. D., Yao, Y., Stroud, J. C., Wang, Z. Z., and Chen, L. (2007) Crystal structure of the extracellular domain of nAChR alpha1 bound to alpha-bungarotoxin at 1.94 A resolution. *Nat. Neurosci. 10*, 953-962.
39. Prives, J., and Bar-Sagi, D. (1983) Effect of tunicamycin, an inhibitor of protein glycosylation, on the biological properties of acetylcholine receptor in cultured muscle cells. *J. Biol. Chem. 258*, 1775-1780.
40. Merlie, J. P., Sebbane, R., Tzartos, S., and Lindstrom, J. (1982) Inhibition of glycosylation with tunicamycin blocks assembly of newly synthesized acetylcholine receptor subunits in muscle cells. *J. Biol. Chem. 257*, 2694-2701.
41. Yu, X. M., and Hall, Z. W. (1994) The role of the cytoplasmic domains of individual subunits of the acetylcholine receptor in 43 kDa protein-induced clustering in COS cells. *J. Neurosci. 14*, 785-795.
42. Yu, X. M., and Hall, Z. W. (1994) A sequence in the main cytoplasmic loop of the alpha subunit is required for assembly of mouse muscle nicotinic acetylcholine receptor. *Neuron 13*, 247-255.
43. Akk, G., and Steinbach, J. H. (2000) Structural elements near the C-terminus are responsible for changes in nicotinic receptor gating kinetics following patch excision. *J. Physiol. 527*, 405-417.
44. Bouzat, C., Bren, N., and Sine, S. M. (1994) Structural basis of the different gating kinetics of fetal and adult acetylcholine receptors. *Neuron 13*, 1395-1402.
45. Jackson, M. B. (1986) Kinetics of unliganded acetylcholine receptor channel gating. *Biophy. J. 49*, 663-672.
46. Unwin, N., Miyazawa, A., Li, J., and Fujiyoshi, Y. (2002) Activation of the nicotinic acetylcholine receptor involves a switch in conformation of the alpha subunits. *J. Mol. Biol. 319*, 1165-1176.
47. Blount, P., and Merlie, J. P. (1989) Molecular basis of the two nonequivalent ligand binding sites of the muscle nicotinic acetylcholine receptor. *Neuron 3*, 349-357.
48. Sine, S. M., Kreienkamp, H. J., Bren, N., Maeda, R., and Taylor, P. (1995) Molecular dissection of subunit interfaces in the acetylcholine receptor: identification of determinants of alpha-conotoxin M1 selectivity. *Neuron 15*, 205-211.

49. Kurosaki, T., Fukuda, K., Konno, T., Mori, Y., Tanaka, K., Mishina, M., and Numa, S. (1987) Functional properties of nicotinic acetylcholine receptor subunits expressed in various combinations. *FEBS Lett. 214*, 253-258.
50. Sine, S. M., and Claudio, T. (1991) Gamma- and delta-subunits regulate the affinity and the cooperativity of ligand binding to the acetylcholine receptor. *J. Biol. Chem. 266*, 19369-19377.
51. Kao, P. N., Dwork, A. J., Kaldany, R. R., Silver, M. L., Wideman, J., Stein, S., and Karlin, A. (1984) Identification of the alpha subunit half-cystine specifically labeled by an affinity reagent for the acetylcholine receptor binding site. *J. Biol. Chem. 259*, 11662-11665.
52. Galzi, J. L., Revah, F., Black, D., Goeldner, M., Hirth, C., and Changeux, J. P. (1990) Identification of a novel amino acid alpha-tyrosine 93 within the cholinergic ligands-binding sites of the acetylcholine receptor by photoaffinity labeling. Additional evidence for a three-loop model of the cholinergic ligands-binding sites. *J. Biol. Chem. 265*, 10430-10437.
53. Dennis, M., Giraudat, J., Kotzyba-Hibert, F., Goeldner, M., Hirth, C., Chang, J. Y., Lazure, C., Chretien, M., and Changeux, J. P. (1988) Amino acids of the Torpedo marmorata acetylcholine receptor alpha subunit labeled by a photoaffinity ligand for the acetylcholine binding site. *Biochemistry 27*, 2346-2357.
54. Chiara, D. C., Middleton, R. E., and Cohen, J. B. (1998) Identification of tryptophan 55 as the primary site of [3H]nicotine photoincorporation in the gamma-subunit of the Torpedo nicotinic acetylcholine receptor. *FEBS Lett. 423*, 223-226.
55. Middleton, R. E., and Cohen, J. B. (1991) Mapping of the acetylcholine binding site of the nicotinic acetylcholine receptor: [3H]nicotine as an agonist photoaffinity label. *Biochemistry 30*, 6987-6997.
56. Martin, M., Czajkowski, C., and Karlin, A. (1996) The contributions of aspartyl residues in the acetylcholine receptor gamma and delta subunits to the binding of agonists and competitive antagonists. *J. Biol. Chem. 271*, 13497-13503.
57. Czajkowski, C., and Karlin, A. (1995) Structure of the nicotinic receptor acetylcholine-binding site. Identification of acidic residues in the delta subunit within 0.9 nm of the 5 alpha subunit-binding. *J. Biol. Chem. 270*, 3160-3164.
58. Martin, M. D., and Karlin, A. (1997) Functional effects on the acetylcholine receptor of multiple mutations of gamma Asp174 and delta Asp180. *Biochemistry 36*, 10742-10750.
59. Stauffer, D. A., and Karlin, A. (1994) Electrostatic potential of the acetylcholine binding sites in the nicotinic receptor probed by reactions of binding-site cysteines with charged methanethiosulfonates. *Biochemistry 33*, 6840-6849.
60. Meltzer, R. H., Thompson, E., Soman, K. V., Song, X. Z., Ebalunode, J. O., Wensel, T. G., Briggs, J. M., and Pedersen, S. E. (2006) Electrostatic steering at acetylcholine binding sites. *Biophys. J. 91*, 1302-1314.
61. Dougherty, D. A. (2008) Cys-loop neuroreceptors: structure to the rescue? *Chem. Rev. 108*, 1642-1653.
62. Cashin, A. L., Petersson, E. J., Lester, H. A., and Dougherty, D. A. (2005) Using physical chemistry to differentiate nicotinic from cholinergic agonists at the nicotinic acetylcholine receptor. *J. Am. Chem. Soc. 127*, 350-356.

63. Zhong, W., Gallivan, J. P., Zhang, Y., Li, L., Lester, H. A., and Dougherty, D. A. (1998) From ab initio quantum mechanics to molecular neurobiology: a cation-pi binding site in the nicotinic receptor. *Proc. Natl. Acad. Sci. U. S. A. 95*, 12088-12093.
64. Beene, D. L., Brandt, G. S., Zhong, W., Zacharias, N. M., Lester, H. A., and Dougherty, D. A. (2002) Cation-pi interactions in ligand recognition by serotonergic (5-HT3A) and nicotinic acetylcholine receptors: the anomalous binding properties of nicotine. *Biochemistry 41*, 10262-10269.
65. Cashin, A. L., Torrice, M. M., McMenimen, K. A., Lester, H. A., and Dougherty, D. A. (2007) Chemical-scale studies on the role of a conserved aspartate in preorganizing the agonist binding site of the nicotinic acetylcholine receptor, *Biochemistry 46*, 630-639.
66. Lee, W. Y., and Sine, S. M. (2004) Invariant aspartic Acid in muscle nicotinic receptor contributes selectively to the kinetics of agonist binding. *J. Gen. Physiol. 124*, 555-567.
67. Gay, E. A., and Yakel, J. L. (2007) Gating of nicotinic ACh receptors; new insights into structural transitions triggered by agonist binding that induce channel opening. *J. Physiol. 584*, 727-733.
68. Stewart, D. S., Chiara, D. C., and Cohen, J. B. (2006) Mapping the structural requirements for nicotinic acetylcholine receptor activation by using tethered alkyltrimethylammonium agonists and antagonists. *Biochemistry 45*, 10641-10653.
69. Giraudat, J., Gali, J., Revah, F., Changeux, J., Haumont, P., and Lederer, F. (1989) The noncompetitive blocker [(3)H]chlorpromazine labels segment M2 but not segment M1 of the nicotinic acetylcholine receptor alpha-subunit. *FEBS Lett. 253*, 190-198.
70. Revah, F., Galzi, J. L., Giraudat, J., Haumont, P. Y., Lederer, F., and Changeux, J. P. (1990) The noncompetitive blocker [3H]chlorpromazine labels three amino acids of the acetylcholine receptor gamma subunit: implications for the alpha-helical organization of regions MII and for the structure of the ion channel. *Proc. Natl. Acad. Sci. U.S.A. 87*, 4675-4679.
71. Hucho, F., Oberthur, W., and Lottspeich, F. (1986) The ion channel of the nicotinic acetylcholine receptor is formed by the homologous helices M II of the receptor subunits. *FEBS Lett. 205*, 137-142.
72. Pedersen, S. E., Sharp, S. D., Liu, W. S., and Cohen, J. B. (1992) Structure of the noncompetitive antagonist-binding site of the Torpedo nicotinic acetylcholine receptor. [3H]meproadifen mustard reacts selectively with alpha-subunit Glu-262. *J. Biol. Chem. 267*, 10489-10499.
73. White, B. H., and Cohen, J. B. (1992) Agonist-induced changes in the structure of the acetylcholine receptor M2 regions revealed by photoincorporation of an uncharged nicotinic noncompetitive antagonist. *J. Biol. Chem. 267*, 15770-15783.
74. Middleton, R. E., Strnad, N. P., and Cohen, J. B. (1999) Photoaffinity labeling the torpedo nicotinic acetylcholine receptor with [(3)H]tetracaine, a nondesensitizing noncompetitive antagonist. *Mol. Pharmacol. 56*, 290-299.
75. Imoto, K., Methfessel, C., Sakmann, B., Mishina, M., Mori, Y., Konno, T., Fukuda, K., Kurasaki, M., Bujo, H., Fujita, Y., and et al. (1986) Location of a delta-subunit region determining ion transport through the acetylcholine receptor channel. *Nature 324*, 670-674.
76. Imoto, K., Busch, C., Sakmann, B., Mishina, M., Konno, T., Nakai, J., Bujo, H., Mori, Y., Fukuda, K., and Numa, S. (1988) Rings of negatively charged amino acids determine the acetylcholine receptor channel conductance. *Nature 335*, 645-648.

77. Akabas, M. H., and Karlin, A. (1995) Identification of acetylcholine receptor channel-lining residues in the M1 segment of the alpha-subunit. *Biochemistry 34*, 12496-12500.
78. Akabas, M. H., Kaufmann, C., Archdeacon, P., and Karlin, A. (1994) Identification of acetylcholine receptor channel-lining residues in the entire M2 segment of the alpha subunit. *Neuron 13*, 919-927.
79. Zhang, H., and Karlin, A. (1998) Contribution of the beta subunit M2 segment to the ion-conducting pathway of the acetylcholine receptor. *Biochemistry 37*, 7952-7964.
80. Zhang, H., and Karlin, A. (1997) Identification of acetylcholine receptor channel-lining residues in the M1 segment of the beta-subunit. *Biochemistry 36*, 15856-15864.
81. Wilson, G., and Karlin, A. (2001) Acetylcholine receptor channel structure in the resting, open, and desensitized states probed with the substituted-cysteine-accessibility method. *Proc. Natl. Acad. Sci. U.S.A. 98*, 1241-1248.
82. Wilson, G. G., and Karlin, A. (1998) The location of the gate in the acetylcholine receptor channel. *Neuron 20*, 1269-1281.
83. Purohit, Y., and Grosman, C. (2006) Block of muscle nicotinic receptors by choline suggests that the activation and desensitization gates act as distinct molecular entities. *J. Gen. Physiol. 127*, 703-717.
84. Auerbach, A., and Akk, G. (1998) Desensitization of mouse nicotinic acetylcholine receptor channels. A two-gate mechanism. *J. Gen. Physiol. 112*, 181-197.
85. Labarca, C., Nowak, M. W., Zhang, H., Tang, L., Deshpande, P., and Lester, H. A. (1995) Channel gating governed symmetrically by conserved leucine residues in the M2 domain of nicotinic receptors. *Nature 376*, 514-516.
86. Cymes, G. D., and Grosman, C. (2008) Pore-opening mechanism of the nicotinic acetylcholine receptor evinced by proton transfer. *Nat. Struc. Mol. Biol. 15*, 389-396.
87. Cymes, G. D., Ni, Y., and Grosman, C. (2005) Probing ion-channel pores one proton at a time. *Nature 438*, 975-980.
88. Corry, B. (2006) An energy-efficient gating mechanism in the acetylcholine receptor channel suggested by molecular and Brownian dynamics. *Biophys. J. 90*, 799-810.
89. Beckstein, O., and Sansom, M. S. (2006) A hydrophobic gate in an ion channel: the closed state of the nicotinic acetylcholine receptor. *Phys. Biol. 3*, 147-159.
90. Bouzat, C., Gumilar, F., Spitzmaul, G., Wang, H. L., Rayes, D., Hansen, S. B., Taylor, P., and Sine, S. M. (2004) Coupling of agonist binding to channel gating in an ACh-binding protein linked to an ion channel. *Nature 430*, 896-900.
91. Lee, W. Y., and Sine, S. M. (2005) Principal pathway coupling agonist binding to channel gating in nicotinic receptors. *Nature 438*, 243-247.
92. Mukhtasimova, N., and Sine, S. M. (2007) An intersubunit trigger of channel gating in the muscle nicotinic receptor. *J. Neurosci. 27*, 4110-4119.
93. Mukhtasimova, N., Free, C., and Sine, S. M. (2005) Initial coupling of binding to gating mediated by conserved residues in the muscle nicotinic receptor. *J. Gen. Physiol. 126*, 23-39.
94. Auerbach, A. (2007) How to turn the reaction coordinate into time. *J. Gen. Physiol. 130*, 543-546.
95. Sine, S. M., and Engel, A. G. (2006) Recent advances in Cys-loop receptor structure and function. *Nature 440*, 448-455.
96. Purohit, P., Mitra, A., and Auerbach, A. (2007) A stepwise mechanism for acetylcholine receptor channel gating. *Nature 446*, 930-933.

97. Purohit, P., and Auerbach, A. (2007) Acetylcholine receptor gating at extracellular transmembrane domain interface: the "pre-M1" linker. *J. Gen. Physiol. 130*, 559-568.
98. Purohit, P., and Auerbach, A. (2007) Acetylcholine receptor gating: movement in the alpha-subunit extracellular domain. *J. Gen. Physiol. 130*, 569-579.
99. Jha, A., Cadugan, D. J., Purohit, P., and Auerbach, A. (2007) Acetylcholine receptor gating at extracellular transmembrane domain interface: the cys-loop and M2-M3 linker. *J. Gen. Physiol. 130*, 547-558.
100. Cadugan, D. J., and Auerbach, A. (2007) Conformational dynamics of the alphaM3 transmembrane helix during acetylcholine receptor channel gating. *Biophys. J. 93*, 859-865.
101. Mitra, A., Tascione, R., Auerbach, A., and Licht, S. (2005) Plasticity of acetylcholine receptor gating motions via rate-energy relationships. *Biophys. J. 89*, 3071-3078.
102. Mitra, A., Cymes, G. D., and Auerbach, A. (2005) Dynamics of the acetylcholine receptor pore at the gating transition state. *Proc. Natl. Acad. Sci. U.S.A. 102*, 15069-15074.
103. Mitra, A., Bailey, T. D., and Auerbach, A. L. (2004) Structural dynamics of the M4 transmembrane segment during acetylcholine receptor gating. *Structure 12*, 1909-1918.
104. Chakrapani, S., Bailey, T. D., and Auerbach, A. (2004) Gating dynamics of the acetylcholine receptor extracellular domain. *J. Gen. Physiol. 123*, 341-356.
105. Chakrapani, S., Bailey, T. D., and Auerbach, A. (2003) The role of loop 5 in acetylcholine receptor channel gating. *J. Gen. Physiol. 122*, 521-539.
106. Cymes, G. D., Grosman, C., and Auerbach, A. (2002) Structure of the transition state of gating in the acetylcholine receptor channel pore: a phi-value analysis. *Biochemistry 41*, 5548-5555.
107. Grosman, C., Zhou, M., and Auerbach, A. (2000) Mapping the conformational wave of acetylcholine receptor channel gating. *Nature 403*, 773-776.
108. Elenes, S., and Auerbach, A. (2002) Desensitization of diliganded mouse muscle nicotinic acetylcholine receptor channels. *J. Physiol. 541*, 367-383.
109. Giniatullin, R., Nistri, A., and Yakel, J. L. (2005) Desensitization of nicotinic ACh receptors: shaping cholinergic signaling. *Trends Neurosci. 28*, 371-378.
110. Jones, M. V., and Westbrook, G. L. (1996) The impact of receptor desensitization on fast synaptic transmission. *Trends Neurosci. 19*, 96-101.
111. Elenes, S., Ni, Y., Cymes, G. D., and Grosman, C. (2006) Desensitization contributes to the synaptic response of gain-of-function mutants of the muscle nicotinic receptor. *J. Gen. Physiol. 128*, 615-627.
112. Song, X. Z., and Pedersen, S. E. (2000) Electrostatic interactions regulate desensitization of the nicotinic acetylcholine receptor. *Biophys. J. 78*, 1324-1334.
113. Hamill, O. P., Marty, A., Neher, E., Sakmann, B., and Sigworth, F. J. (1981) Improved patch-clamp techniques for high-resolution current recording from cells and cell-free membrane patches. *Pflug. Arch. 391*, 85-100.
114. Sakmann, B., and Neher, E. (1995) *Single-channel recording*, 2nd ed., Plenum Press, New York.
115. Monod, J., Wyman, J., and Changeux, J. P. (1965) On the Nature of Allosteric Transitions: a Plausible Model. *J. Mol. Biol. 12*, 88-118.

116. Hawkes, A. G., Jalali, A., and Colquhoun, D. (1992) Asymptotic distributions of apparent open times and shut times in a single channel record allowing for the omission of brief events *Phil. Trans. R. Soc. Lon. 337*, 383-404.
117. Qin, F., Auerbach, A., and Sachs, F. (1996) Estimating single-channel kinetic parameters from idealized patch-clamp data containing missed events. *Biophys. J. 70*, 264-280.
118. Qin, F., Auerbach, A., and Sachs, F. (1997) Maximum likelihood estimation of aggregated Markov processes. *Proc. Biol. Sci. 264*, 375-383.
119. Qin, F., and Li, L. (2004) Model-based fitting of single-channel dwell-time distributions. *Biophys. J. 87*, 1657-1671.
120. Sigworth, F. J., and Sine, S. M. (1987) Data transformations for improved display and fitting of single-channel dwell time histograms. *Biophys. J. 52*, 1047-1054.

Tables I.1. Currently available PDB structures of the acetylcholine receptor (AChR) or acetylcholine binding protein (AChBP).

PDB	Species	Protein	Bound Ligand	(Å)
1I9B	*Lymnaea stagnalis*	AChBP	**HEPES**[1]	2.7
1OED	*Torpedo Marmorata*	AChR		4
1UV6	*Lymnaea stagnalis*	AChBP	**Carbamylcholine**	2.5
1UW6	*Lymnaea stagnalis*	AChBP	**Nicotine**	2.2
1UX2	*Lymnaea stagnalis*	AChBP		2.2
1YI5	*Aplysia californica*	AChBP	**α-Cobratoxin**[2]	4.2
2BYQ	*Aplysia californica*	AChBP	**Epibatidine**	3.4
2BJ0	*Bulinus truncatus*	AChBP		2
2BR7	*Aplysia californica*	AChBP	**HEPES**	3
2BR8	*Aplysia californica*	AChBP	**α-Conotoxin PNIA**	2.4
2BG9	*Torpedo Marmorata*	AChR		4
2BYN	*Aplysia californica*	AChBP		2
2BYP	*Aplysia californica*	AChBP	**α-Conotoxin IMI**	2.1
2BYR	*Aplysia californica*	AChBP	**Methyllycaconitine**	2.5
2BYS	*Aplysia californica*	AChBP	**Lobeline**	2
2C9T	*Aplysia californica*	AChBP	**α-Conotoxin IMI**	2.3
2UZ6	*Aplysia californica*	AChBP	**α-Conotoxin**	2.4
2QC1	*Mus musculus*	AChR α1 ECD[3]	**α-Bungarotoxin**	1.9
2PGZ	*Aplysia californica*	AChBP	**Cocaine**	1.8
2PH9	*Aplysia californica*	AChBP	**Galanthamine**	2.9
3C84	*Aplysia californica*	AChBP	**Thiacloprid**	1.9
3C79	*Aplysia californica*	AChBP	**Imidacloprid**	2.5
2ZJU	*Lymnaea stagnalis*	AChBP	**Imidacloprid**	2.6
2ZJV	*Lymnaea stagnalis*	AChBP	**Clothianidin**	2.7

[1] Agonist are shown in blue.
[2] Antagonists are shown in red.
[3] The extracellular ligand-binding domain of the AChR α1 subunit.

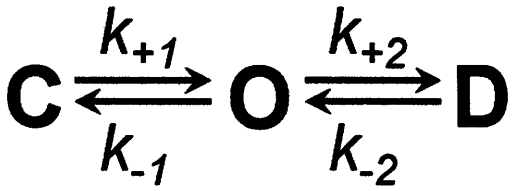

Scheme I.1. A simple kinetic model for ion channel conformational changes. "C", closed; "O", open; "D", desensitized; $k_{+/-n}$, s^{-1}.

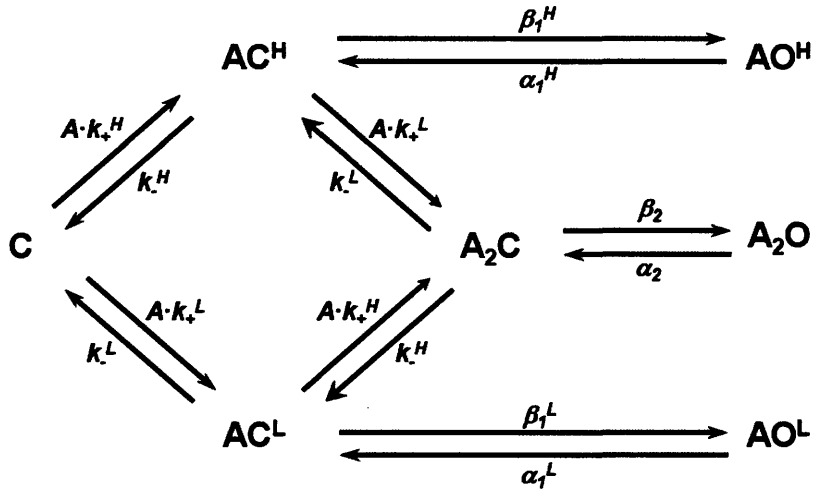

Scheme I.2. A general kinetic model derived from MWC theory of AChR concerted allosteric conformational changes. Conformational states: C, closed; O, open; A, bound agonist. Rate constants: k_+, agonist association, M^{-1} s^{-1}; k_-, agonist dissociation, s^{-1}; β_1, monoliganded opening rate, s^{-1}; α_1, monoliganded closing rate, s^{-1}; β_2, diliganded opening rate, s^{-1}; α_2, diliganded closing rate, s^{-1}; H, high affinity site; L, low affinity site.

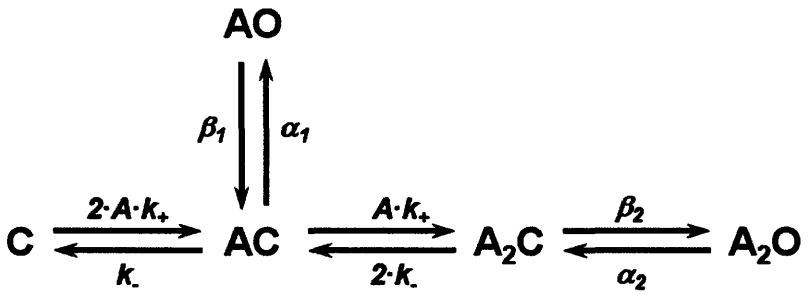

Scheme I.3. A simplified AChR kinetic model.

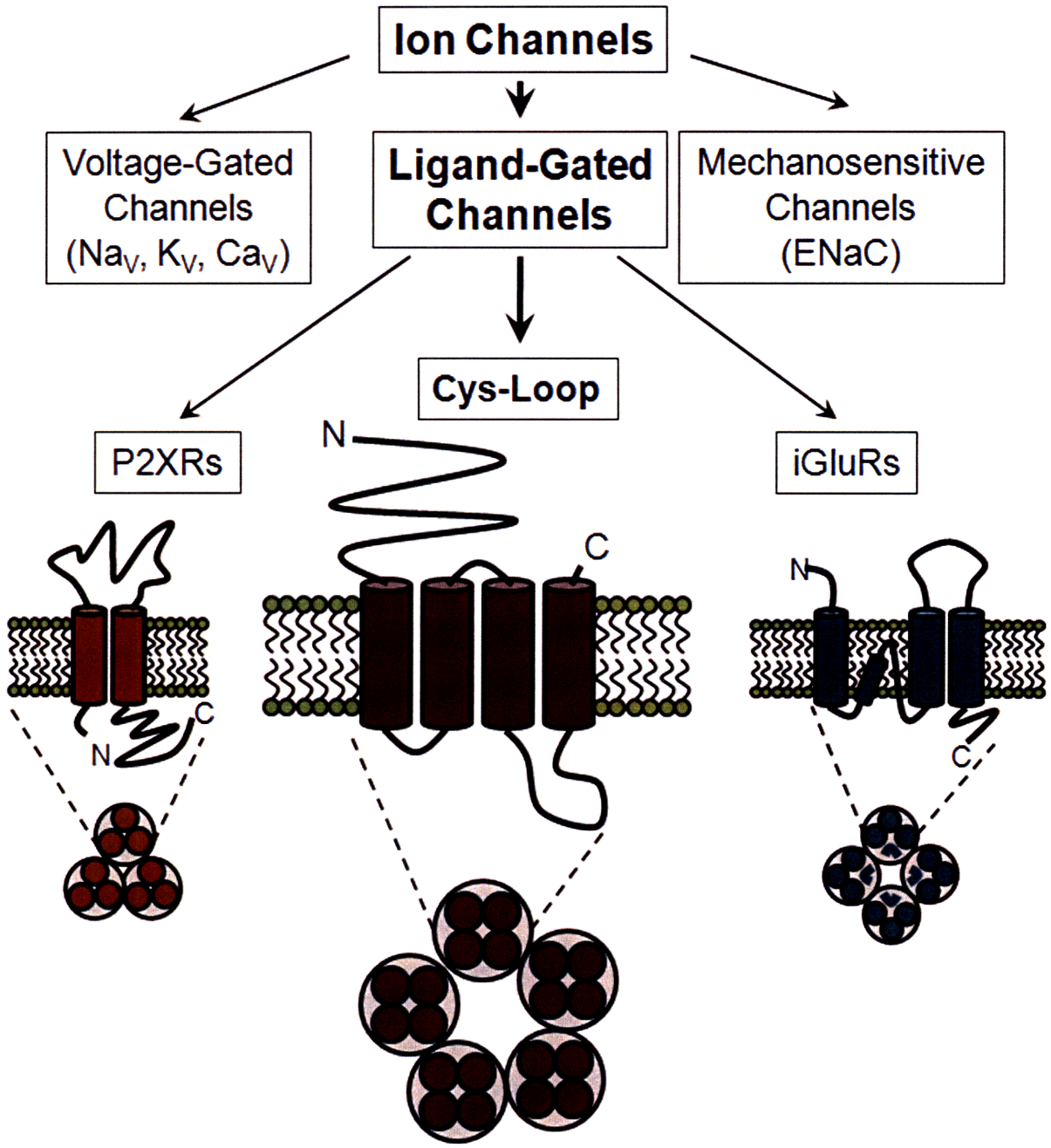

Figure I.1. Ligand-gated ion channels are one class of ion channels. The cys-loop receptors are one of three gene superfamilies of ligand-gated ion channels. Cys-loop receptors consist of five homologous subunits arranged pseudo-symmetrically around the ion conduction pore. Each subunit has an N-terminal ligand-binding domain and four transmembrane helices.

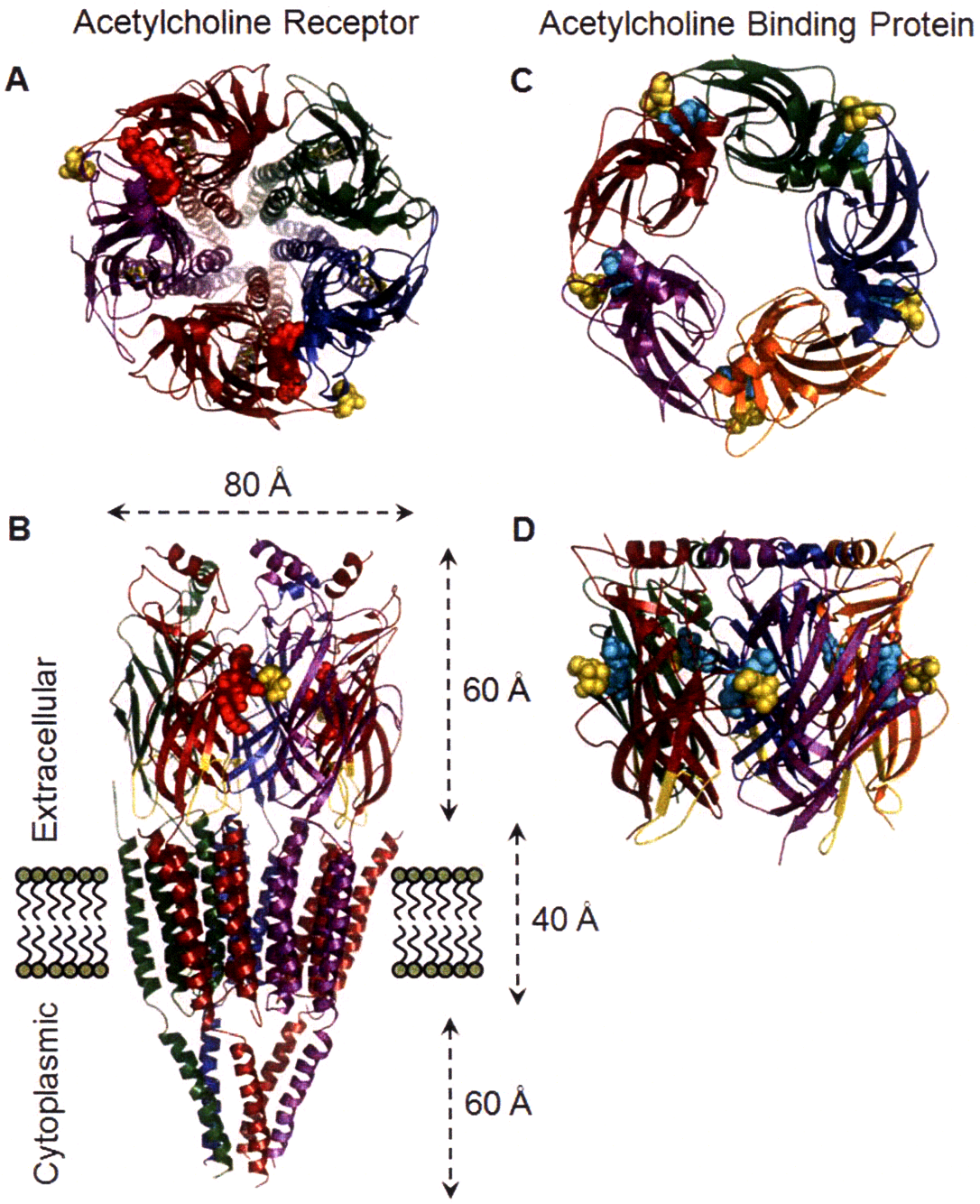

Figure I.2. The AChR cryoelectron structure at 4 Å resolution (PDB 2BG9) and the AChBP x-ray structure at 2.7 Å resolution (PBB 1I9B). (A) A view of the muscle-type AChR from the extracellular side. The α-subunits are red, the β-subunit is green, the δ-subunit is blue, and the ε-subunit is purple. (B) A side view of the AChR. (C) A top view of the homomeric AChBP. The subunits are colored arbitrarily. The location of the transmitter binding sites are shown by the cyan spheres. (D) A side view of the AChBP. The locations of the TBSs are indicated by colored spheres. The cys-loop is shown as a yellow loop.

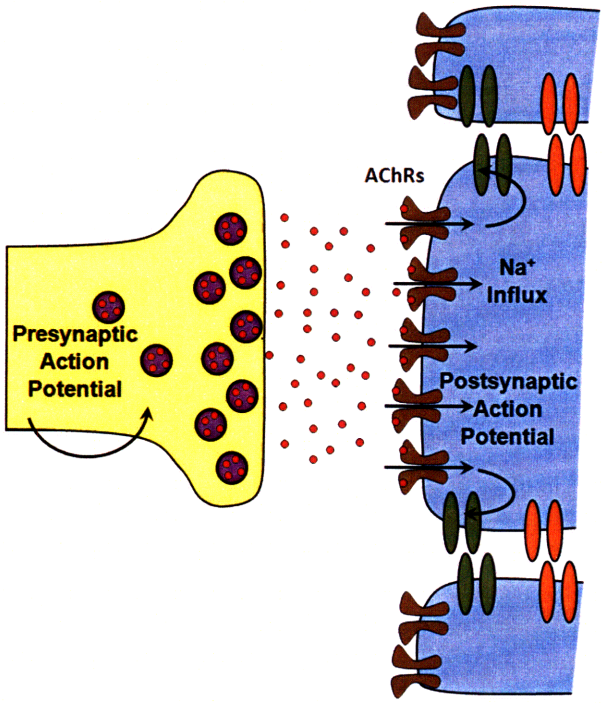

Figure I.3. AChRs at the neuromuscular junction are models for signal transduction at fast chemical synapses. The presynaptic nerve terminal is yellow, and the postsynaptic muscle endplate is blue. Opening of AChRs (brown) depolarizes the membrane. The postsynaptic action potential is propagated by voltage-gated sodium channels (green), ultimately opening voltage-gated calcium channels (orange).

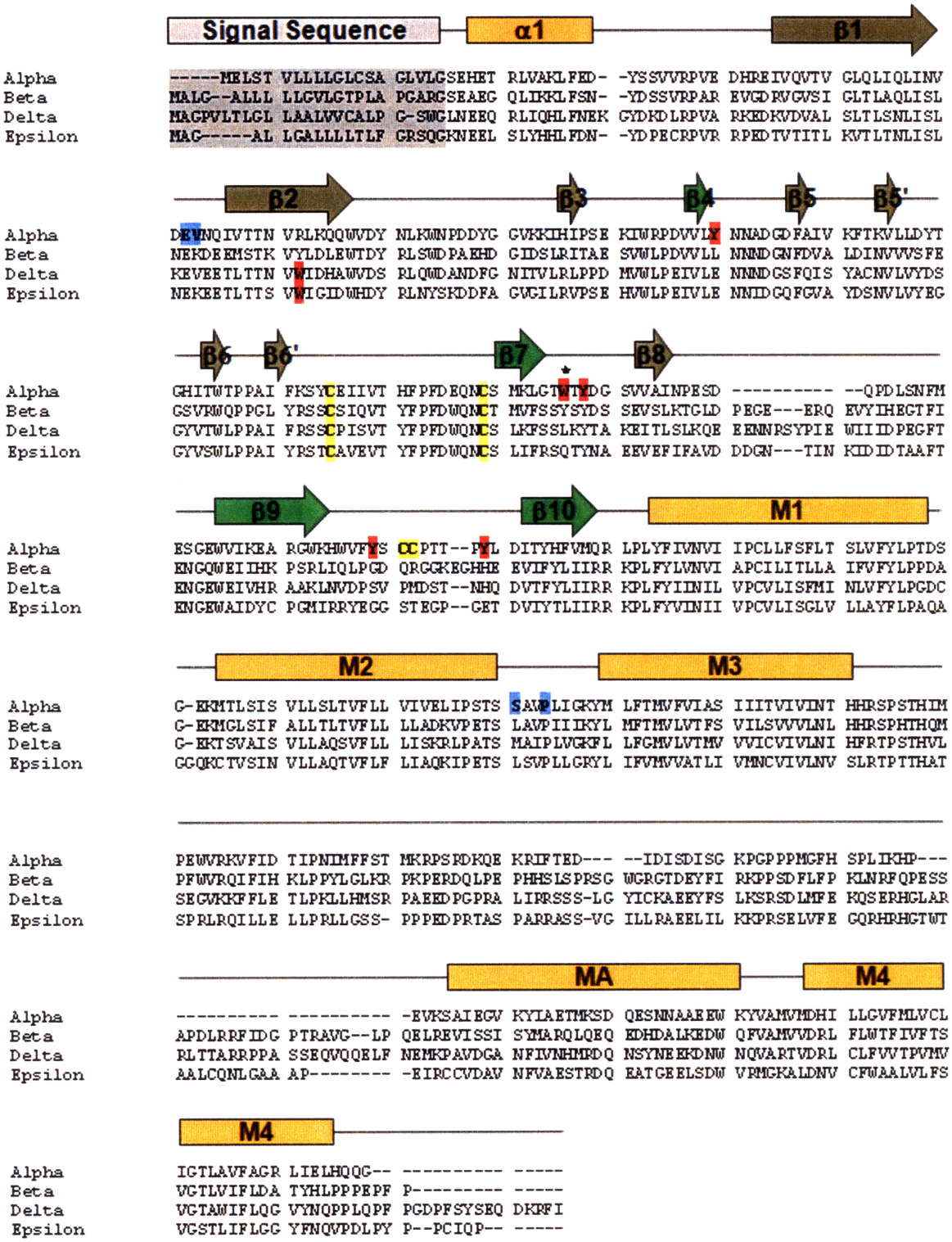

Figure I.4. Alignment of the adult mouse muscle-type AChR subunit protein sequences. The *Torpedo* and mouse α-subunits are 71% identical, and the *Torpedo* sequence and structure were used to annotate the sequence: α-helices, orange; inner β-sheets, green; outer β-sheets, tan; disulfide, yellow; TBS aromatic residues, red; residues at the domain interface, blue.

Figure I.5. A side view of the αδ subunit interface. The α-subunit is color coded according to Figure I.4, and the δ-subunit is grey.

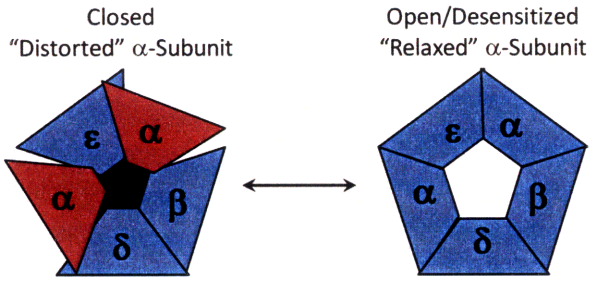

Figure I.6. Cartoon explanation of the rotation of the α-subunits.

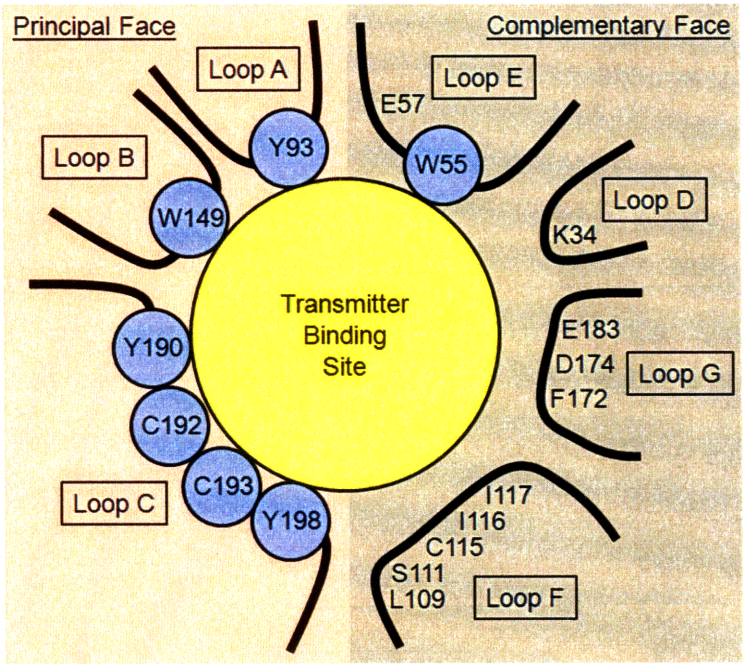

Figure I.7. Cartoon of the transmitter binding site and the loops contributing binding determinants.

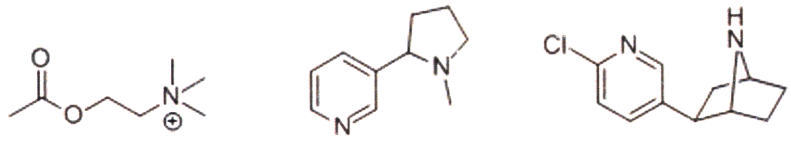

Figure I.8. Acetylcholine receptor agonists containing ammonium groups.

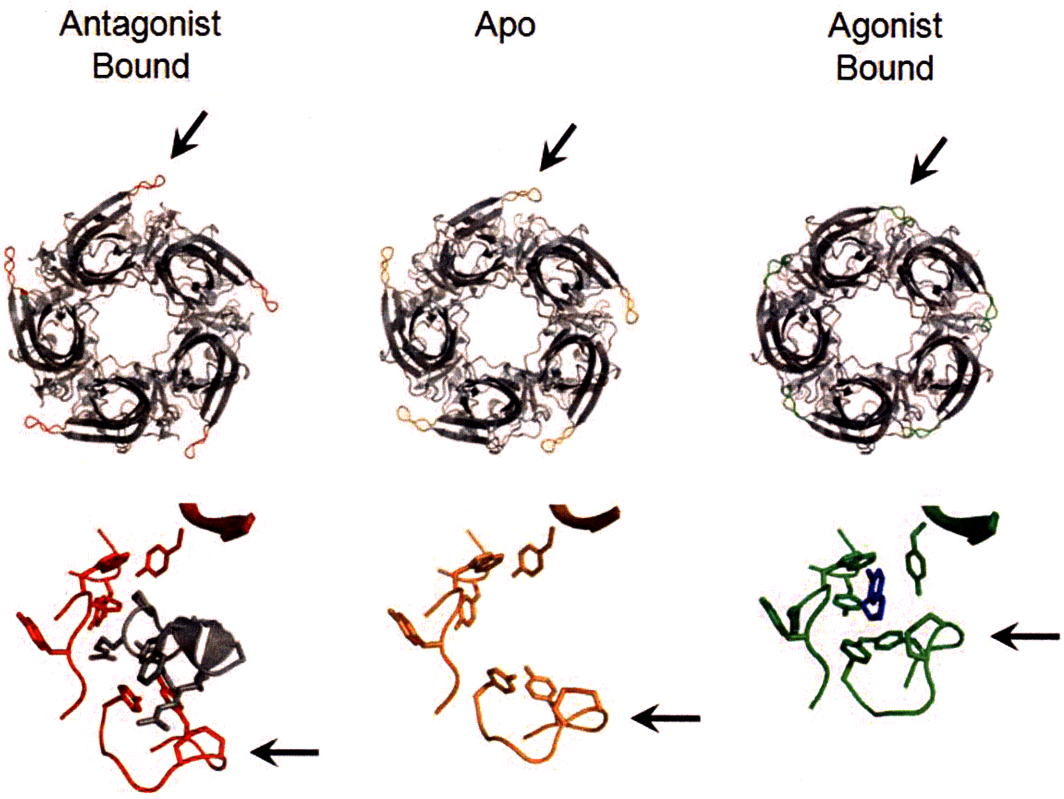

Figure I.9. AChBP models. Loop C (arrow) is positioned away from the agonist binding site in the antagonist-bound (red, PDB 2BYP) and apo (orange, PDB 2BYN) structures. Loop C caps the agonist-bound site (green, PDB 2BYQ). Top row: Top view of the AChBPs. Bottom row: Close-up view of a TBS. In the antagonist-bound structure (red, left), the peptide competitive antagonist α-conotoxin IMI is shown in grey.

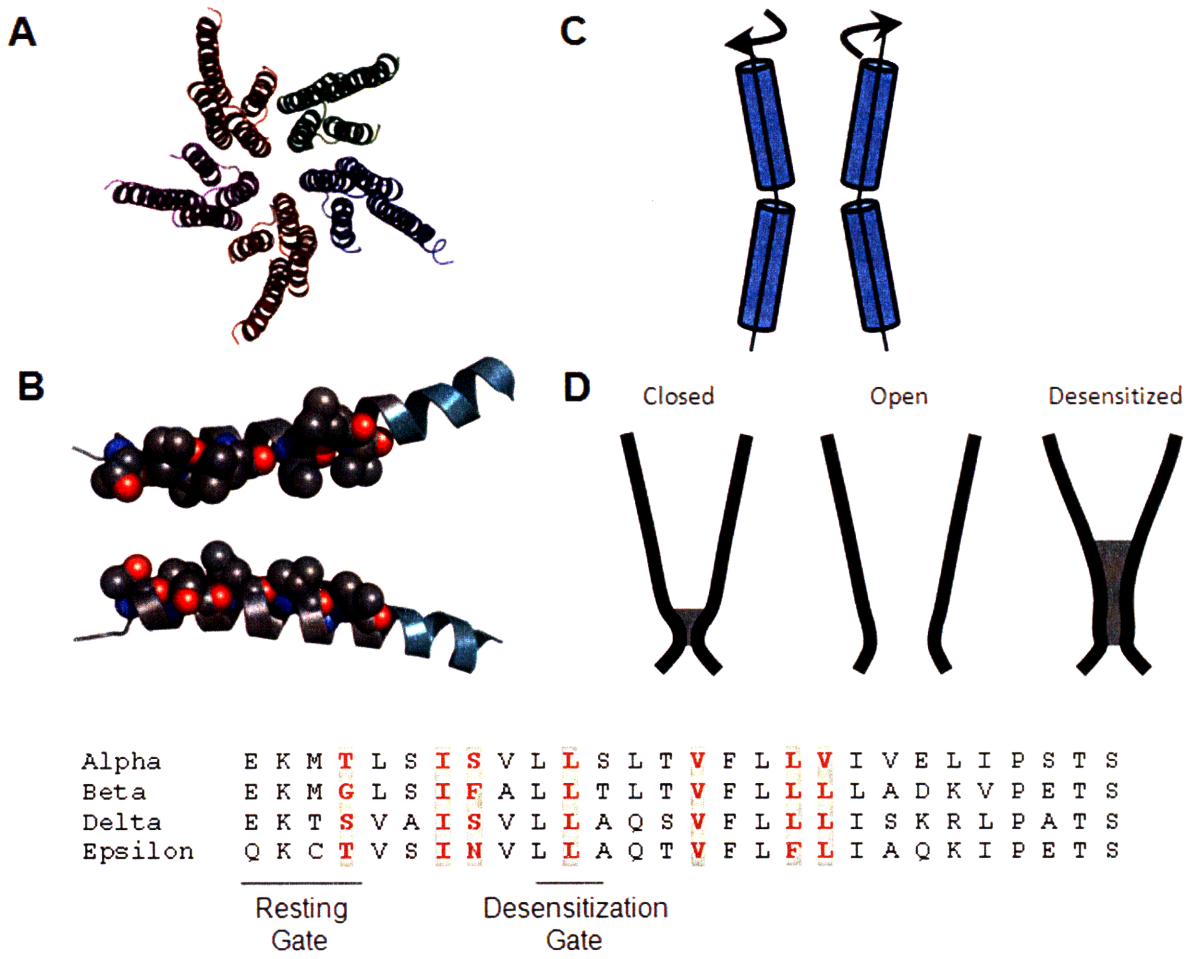

Figure I.10. The muscle-type AChR transmembrane domain. (A) View from the extracellular opening. (B) A side view of αM2 helices. The extracellular side to the left. Highlighted residues in the sequence alignment are shown as spheres (*87*). The light blue region is above the lipid bilayer. (C) A proposed mechanism for pore gating involves rotation of the M2 helices, causing widening of the pore. (D) Diagram of approximate locations of the closed and desensitized gates as determined by SCAM.

Figure I.11. Residues important for coupling agonist binding to pore opening: the initial trigger, blue; the intersubunit trigger, green; the principal trigger, red; loops, yellow.

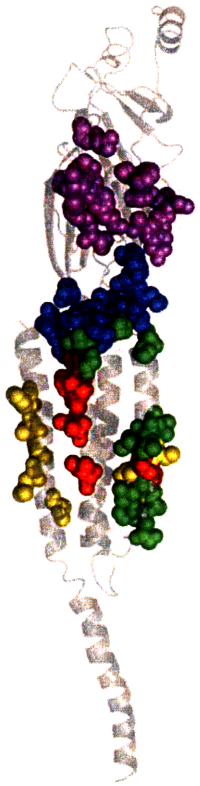

Figure I.12. Color-coded Φ-value map of the α-subunit demonstrating the conformational wave: $0.9 \leq \Phi \leq 1$, purple; $0.7 \leq \Phi \leq 0.9$, blue; $0.6 \leq \Phi \leq 0.7$, green; $0.4 \leq \Phi \leq 0.6$, yellow; $0 \leq \Phi \leq 0.4$, red.

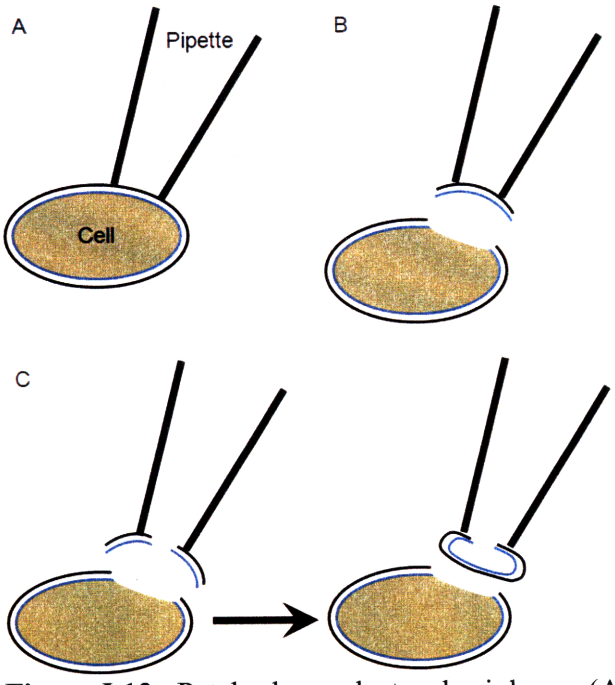

Figure I.13. Patch-clamp electrophysiology. (A) Cell-attached mode. (B) Inside-out mode. (C) Outside-out mode.

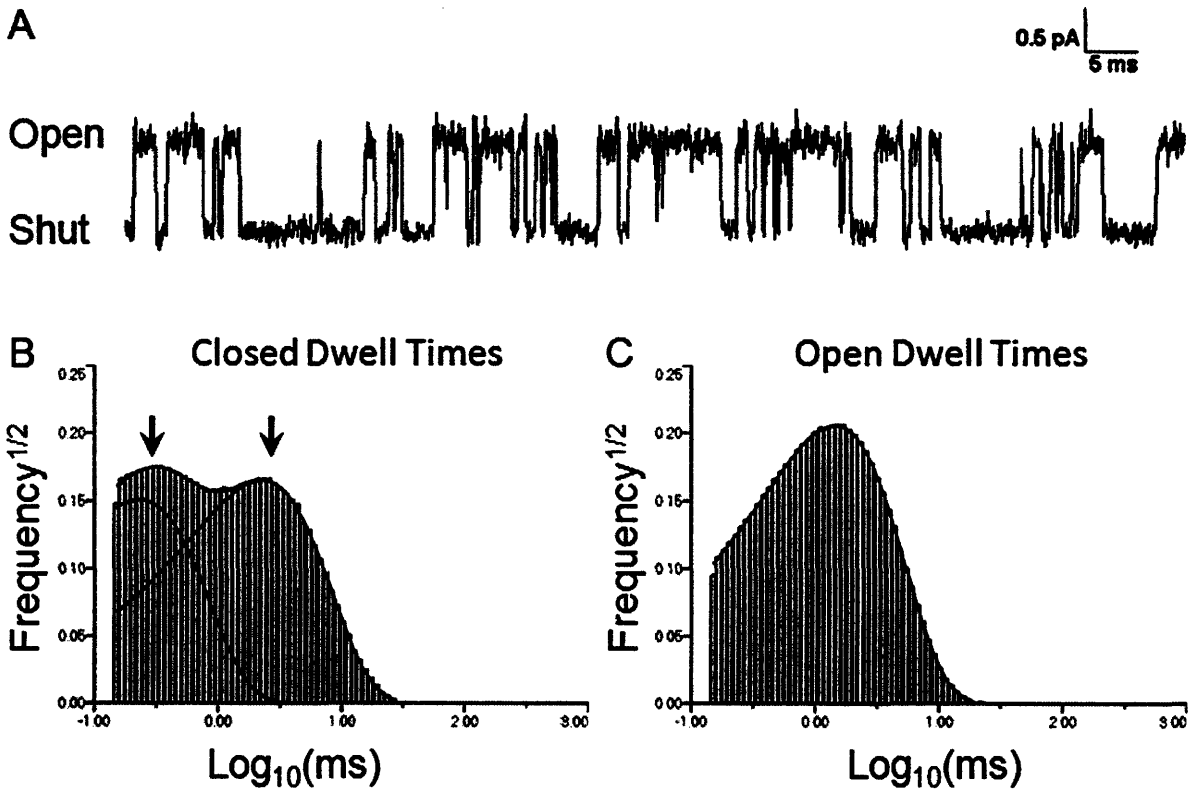

Figure I.14. (A) An example of a single-channel record. Openings are upward deflections in current. (B) An example of the closed dwell-time distribution when there are two non-conducting states (arrows). The dwell-time distribution is plotted using the Sigworth-Sine transformation (*120*): the histogram is plotted with a $\log_{10}$ x-axis with 0.1 log unit bin widths, and the y-axis is the square-root of the frequency. This type of plot is useful for sums of exponentials because each exponential appears as a peak. (C) An example of the open dwell-time distribution with only one conducting state.

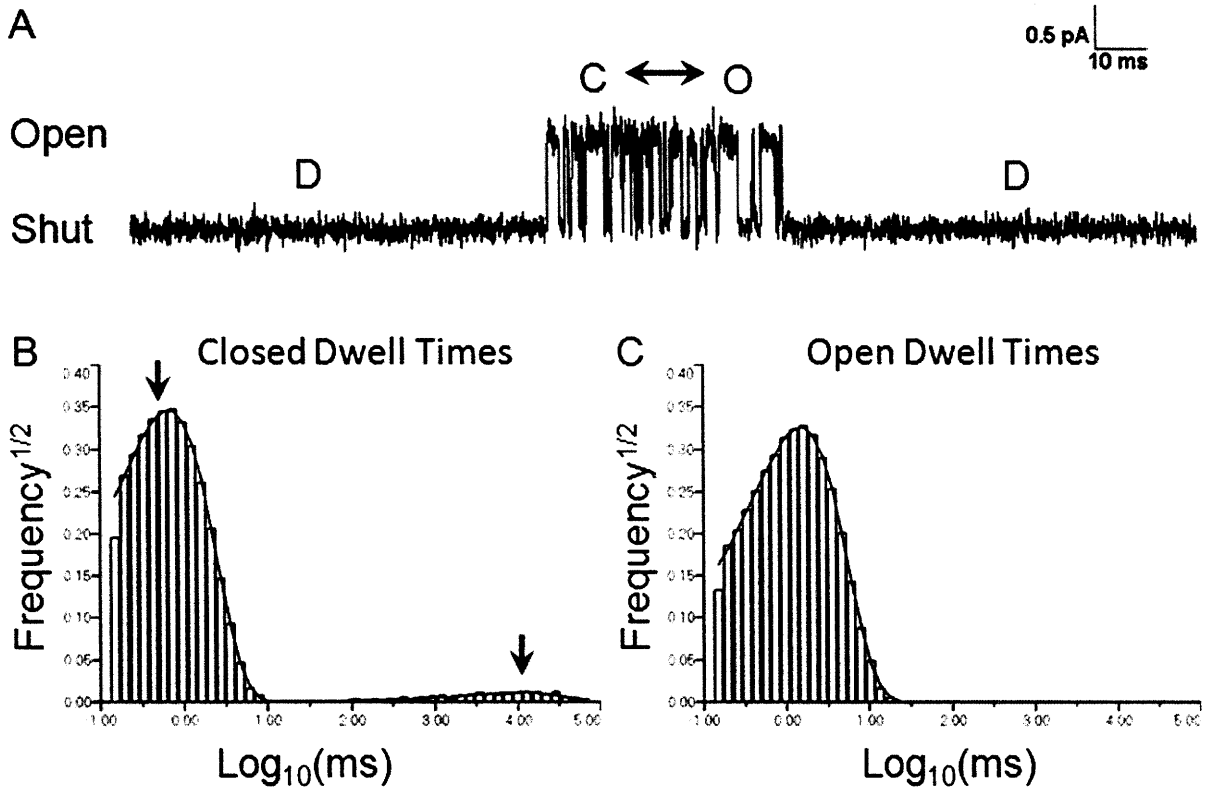

Figure I.15. (A) An example of a single-channel cluster. (B) The closed dwell-time distribution shows the closed and desensitized components are well-separated (arrows). (C) The open dwell-time distribution.

Chapter II.

A Structure-Activity Relationship Between Organic Cations, Binding, and Gating of the Acetylcholine Receptor: Cation-π Binding Energy as a Parameter for Distinguishing Agonists From Antagonists

II.A Summary

Cation-π interactions have been shown to be important for activation of acetylcholine receptors by strong agonists. Cationic agonists interact with aromatic residues found in the transmitter binding sites. Using a series of structurally related organic cations, we demonstrate that the efficiency for channel opening, the gating energy, is strongly correlated with the cation-π energy. This suggests that cation-π interactions contribute significantly to the open-state affinity of these cations. We propose that the cation-π binding energy may be a useful metric for quantitative structure-activity relationships used to guide the design of agonists and antagonists with therapeutic potential to treat nicotine addiction, neuromuscular and neurological disorders.

II.B Introduction

Cation-π interactions have been shown to be important for the function of nicotinic acetylcholine receptors (AChRs) and other members of the cys-loop superfamily (*1, 2*). These interactions are formed between cationic small molecules and aromatic residues at the transmitter binding sites (TBSs) for these receptors. The cation-π binding energy therefore may be a useful parameter in predicting the action of a candidate molecule as either an agonist or competitive antagonist.

AChRs are involved in a broad range of synaptic activities through the central and peripheral nervous systems, and as a result they are the targets of therapeutic drugs for a variety of conditions. Structure-activity relationships (SARs) continue to be used to develop AChR antagonists that can be used as muscle relaxants (*3*). However, using parameters such as molecular shape, charge, and hydrogen bonding ability, SARs have had limited success in guiding drug design for neuromuscular blocking agents. In the brain, AChRs have been proposed to be targets for treating nicotine addiction, depression, and a variety of neurological disorders (*4*). SARs for these drug candidates are typically centered on derivatives of AChR agonists or antagonists derived from natural sources, such as nicotine or epibatidine. The small

molecule drugs that bind AChRs are structurally very diverse. The identification of simple, independent parameters which correlate with binding or gating would therefore be useful for improving SAR guided drug design.

Structural and biochemical studies of the AChR and the acetylcholine binding protein (AChBP) have provided a model for the ligand-binding process and identified several aromatic residues that are important for binding charged agonists and competitive antagonists (*5-12*). The binding site "aromatic cage" consists of residues αTyr93, αTrp149, αTyr190, αTyr198, and δTyr57 (or γ/εTyr55). Residues αTyr190 and αTyr198 are part of Loop C, a binding determinant on the α subunit. In the apo-AChBP structure, Loop C is positioned away from the TBS cavity. In the agonist-bound AChBP, Loop C is displaced approximately 10 Å from its apo-position towards the TBS cavity (*8*). In this conformation, Loop C "caps" the agonist-bound binding site, and residues αTyr190 and αTyr198 come in close proximity of the bound molecule. In this arrangement, the aromatic cage is contracted, increasing favorable contacts with the agonist molecule (**Figure II.1**). In contrast, comparison of apo-AChBP and agonist-bound AChBP structures indicate that αTrp149 found in Loop B does not change conformation significantly. Molecular dynamics simulations on nanosecond timescales also have shown that the backbone of αTrp149 is relatively stable when a simulated receptor relaxes from an agonist-bound conformation (*13*).

Using unnatural amino acid mutagenesis, αTrp149 was shown to form cation-π interactions with cholinergic agonists (*14, 15*). Substitution of fluorine in the indole ring of this residue increased the concentration for half-maximal AChR activation, the EC_{50}, for epibatidine and acetylcholine. The observed increase in EC_{50} correlated with the calculated decrease in cation-π binding ability of the fluorinated analogs. A similar correlation was not observed for the other binding site aromatic residues, suggesting αTrp149 is primarily responsible for the cation-π interaction (*15-17*).

EC_{50}, analogously to K_M for enzymes, reflects both binding and conformational or chemical equilibria. For an ion channel EC_{50}, the equilibrium for the open-closed conformational change, called gating, can be a significant component. Therefore, the correlation between EC_{50} and cation-π binding energy is consistent with three possibilities. In the first case, the cation-π energy could contribute entirely to the closed-state affinity. The cation-π interaction

could fully form when agonist binds the closed state, and it could remain constant in strength during AChR gating. In the second case, the cation-π energy could contribute to both binding and gating. The cation-π interaction could form in the closed-state, but strengthen in the open state. In the third case, the cation-π energy could contribute entirely to the open-state affinity. Agonist binding to the closed AChR would not involve the cation-π interaction. Instead, the cation-π interaction would only exist in the open state, and the gating equilibrium would correlate with cation-π energy. In all of these three cases, attenuation of the cation-π energy would increase the EC_{50}.

It has been hypothesized that the correlation between EC_{50} and cation-π energy primarily reflects contributions to binding (*14*). Both 5-hydroxytryptamine (5-HT) and acetylcholine (ACh) are strong agonists for the serotonin channel, $5\text{-}HT_{3A}R$. For both 5-HT and ACh, channel activation is attenuated by fluorination of αTrp149, and EC_{50}'s are linearly correlated to calculated cation-π binding energies for the fluorination series. For all combinations of agonist and mutated receptor, maximal currents of similar magnitude were observed when exposed to saturating concentrations of agonist, suggesting gating efficiency was not severely compromised (*18*). However, with the strong agonists used in these studies, changes in gating efficiency could lead to relatively small changes in channel maximal currents. The previous studies therefore did not rule out the possibility that the interaction between agonist and αTrp149 changes with gating (*14, 15, 18*). Currently, there are no definitive models for the agonist-bound closed and open AChR states, and there is no direct structural data to resolve this issue. Although fluorination was introduced at a precise binding site location, the AChR is an allosteric protein complex. Perturbations localized to the binding site do not necessarily affect agonist affinity only, and likewise perturbations far from the binding site do not necessarily affect gating only. For example, mutations αY93F and αY190F affect both binding and gating, and mutation αY198F affects gating primarily (*19-21*). In contrast mutation αN217K in the M1 transmembrane helix primarily affects binding (*22*).

If the cation-π binding energy is strongly correlated to closed-state affinity, it may be a useful parameter in structure-activity relationships that distinguish agonists from competitive antagonists. A strong agonist exhibits a high affinity for the closed state and an even higher affinity for the open state, promoting efficient gating. A strong competitive antagonist exhibits a

high affinity for the closed state but not for the open state, making gating inefficient. Establishing metrics for closed-state affinity and open-state affinity could aid drug design. The cation-π binding energy appears to be a good candidate as a useful metric for closed-state affinity and possibly open-state affinity.

We hypothesized that the ability of an organic cation to form a cation-π interaction will predict its closed-state affinity for the muscle-type AChR. We tested this hypothesis by measuring agonist binding affinity (K_D) and gating efficiency (Θ_2) for activation of mouse AChRs by organic cations. Single-channel recordings are used to directly measure microscopic rate constants and equilibria. By using a series of structurally related organic cations, we probe the role of the aromatic cage in agonist binding and gating, without having to deconvolve the effect of secondary elements such as the ester moiety of ACh. For the set of compounds tested, there is a strong correlation between the ab initio calculated cation-π binding energy and Θ_2 and a weaker correlation with K_D. These results suggests that secondary structural elements may play a role in positioning the cationic center. We conclude that cation-π binding energy has the potential to be used as a parameter in designing AChR agonists and antagonists.

II.C Materials and Methods

Chemicals.

Tetramethylammonium (TMA) chloride, triethylmethylammonium (TEMA) chloride, and tetramethylphosphonium (TMP) bromide were from Aldrich. Ethyltrimethylammonium (ETMA) iodide was from TCI. Dimethyldiethylammonium (DEDMA) hydroxide from Fluka was neutralized with hydrochloric acid. Cell culture reagents were from Invitrogen (Carlsbad, CA). Plasmids for expression of the adult mouse α, β, δ, and ε subunits were generously provided by Professor Anthony Auerbach at SUNY Buffalo. The plasmids contain the pRGB4 backbone, with a CMV promoter (*23*).

Cell culture.

HEK-293 human embryonic kidney cells (ATCC CRL-1573) were maintained in Dulbecco's Minimum Essential Media (DMEM) supplemented with 10% Fetal Bovine Serum (FBS) at 37°C in a 5% CO_2 humidified atmosphere. Cells were transfected at 40-60% confluency using the method of calcium phosphate precipitation according to previously

published protocols (*24*) as follows. For one 35 mm plate, a total of 3.5 μg of plasmid DNA was used in a mass ratio of 2:1:1:1 of α:β:δ:ε subunits. Plasmids were mixed in 87.5 μL of 250 mM $CaCl_2$ on ice. The plasmid solution was added drop wise to ice-cold 87.5 μL of 50 mM HEPES, pH 7.05, 280 mM NaCl, 1.5 mM Na_2HPO_4. The layered mixture was incubated for 10 minutes at room temperature without disturbance, and then it was mixed. The mixture was incubated for an additional 15 minutes at room temperature and then mixed again, forming a fine DNA precipitate that is visible under the microscope. The precipitate was added drop wise to cells. Media was changed 8-30 hours after addition of DNA, and patch-clamp experiments were conducted 24-72 hours after media change. For transfection of several dishes, the recipe could be multiplied up to 4-fold for a single mixture; however, use of more than 350 μL of plasmid solution inhibits the formation of precipitant.

Justification for use of the αG153S mutant.

The αG153S mutation is a gain-of-function mutation originally identified from a patient diagnosed with slow-channel congenital myasthenia (genetic disease causing muscle weakness). It has been shown to primarily increase agonist affinity (*25*). This mutation is at the binding site and is proposed to be important for the hydrogen bonding network and allosteric transduction mechanism (*26*). Although this mutation occurs at the binding site, it is not part of the aromatic cage. The αG153S mutation is not likely to directly affect the cation-π interaction between αTrp149 and the agonist, as αTrp149 has been shown to be primarily stabilized by αD89 (*27, 28*). Furthermore, the cation-π interaction has shown to be robust to variations in sequence and structure, existing in several different cys-loop receptors (*29*). We therefore use this mutant assuming its effects are equivalent for the series of agonists used here. Of the series, only TMA is a highly efficacious agonist for the wild-type AChR (*30-32*). Furthermore, high concentrations of these cations causes severe open-channel block. The advantage of using the αG153S mutant is that it enables single-channel clusters to be recorded and analyzed for the series at lower agonist concentrations, where block is not nearly as severe and can be compensated for in our analysis. As a control to demonstrate that the mutation affects the series of cations equivalently, a rate-equilibrium free energy relationship (REFER) is examined in the **Results**. The REFER is shown to be linear with a slope approximately 1 as has been observed previously for energetic changes at the TBSs, due to mutation or ligand variation (*33, 34*).

Single-channel recordings.

Single-channel recording was performed in the cell-attached mode according to previously published protocols (*35, 36*). Borosilicate pipettes (1B150F-4, World Precision Instruments, Sarasota, FL) were pulled to resistances of 10–20 MΩ using a two-stage pipette puller (PP-830, Narishige, East Meadow, NY). Pipette tips were coated with Sylgard (Dow Corning, Midland, MI) and cured using a heat gun. The pipettes were then heat polished using a microforge (MP-830, Narishige). Before recording, transfected cells were washed with Dulbecco's Phosphate Buffered Saline (DPBS) containing (in mM): 137 NaCl, 0.9 $CaCl_2$, 0.5 $MgCl_2$, 2.7 KCl, 1.5 KH_2PO_4, 8.1 Na_2PO_4, pH 7.3. The bath solution was DPBS. Pipette solutions were DPBS supplemented with agonist. Pipettes tips were backfilled with the pipette solution, filling 1–2 mm linear volume, using a MicroFil syringe (World Precision Instruments). For each compound tested, a new syringe was used. Cell membrane potentials were typically -30 to -40 mV, and a command voltage of -70 mV was used during recording. Single-channel currents were amplified with an Axopatch 200B patch-clamp amplifier (Axon Instruments, Foster City, CA) and recorded through a low-pass Bessel filter at 10 kHz. Data was digitized at a sampling rate of 20 kHz using a NI 6040 E Data Acquisition Board (National Instruments, Austin, TX). Data was recorded using QuB software (www.qub.buffalo.edu) (*37-41*).

Identifying Single-Channel Clusters.

At high agonist concentrations, single-channel events have a characteristic clustered appearance. Most channels are desensitized, resulting in the long closed sojourns between clusters. If only one open conductance level is observed in the cluster, the clusters themselves likely represent activity from one channel. As the "intracluster" open probability increases, the probability that the cluster represents activity from exactly one channel becomes very high. Therefore, analysis of intracluster events permits estimation of microscopic rate constants without the problem of ensemble averaging. The data presented in this study are derived from intracluster events and the durations, or dwells, of these events.

The baselines of single-channel records were adjusted manually using QuB. A 5 kHz Gaussian digital filter was applied, and records were idealized using either the segmental k-

means or half-amplitude algorithms in QuB (*37*). All records were examined visually in their entirety, and misidealizations were corrected manually.

To identify clusters, the desensitized and non-desensitized closed dwells are classified and separated by analyzing exponential time constants that describe the close dwell-time distribution. There are several non-desensitized and desensitized closed states, and the lifetime of each of these states is exponentially distributed. Each state contributes an exponential time component, or time constant, to the observed closed dwell-time distribution. For each idealized dwell-time record, these time constants and their fractional contribution to the distribution, or amplitude, were determined in QuB using a maximum-interval likelihood (MIL) algorithm (*38*). MIL fitting in QuB requires the use of a kinetic model. The fitted time constants depend on the number of states included in the model but not the topology of the model. Thus, an arbitrary, uncoupled star model was used to obtain time constants, ignoring the fitted rate constants (*42*). Closed and open states were added successively until the negative log-likelihood score increased by less than the ln(N)/2, the Schwarz threshold for nested model selection for N events (*42, 43*). This procedure results in a set of time constants and associated fractional amplitudes, (τ_i, a_i), that describe the observed closed dwell-time distribution

By inspecting the closed dwell-time distribution and time constants determined above, a critical time, t_{crit}, was chosen to separate non-desensitized dwells and desensitized dwells. Typically, non-desensitized closed dwells make the largest contribution to the distribution at shorter times. In contrast, desensitized dwells contributed longer closed dwells. To choose a t_{crit}, the closed-dwell time was visually inspected, and an initial cutoff was subjectively chosen to separate non-desensitized and desensitized components. The non-desensitized components (τ_i, a_i) are shorter than the cutoff, and the desensitized components (τ_j, a_j) are longer than the cutoff. The critical time was chosen to minimize the percentage of misclassified events by solving **Equation II.1**, and the fraction of misclassified events, κ, is given by **Equation II.2**. An example is given in **Figure II.2**. The fraction of misclassified events was typically less than 5%.

$$\sum_{i=1}^{m} \frac{a_i}{\tau_i} \cdot e^{-t_{crit}\,\tau_i} = \sum_{j=m+1}^{n} \frac{a_j}{\tau_j} \cdot e^{-t_{crit}\,\tau_j} \qquad (II.1)$$

$$\kappa = \sum_{i=1}^{m} a_i \cdot e^{-t_{crit}\,\tau_i} + \sum_{j=m+1}^{n} a_j \cdot (1 - e^{-t_{crit}\,\tau_j}) \qquad (II.2)$$

Once the t_{crit} is determined, clusters were defined as successive open and closed events separated by closed dwells of length greater than the t_{crit}. Clusters with fewer than five events and multiple-conductance levels (more than one channel) were excluded. Clusters were visually examined to ensure t_{crit} was properly chosen.

Single-Channel Analysis of Intracluster Closed and Open Events

The intracluster closed and open dwell-time distributions were analyzed in QuB to estimate the diliganded closing rate constant α_2, the diliganded opening rate constant β_2, and the diliganded gating equilibrium constant $\Theta_2 = \beta_2/\alpha_2$. Clustered activity was observed for TMA and ETMA at concentrations from 10 μM to 5 mM. Clustered activity was observed for DEDMA at concentrations from 50 μM to 5 mM. At 10 μM DEDMA, activity from low-channel count patches appeared to exhibit very long, low open probability (P_o) clusters. Because loose clusters such as this may include interlaced activity of more than one channel, the observed open probability is between P_o and $N \cdot P_o$ where N is the number of channels in the patch. Analysis of these clusters is still useful for obtaining upper bounds for P_o and β_2. Estimation of α_2 is not affected by this complication. Clusters were only observed for TEMA at 1 mM, but as with DEDMA estimates from lower concentrations still provided upper bounds for P_o and β_2. At 5 mM TEMA, currents were too low in amplitude due to fast block, and were not analyzed further. The analysis and estimation of diliganded rate constants is explained in detail in the **Results** section.

Intracluster open probabilities were analyzed according to the equivalent binding sites model shown in **Scheme II.1**. In the equivalent binding sites scheme, agonist binding to each transmitter binding sites is identical. The agonist closed-state dissociation constant is K_D. The diliganded gating equilibrium constant is Θ_2. The blocking dissociation rate constant is K_B. The gap equilibrium constant is K_G. The gap state empirically compensates for the contamination of clusters by desensitized sojourns, and it adjusts for the maximum open probability observed for each agonist (*24*). The gap state is accessible from both the unblocked and blocked open state. The resting and desensitization gates have been shown to be distinct entities (*44, 45*), and it has also been shown that the desensitization gate can close while the open pore is blocked (*46*).

The equivalent binding sites model is often a good descriptor of single-channel activity when differentiating binding sites is not essential (*24*). However, the two muscle-type AChR binding sites are not equivalent (*25*) as discussed in more detail in **Chapter III**. In this work, we are interested in comparing binding energy versus diliganded gating energy, so the equivalent binding sites model is an appropriate and useful simplification.

Computations.

Ab initio calculations were carried using the Gaussian 03 program package (*47*). Geometry optimization and Hartree-Fock energies were calculated in the gas phase using the 6-31g(d,p) basis set. Gas phase calculations have proven useful for investigating the trends in a cation-π perturbation series (*14, 15, 18, 48-50*). We examined the binding energy trends between benzene and the cations experimentally investigated in this work. Tryptophan has also been used to investigate possible additional hydrogen bonding with some agonists (*14*). Here, benzene was used as a simple model aromatic (*48-51*). Our interest was to assess cation-π binding energy as a straightforward metric which might correlate with closed-state or open-state affinity. The binding energy was estimated as the difference in energies of benzene and the cation optimized separately versus the energy of the pair optimized in complex. The cation was initially placed 4.5 Å above the benzene ring in at least three different orientations; for example, TMA was placed with one, two, or three methyl groups facing the benzene ring. The conformations of the benzene-cation complexes optimized to approximately the same final conformation in each case, and the mean and standard deviation (SD) of the calculated binding energies were used throughout the work. No constraints were placed on the conformation of the benzene ring or the benzene-cation distance. The calculated TMA-benzene interaction energy and conformation agreed with the previously published value using this method and basis set (*48*). As expected, the calculated cation-π energies of the organic cations are smaller than those previously reported for cations such as Na^+ (*49, 50*), but the trends are still apparent.

Non-linear least squares fitting of the dose-response curves and fitting of linear correlations was performed in Origin (OriginLab, Northhampton, MA).

II.D Results

Activation and Block by Simple Organic Cations.

Single-channel currents from the gain-of-function αG153S mutant AChR were measured using TMA (**Figure II.3**), ETMA (**Figure II.4**), DEDMA (**Figure II.5**), TEMA (**Figure II.6**), and TMP (**Figure II.7**) as agonists. TMA was the most efficacious agonist of the ammonium series, and substitution of additional ethyl groups decreased activity. The P_o versus concentration dose-response curve was initially fitted to a Hill equation (**Equation II.3**), where EC_{50} is the concentration for half-maximal open probability and n is the Hill coefficient. The EC_{50} and Hill coefficients are reported in **Table II.1**.

$$P_O = P_O^{Max} \cdot \frac{[Agonist]^n}{EC_{50}^n + [Agonist]^n} \qquad (II.3)$$

Activation by TEMA was weak, and the Hill coefficient was constrained to 1.5 to produce a reliable fit. Hill coefficients consistently have been observed to be 1 to 2 for AChR agonists (*52*). In this range, P_O^{Max} varied from 0.028 to 0.053 with a coefficient of variation of 20% (**Table II.2**), and the standard deviation of this range of values was used to estimate the error in P_O^{Max}.

It is important to measure the magnitude of unresolved open-channel blockade because fast blockade will cause an overestimation of open probabilities. A reduction in open-channel current at high concentrations was observed for all compounds, indicative of unresolved fast open-channel blockade. (**Figure II.8A**) Cationic agonists can also block the open-channel by binding the open pore and interrupting current flow (*53*). When blockade kinetics are sufficiently fast, the interruptions of current are unresolved because of limited recording bandwidth. This phenomenon causes a decrease in the observed open-channel current. The apparent current amplitude in the presence of unresolved open-channel block is a function of the maximal current in the absence of blocker, i_0, and the blocking dissociation constant, K_B (*54*). (**Equation II.4**)

$$i = i_0 \cdot \frac{K_B}{K_B + [Blocker]} \qquad (II.4)$$

The measured K_B values for the various agonists are reported in **Table II.1**. As expected, increasing the number of number of ethyl substitutions increases blocking affinity (*53*).

Contamination of clusters by desensitized sojourns is important to identify because it causes underestimation of the open probability. In most of the high open-probability clusters, regardless of agonist, a gap state is observed to contaminate clusters. The gap state encompasses short-lived desensitized states that has a lifetime on the order of 1 to 10 ms (*24*). Because of the similarity of the gap lifetime to the critical times used for cluster identification, there is inevitably some contamination of gap sojourns in clusters. The gap state is easily dealt with by incorporating it into any model used for analysis (*24*).

Estimation of Diliganded Gating Rate Constants

The diliganded opening rate constant, β_2, can be measured from the dose-response relationship of the intracluster closed times. The effective opening rate, an apparent rate constant incorporating gating and agonist binding rates, is inversely proportional to the major intracluster closed time component which scales with agonist concentration (*55*). As the agonist concentration increases, the receptor is increasingly saturated so that the effective opening rate, β_2', approaches the true opening rate β_2 (*55*). This method provides accurate results even in the presence of gap state contamination for two reasons. One reason for the robustness of the β_2 measurement is that the gap state closed time component is typically small in fractional amplitude. A second reason is that the non-desensitized components are agonist-concentration dependent, but the gap state component is not. A Hill equation can be used to describe the dose response (**Equation II.5**).

$$\beta' = \beta \cdot \frac{[Agonist]^n}{K_{Apparent}^n + [Agonist]^n} \qquad (II.5)$$

Estimation of β_2 in this manner does not require assumption of a model. It is an empirical fit that has been used extensively in studies of the AChR to provide accurate estimates of β_2 (*24, 56*). The αG153S mutant primarily increases agonist affinity, and we expect the diliganded opening rate to be similar to the wild-type rate. As expected, the opening rate constant for TMA for both

the wild-type and mutant is approximately 10000 s^{-1} (*30*). The dose-response of the effective opening rates are shown in **Figure II.8B**, and values are reported in **Table II.3**.

For ETMA, the unconstrained fit converged to values of $\beta_2 = 3400 \pm 200\ s^{-1}$ and a Hill coefficient of n = 5.7. The Hill coefficient fell far outside the expected range of 1 to 2 for AChR agonists (*52*). Constraining the Hill coefficient to 1.5 produced a good fit, and the opening rate constant was $\beta_2 = 3500 \pm 200\ s^{-1}$. We tested the sensitivity of the estimate of β_2 to variation in n, and it varied from $3800 \pm 400\ s^{-1}$ (n=1) to $3500 \pm 200\ s^{-1}$ (n=2) with a coefficient of variation of 3%. Therefore, the estimate of β_2 is insensitive to n and is robust and reliable.

Because activation by TEMA is weak, the Hill coefficient was constrained to produce a reliable fit. When the Hill coefficient was constrained to n = 1.5, the opening rate constant was estimated to be $\beta_2 = 60\ s^{-1}$. The opening rate constant was fairly sensitive to n. For the range of n from 1.0 to 2.0, the coefficient of variation for β_2 estimates was 52%. 30% of this variation was due to the estimates of β_2 when n was constrained to 1.0 or 1.1, and the estimates of β_2 when n was constrained to 1.2–2.0 accounted for the remaining 22% variation (**Table II.2**). The standard deviation of these range of opening rate constant values was used to estimate the error; hence, we estimated that $\beta_2 = 60 \pm 40\ s^{-1}$ for activation of the αG153S AChR by TEMA.

The diliganded closing rate constant α_2 can be estimated from the mean length of single-channel openings. Open lifetimes were observed to increase with agonist concentration (**Figure II.8C**). This observation is consistent with fast, unresolved open-channel block described above. The increase in mean open lifetime, $\langle t_O \rangle$, is linearly related to concentration (**Equation II.6**). The y-intercept estimates the unblocked open lifetime which is inversely proportional to the diliganded closing rate constant α_2.

$$\langle t_O \rangle = \frac{1}{\alpha_2} + \frac{1}{\alpha_2} \cdot \frac{[Blocker]}{K_B} \qquad (II.6)$$

Measured values for α_2 are reported in **Table II.3**, and we calculate the gating equilibrium constant $\Theta_2 = \beta_2 / \alpha_2$.

Diliganded Gating Φ-Value

The diliganded gating rate constants and equilibria were measured in a model-independent manner, and the slope, Φ, of the linear rate-equilibrium free energy relationship (REFER) is consistent with previously measured values (*33, 34*) (**Figure II.9**). For the AChR allosteric gating mechanism, the Φ-value is a measure of transition state structure and relative timing in the conformational reaction (*57*). To measure Φ, perturbations are applied to the AChR at a specific location, such as a series of mutations at a single residue or a series of agonists at the transmitter binding site. For the series, the diliganded opening rate constant β_2 is plotted as a function of the gating equilibrium Θ_2 on a log-log scale. The Φ-value is the slope of the linear REFER. A Φ-value close to 1 indicates the change in gating equilibrium is due mostly to a change in β_2. For the transmitter binding sites, $\Phi \sim 0.9$ has been measured (*33, 34*). For the agonists examined here, $\Phi = 0.84 \pm 0.01$ ($R^2 = 0.9992$) was observed. We conclude that in our system, the mutant TBSs exhibit characteristics consistent with wild-type TBSs.

Estimation of K_D From the P_o Dose-Response Curve

The closed state affinities, K_D, were estimated by fitting **Equation II.8** to the intracluster open probability dose-response relationships, using measured values of K_B and Θ_2 (**Figure II.8D, Table II.3**). A simple equivalent binding sites models was used to fit the dose-response relationships because basic discrimination between total closed-state binding affinity and gating efficiency was the goal (*24*). Given **Scheme II.1**, the intracluster open probability equals the total steady-state occupancy of all open states within the cluster (**Equation II.8**). A is the agonist concentration, and K_G is the equilibrium constant for gap state contaminating sojourns. Fast open-channel block is unresolved in these experiments, causing lengthening of open lifetimes. Therefore, it is appropriate to treat unresolved block as an open state, and it appears as the second term of the numerator in **Equation II.8**.

$$P_O = \frac{\left(\frac{A^2}{K_D^2}\cdot\Theta_2\right)+\left(\frac{A^2}{K_D^2}\cdot\Theta_2\cdot\frac{A}{K_B}\right)}{1+\left(\frac{2\cdot A}{K_D}\right)+\left(\frac{A^2}{K_D^2}\right)+\left(\frac{A^2}{K_D^2}\cdot\Theta_2\right)+\left(\frac{A^2}{K_D^2}\cdot\Theta_2\cdot\frac{A}{K_B}\right)+\left(\frac{A^2}{K_D^2}\cdot\Theta_2\cdot K_G\right)+\left(\frac{A^2}{K_D^2}\cdot\Theta_2\cdot\frac{A}{K_B}\cdot K_G\right)}$$

$$= \frac{A^2\cdot\Theta_2\cdot K_B + A^3\cdot\Theta_2}{K_D^2\cdot K_B + 2\cdot A\cdot K_D\cdot K_B + A^2\cdot K_B + A^2\cdot\Theta_2\cdot K_B + A^3\cdot\Theta_2 + A^2\cdot\Theta_2\cdot K_G\cdot K_B + A^3\cdot\Theta_2\cdot K_G} \quad (II.8)$$

We take the approach of using model-independent measurements obtained above to constrain this model-dependent analyses, an approach often used to produce physically relevant fitted solutions (*24, 25, 52, 56*). K_B was constrained using the model-independent measurements of fast open-channel block obtained above. This constraint prevents over-parameterization and prevents optimization of K_B to a value inconsistent with the observed data. We also constrained Θ_2 because we obtained model-independent measurements of Θ_2 which reflects the observed activity.

TEMA is a weak agonist, and an additional constraint was placed on K_G to obtain an estimate of K_D for TEMA. K_G can be estimated according to **Equation II.9**, so that the fitted curve saturates at the observed P_O^{Max}. From our estimate of P_O^{Max} for TEMA, K_G was constrained to 30, and fitting produced an estimate of K_D = 200 μM for TEMA.

$$P_O^{Max} = \lim P_O = \frac{1}{1+K_G} \qquad (II.9)$$

Because we obtained estimates of P_O^{Max} and Θ_2 for TEMA by constraining the Hill coefficient to n = 1.5, we examined the sensitivity of K_D estimation to the values of P_O^{Max} and K_G. Sensitivity analysis of P_O^{Max} and Θ_2 produced a range of 11 values for each parameter. We estimated K_D for the 121 possible combinations, and the standard deviation of these 121 values was used to estimate the error in the dissociation constant for TEMA. Therefore we estimate $K_D = 200 \pm 200$ μM.

Calculation of Cation-Pi Interaction Energies

Ab initio calculations of benzene-cation complexes were carried out using the Gaussian 03 program. Geometries were optimized and Hartree-Fock energies were calculated in the gas phase, using the 6-31g(d,p) basis set. The calculated conformations are shown in **Figure II.10** and energies are reported in **Table II.4**. For reference, the conformation of the benzene-TMA complex was manually docked in the epibatidine-bound AChBP structure (**Figure II.11**), and benzene was overlaid with αTrp149.

The cation-pi energies calculated for TMA, ETMA, DEDMA, and TMP were similar. The calculated energy for TEMA was lower. We also carried out calculations for tetraethylammonium (TEA). We did not perform single-channel recordings on TEA because its activity was too low, but it has previously been studied (*31*). The distance between the cation heteroatom and the benzene ring ranged from 4.8 to 5.0 Å, in agreement with other calculations for quaternary ammoniums (*48, 51*). For all optimized complexes, three α carbons are oriented with protons facing the benzene π system in a facial conformation, as has been previously observed (*48*).

Both gating energy and closed-state binding affinity show positive correlation with the calculated cation-pi binding energy, but the closed-state binding affinity is more weakly correlated (**Figure II.12**).

II.E Discussion

Calculated Cation-Pi Energy Strongly Correlates with Gating Energy

The calculated cation-π binding energies are linearly correlated with the diliganded gating energies for simple organic cations (**Figure II.13**). Single-channel recording allowed us to experimentally measure the diliganded rate constants α_2 and β_2 for TMA, ETMA, DEDMA, TEMA, and TMP. The diliganded gating equilibrium, Θ_2, was calculated from these microscopic rate constants. There is a clear linear correlation between cation-π energy and the diliganded gating energy, $-R \cdot T \cdot \ln(\Theta_2)$. A slope of $m_\Theta = 3.1 \pm 0.6$ ($R^2 = 0.87$) was measured.

It can be useful to consider this correlation partitioned between gating rate constants because changing the cation-π binding energy acts as an energetic perturbation to the binding sites. We observe that $m_{\beta 2} > m_{\alpha 2}$ as expected because we have already determined from the Φ-value that a perturbation to the binding site affects the opening rates constant more than the closing rate constant. The gating rate constants are plotted as energies, $+R \cdot T \cdot \ln(\alpha_2)$ and $-R \cdot T \cdot \ln(\beta_2)$, to be consistent with plots of gating and binding energies. For the closing rate constant, the slope is $m_{\alpha 2} = 0.5 \pm 0.1$ ($R^2 = 0.86$), and for the opening rate constant, the slope is $m_{\beta 2} = 2.6 \pm 0.5$ ($R^2 = 0.87$).

Unexpectedly, $m_{\beta 2} > 1$ which suggests either the calculated cation-π binding energy underestimates the strength of the interaction in the AChR binding site or multiple cation-π

interactions are important to open-state affinity. We used a simple model system to perform an ab initio calculations of cation-π binding energies between the cations and benzene. In reality, the aromatic cage of the AChR TBSs contains both tyrosine and tryptophan residues. The cation-π binding ability of benzene and phenol have been calculated to be nearly equal, but an indole has significantly greater cation-π binding potential (*49, 50*). Thus, if the cations are primarily interacting with the indoles of tryptophan residues, our calculations may underestimate the true cation-π binding energy causing a slope greater than unity. It is also reasonable to expect that the cation can form cation-π interactions with the multiple aromatic residues when the aromatic cage is compactly arranged in the open state. Although previous studies using unnatural amino acids suggested that the aromatic cage residues other than αTrp149 do not make cation-π interactions with acetylcholine in the muscle-type AChR (*15, 58*), other studies have shown that different agonist can bind in with different favorable contacts (*7, 8, 14, 18, 29*). Of note, residues αTyr190 and αTyr198 appear to be in significantly greater contact with the agonist molecule in bound AChBP structures (*7, 8*). NMR studies also suggest that the cationic head of acetylcholine comes within 3.9 Å of all five aromatic cage residues when bound to the AChR (*59*). It is possible that multiple cation-π interactions of varying strengths are present in the agonist-bound open-state TBS consistent with an observed slope of greater than unity.

Calculated Cation-Pi Energy Weakly Correlates with Close-State Affinity

The calculated cation-π binding energies are also correlated with the closed-state affinity, but more weakly than with diliganded gating energy (**Figure II.14**). Closed-state affinities were estimated by fitting the intracluster open probability dose-response relationships, using **Scheme II.1**. Both K_B and Θ_2 were constrained during fitting because model-independent measurements were made for these parameters. When the binding energies, $+R \cdot T \cdot \ln(K_D)$, are plotted versus the calculated cation-π binding energies, TMP is a clear outlier (**Figure II.14A**). Excluding TMP, the linear correlation has slope $m_K = 0.15 \pm 0.07$ ($R^2 = 0.4986$). The slope m_K is significantly smaller than the slope m_Θ, suggesting that gating is significantly more sensitive to differences in the abilities of simple agonists to form cation-π interactions.

The K_D's for the ammonium series are very similar, but TMP is an outlier. TMP is a monovalent cation of approximately the same molecular size as ETMA or DEDMA, suggesting

that simple electrostatics do not account for TMP's anomalous behavior. The difference in hydrophobicity between TMP and the ammonium compounds may explain the difference in affinities. The hydrophobicity of small drugs is often estimated by the calculated octanol-water partition coefficient, Log P (*60, 61*). TMP is significantly more hydrophobic than the ammonium compounds. The relationship between Log P and closed-state binding energy is approximately linear (*62, 63*), and the slope is $m_{KLogP} = 0.7 \pm 0.1$ kJ/mol ($R^2 = 0.88$) (**Figure II.14B**).

These results suggest that the cation-π binding interactions contribute only weakly to the total closed-state binding affinity of simple organic cations to the AChR. Other factors such as hydrophobicity appear to have a stronger influence. The correlations indicate the calculated cation-π binding energy may not be an informative metric for the closed-state affinity of organic cations to the AChR; however, they do not rule out a role for cation-π interactions in the closed state.

Implications for the AChR Binding and Activation Mechanism

The strong linear correlation between calculated cation-π energy and gating energy suggests that cation-π interactions are important for open-state affinity of organic cations to the AChR TBSs. There is a weak linear correlation between closed-state binding affinities and calculated cation-π energies with a near-zero slope, suggesting other agonist-channel interactions are more important than cation-π interactions in the closed state. Simple organic cations are not positioned for a strong closed-state cation-π interaction by any mechanisms other than partitioning to the binding site and conformational sampling. In contrast, agonist-bound AChBP structures suggest the TBS aromatic cage is arranged compactly around the organic cation in the open state. The increase in favorable contacts between the cation and aromatics improve positioning for cation-π interactions in the open-state.

This mode of binding may differ with other agonists, and the different contributions cation-π energies make to closed-state or open-state affinities for different agonist can be tested. For example, 5-HT and ACh are both more complex than the organic cations investigated here, and cation-π interactions for these strong agonists are hypothesized to contribute primarily to binding rather than channel gating (*14*). For more complex agonists, the structural components

separate from the cationic center may help position the molecule for a cation-π interaction in the closed-state. For example, the backbone carbonyl of αTrp149 has also been shown to impact activation, attributed to hydrogen-bonding interactions (*14*). For 5-HT and ACh, the non-cationic moieties might position the cationic center optimally for a strong cation-π interaction. In this binding mode, the strength of the closed-state interaction is nearly maximal, and the interaction does not strengthen in the open state to a large extent.

Parameters for Quantitative Structure-Activity Relationships

These results suggest that the calculated cation-π binding energy between a charged agonist and an aromatic ring is a useful parameter for structure-activity relationships that distinguish agonists from antagonists. For simple organic cations, we have shown that the cation-π energy is strongly correlated with gating. Thus, similar small molecules that can bind the closed state well, but do not form cation-π interactions are candidates for antagonistic activity. Log P is already a commonly used parameter in structure-activity relationships, and it correlates with closed-state binding affinity. Thus, Log P may be useful for judging the ability of a small molecule to partition to the closed-state binding site.

We briefly investigated whether the reported binding and gating characteristics of TEA are predicted by the observed correlations. Correcting gating and closed-state affinity for the effects of the mutant receptor used in these studies, we found that TEA closed-state affinity and binding energy fit well on the trend lines predicted by Log P and cation-π energy, respectively.

Clearly, cation-π energy will not be a sole predictor of agonistic versus antagonistic activity, but the strong correlations that have been observed suggest it will be an extremely useful metric for predicting binding and gating characteristics.

II.F Conclusions

We show here that cation-π interactions between organic cations and the AChR binding site contribute to the channel gating efficiency. Cation-π interactions have been shown to impact the function of a broad array of ion channels, both ligand-gated and voltage-gated, and enzymes (*64*). The results suggest that calculated cation-π binding energies may be a useful parameter for predicting agonistic versus antagonistic activity of drug candidates.

II.G References

1. Dougherty, D. A. (2008) Cys-loop neuroreceptors: structure to the rescue?, *Chem. Rev. 108*, 1642-1653.
2. Dougherty, D. A. (2008) Physical organic chemistry on the brain. *J. Org. Chem. 73*, 3667-3673.
3. Lee, C. (2003) Conformation, action, and mechanism of action of neuromuscular blocking muscle relaxants. *Pharmacol. Therapeut. 98*, 143-169.
4. Jensen, A. A., Frolund, B., Liljefors, T., and Krogsgaard-Larsen, P. (2005) Neuronal nicotinic acetylcholine receptors: structural revelations, target identifications, and therapeutic inspirations. *J. Med. Chem. 48*, 4705-4745.
5. Unwin, N. (2005) Refined structure of the nicotinic acetylcholine receptor at 4A resolution. *J. Mol. Biol. 346*, 967-989.
6. Brejc, K., van Dijk, W. J., Klaassen, R. V., Schuurmans, M., van Der Oost, J., Smit, A. B., and Sixma, T. K. (2001) Crystal structure of an ACh-binding protein reveals the ligand-binding domain of nicotinic receptors. *Nature 411*, 269-276.
7. Celie, P. H., van Rossum-Fikkert, S. E., van Dijk, W. J., Brejc, K., Smit, A. B., and Sixma, T. K. (2004) Nicotine and carbamylcholine binding to nicotinic acetylcholine receptors as studied in AChBP crystal structures. *Neuron 41*, 907-914.
8. Hansen, S. B., Sulzenbacher, G., Huxford, T., Marchot, P., Taylor, P., and Bourne, Y. (2005) Structures of Aplysia AChBP complexes with nicotinic agonists and antagonists reveal distinctive binding interfaces and conformations. *EMBO J. 24*, 3635-3646.
9. Corringer, P. J., Le Novere, N., and Changeux, J. P. (2000) Nicotinic receptors at the amino acid level. *Ann. Rev. Pharmacol. Toxicol. 40*, 431-458.
10. Karlin, A. (2002) Emerging structure of the nicotinic acetylcholine receptors. *Nat. Rev. Neurosci. 3*, 102-114.
11. Sine, S. M., and Engel, A. G. (2006) Recent advances in Cys-loop receptor structure and function. *Nature 440*, 448-455.
12. Lester, H. A., Dibas, M. I., Dahan, D. S., Leite, J. F., and Dougherty, D. A. (2004) Cys-loop receptors: new twists and turns. *Trends Neurosci. 27*, 329-336.
13. Henchman, R. H., Wang, H. L., Sine, S. M., Taylor, P., and McCammon, J. A. (2003) Asymmetric structural motions of the homomeric alpha7 nicotinic receptor ligand binding domain revealed by molecular dynamics simulation. *Biophys. J. 85*, 3007-3018.
14. Cashin, A. L., Petersson, E. J., Lester, H. A., and Dougherty, D. A. (2005) Using physical chemistry to differentiate nicotinic from cholinergic agonists at the nicotinic acetylcholine receptor. *J. Am. Chem. Soc. 127*, 350-356.
15. Zhong, W., Gallivan, J. P., Zhang, Y., Li, L., Lester, H. A., and Dougherty, D. A. (1998) From ab initio quantum mechanics to molecular neurobiology: a cation-pi binding site in the nicotinic receptor. *Proc. Natl. Acad. Sci. U.S.A. 95*, 12088-12093.
16. Kearney, P. C., Nowak, M. W., Zhong, W., Silverman, S. K., Lester, H. A., and Dougherty, D. A. (1996) Dose-response relations for unnatural amino acids at the agonist binding site of the nicotinic acetylcholine receptor: tests with novel side chains and with several agonists. *Mol. Pharmacol. 50*, 1401-1412.

17. Nowak, M. W., Gallivan, J. P., Silverman, S. K., Labarca, C. G., Dougherty, D. A., and Lester, H. A. (1998) In vivo incorporation of unnatural amino acids into ion channels in Xenopus oocyte expression system. *Meth. Enzymology 293*, 504-529.
18. Beene, D. L., Brandt, G. S., Zhong, W., Zacharias, N. M., Lester, H. A., and Dougherty, D. A. (2002) Cation-pi interactions in ligand recognition by serotonergic (5-HT3A) and nicotinic acetylcholine receptors: the anomalous binding properties of nicotine. *Biochemistry 41*, 10262-10269.
19. Akk, G. (2001) Aromatics at the murine nicotinic receptor agonist binding site: mutational analysis of the alpha Y93 and alpha W149 residues. *J. Physiol. 535*, 729-740.
20. Akk, G., Zhou, M., and Auerbach, A. (1999) A mutational analysis of the acetylcholine receptor channel transmitter binding site. *Biophys. J. 76*, 207-218.
21. Chen, J., Zhang, Y., Akk, G., Sine, S., and Auerbach, A. (1995) Activation Kinetics of Recombinant Mouse Nicotinic Acetylcholine-Receptors - Mutations of Alpha-Subunit Tyrosine-190 Affect Both Binding and Gating. *Biophys. J. 69*, 849-859.
22. Wang, H. L., Auerbach, A., Bren, N., Ohno, K., Engel, A. G., and Sine, S. M. (1997) Mutation in the M1 domain of the acetylcholine receptor alpha subunit decreases the rate of agonist dissociation. *J. Gen. Physiol. 109*, 757-766.
23. Sine, S. M. (1993) Molecular dissection of subunit interfaces in the acetylcholine receptor: identification of residues that determine curare selectivity. *Proc. Natl. Acad. Sci. U.S.A. 90*, 9436-9440.
24. Salamone, F. N., Zhou, M., and Auerbach, A. (1999) A re-examination of adult mouse nicotinic acetylcholine receptor channel activation kinetics. *J. Physiol. 516*, 315-330.
25. Sine, S. M., Ohno, K., Bouzat, C., Auerbach, A., Milone, M., Pruitt, J. N., and Engel, A. G. (1995) Mutation of the Acetylcholine-Receptor Alpha-Subunit Causes a Slow-Channel Myasthenic Syndrome by Enhancing Agonist Binding-Affinity. *Neuron 15*, 229-239.
26. Grutter, T., de Carvalho, L. P., Le Novere, N., Corringer, P. J., Edelstein, S., and Changeux, J. P. (2003) An H-bond between two residues from different loops of the acetylcholine binding site contributes to the activation mechanism of nicotinic receptors. *EMBO J. 22*, 1990-2003.
27. Lee, W. Y., and Sine, S. M. (2004) Invariant aspartic Acid in muscle nicotinic receptor contributes selectively to the kinetics of agonist binding. *J. Gen. Physiol. 124*, 555-567.
28. Cashin, A. L., Torrice, M. M., McMenimen, K. A., Lester, H. A., and Dougherty, D. A. (2007) Chemical-scale studies on the role of a conserved aspartate in preorganizing the agonist binding site of the nicotinic acetylcholine receptor, *Biochemistry 46*, 630-639.
29. Mu, T. W., Lester, H. A., and Dougherty, D. A. (2003) Different binding orientations for the same agonist at homologous receptors: a lock and key or a simple wedge? *J. Am. Chem. Soc. 125*, 6850-6851.
30. Akk, G., and Auerbach, A. (1996) Inorganic, monovalent cations compete with agonists for the transmitter binding site of nicotinic acetylcholine receptors. *Biophys. J. 70*, 2652-2658.
31. Akk, G., and Steinbach, J. H. (2003) Activation and block of mouse muscle-type nicotinic receptors by tetraethylammonium. *J. Physiol. 551*, 155-168.
32. Zhang, Y., Chen, J., and Auerbach, A. (1995) Activation of recombinant mouse acetylcholine receptors by acetylcholine, carbamylcholine and tetramethylammonium. *J. Physiol. 486*, 189-206.

33. Grosman, C., Zhou, M., and Auerbach, A. (2000) Mapping the conformational wave of acetylcholine receptor channel gating. *Nature 403*, 773-776.
34. Purohit, P., Mitra, A., and Auerbach, A. (2007) A stepwise mechanism for acetylcholine receptor channel gating. *Nature 446*, 930-933.
35. Hamill, O. P., Marty, A., Neher, E., Sakmann, B., and Sigworth, F. J. (1981) Improved patch-clamp techniques for high-resolution current recording from cells and cell-free membrane patches. *Pflug. Arch. 391*, 85-100.
36. Sakmann, B., and Neher, E. (1995) *Single-channel recording*, 2nd ed., Plenum Press, New York.
37. Qin, F. (2004) Restoration of single-channel currents using the segmental k-means method based on hidden Markov modeling. *Biophys. J. 86*, 1488-1501.
38. Qin, F., Auerbach, A., and Sachs, F. (1996) Estimating single-channel kinetic parameters from idealized patch-clamp data containing missed events. *Biophys. J. 70*, 264-280.
39. Qin, F., Auerbach, A., and Sachs, F. (1996) Idealization of single-channel currents using the segmental K-means method. *Biophys. J. 70*,432-432.
40. Qin, F., Auerbach, A., and Sachs, F. (1997) Maximum likelihood estimation of aggregated Markov processes. *Proceedings 264*, 375-383.
41. Qin, F., and Li, L. (2004) Model-based fitting of single-channel dwell-time distributions. *Biophys. J. 87*, 1657-1671.
42. Purohit, Y., and Grosman, C. (2006) Estimating binding affinities of the nicotinic receptor for low-efficacy ligands using mixtures of agonists and two-dimensional concentration-response relationships. *J. Gen. Physiol. 127*, 719-735.
43. Schwarz, G. (1978) Estimating Dimension of a Model. *Ann. Stat. 6*, 461-464.
44. Auerbach, A., and Akk, G. (1998) Desensitization of mouse nicotinic acetylcholine receptor channels. A two-gate mechanism. *J. Gen. Physiol. 112*, 181-197.
45. Wilson, G., and Karlin, A. (2001) Acetylcholine receptor channel structure in the resting, open, and desensitized states probed with the substituted-cysteine-accessibility method. *Proc. Natl. Acad. Sci. U.S.A. 98*, 1241-1248.
46. Purohit, Y., and Grosman, C. (2006) Block of muscle nicotinic receptors by choline suggests that the activation and desensitization gates act as distinct molecular entities. *J. Gen. Physiol. 127*, 703-717.
47. Frisch, M. J. T., G. W.; Schlegel, H. B.; Scuseria, G. E.; Robb, M. A.; Cheeseman, J. R.; Montgomery, Jr., J. A.; Vreven, T.; Kudin, K. N.; Burant, J. C.; Millam, J. M.; Iyengar, S. S.; Tomasi, J.; Barone, V.; Mennucci, B.; Cossi, M.; Scalmani, G.; Rega, N.; Petersson, G. A.; Nakatsuji, H.; Hada, M.; Ehara, M.; Toyota, K.; Fukuda, R.; Hasegawa, J.; Ishida, M.; Nakajima, T.; Honda, Y.; Kitao, O.; Nakai, H.; Klene, M.; Li, X.; Knox, J. E.; Hratchian, H. P.; Cross, J. B.; Bakken, V.; Adamo, C.; Jaramillo, J.; Gomperts, R.; Stratmann, R. E.; Yazyev, O.; Austin, A. J.; Cammi, R.; Pomelli, C.; Ochterski, J. W.; Ayala, P. Y.; Morokuma, K.; Voth, G. A.; Salvador, P.; Dannenberg, J. J.; Zakrzewski, V. G.; Dapprich, S.; Daniels, A. D.; Strain, M. C.; Farkas, O.; Malick, D. K.; Rabuck, A. D.; Raghavachari, K.; Foresman, J. B.; Ortiz, J. V.; Cui, Q.; Baboul, A. G.; Clifford, S.; Cioslowski, J.; Stefanov, B. B.; Liu, G.; Liashenko, A.; Piskorz, P.; Komaromi, I.; Martin, R. L.; Fox, D. J.; Keith, T.; Al-Laham, M. A.; Peng, C. Y.; Nanayakkara, A.; Challacombe, M.; Gill, P. M. W.; Johnson, B.; Chen, W.; Wong, M. W.; Gonzalez, C.; and Pople, J. A. (2004) Gaussian 03, Revision B.05, Gaussian, Inc., Wallingford, CT.

48. Lee, J. Y., Lee, S. J., Choi, H. S., Cho, S. J., Kim, K. S., and Ha, T. K. (1995) Ab-Initio Study of the Complexation of Benzene with Ammonium Cations. *Chem. Phys. Lett. 232*, 67-71.
49. Mecozzi, S., West, A. P., and Dougherty, D. A. (1996) Cation-pi interactions in aromatics of biological and medicinal interest: Electrostatic potential surfaces as a useful qualitative guide. *Proc. Natl. Acad. Sci. U.S.A. 93*, 10566-10571.
50. Mecozzi, S., West, A. P., and Dougherty, D. A. (1996) Cation-pi interactions in simple aromatics: Electrostatics provide a predictive tool. *J. Am. Chem. Soc. 118*, 2307-2308.
51. Gao, J., Chou, L. W., and Auerbach, A. (1993) The Nature of Cation-Pi-Binding - Interactions between Tetramethylammonium Ion and Benzene in Aqueous-Solution. *Biophys. J. 65*, 43-47.
52. Akk, G., and Auerbach, A. (1999) Activation of muscle nicotinic acetylcholine receptor channels by nicotinic and muscarinic agonists. *Brit. J. Pharmacol. 128*, 1467-1476.
53. Carter, A. A., and Oswald, R. E. (1993) Channel Blocking Properties of a Series of Nicotinic Cholinergic Agonists. *Biophys. J. 65*, 840-851.
54. Grosman, C., and Auerbach, A. (2000) Asymmetric and independent contribution of the second transmembrane segment 12 ' residues to diliganded gating of acetylcholine receptor channels - A single-channel study with choline as the agonist. *J. Gen. Physiol. 115*, 637-651.
55. Auerbach, A. (1993) A Statistical-Analysis of Acetylcholine-Receptor Activation in Xenopus Myocytes - Stepwise Versus Concerted Models of Gating. *J. Physiol. 461*, 339-378.
56. Akk, G., and Steinbach, J. H. (2005) Galantamine activates muscle-type nicotinic acetylcholine receptors without binding to the acetylcholine-binding site. *J. Neurosci. 25*, 1992-2001.
57. Auerbach, A. (2007) How to turn the reaction coordinate into time. *J. Gen. Physiol. 130*, 543-546.
58. Nowak, M. W., Kearney, P. C., Sampson, J. R., Saks, M. E., Labarca, C. G., Silverman, S. K., Zhong, W., Thorson, J., Abelson, J. N., Davidson, N., and et al. (1995) Nicotinic receptor binding site probed with unnatural amino acid incorporation in intact cells, *Science 268*, 439-442.
59. Williamson, P. T., Verhoeven, A., Miller, K. W., Meier, B. H., and Watts, A. (2007) The conformation of acetylcholine at its target site in the membrane-embedded nicotinic acetylcholine receptor. *Proc. Natl. Acad. Sci. U.S.A. 104*, 18031-18036.
60. Chou, J. T., and Jurs, P. C. (1979) Computer-Assisted Computation of Partition-Coefficients from Molecular-Structures Using Fragment Constants. *J. Chem. Inf. Comp. Sci. 19*, 172-178.
61. Viswanadhan, V. N., Ghose, A. K., Revankar, G. R., and Robins, R. K. (1989) Atomic Physicochemical Parameters for 3 Dimensional Structure Directed Quantitative Structure - Activity Relationships .4. Additional Parameters for Hydrophobic and Dispersive Interactions and Their Application for an Automated Superposition of Certain Naturally-Occurring Nucleoside Antibiotics. *J. Chem. Inf. Comp. Sci. 29*, 163-172.
62. Plaizier-Vercammen, J. A. (1987) Interaction of povidone with aromatic compounds. VI: Use of partition coefficients (log Kd) to correlate with log P values and apparent Kd values to express the binding as a function of pH and pKa. *J. Pharmaceut. Sci. 76*, 817-820.

63. Brown, M. L., Brown, G. B., and Brouillette, W. J. (1997) Effects of log P and phenyl ring conformation on the binding of 5-phenylhydantoins to the voltage-dependent sodium channel. *J. Med. Chem. 40*, 602-607.
64. Ma, J. C., and Dougherty, D. A. (1997) The Cation-pi Interaction. *Chem. Rev. 97*, 1303-1324.

Table II.1. Hill Parameters for Intracluster Open Probability Agonist Dose Response

Agonist	P_O^{Max}	EC_{50} (μM)	n	K_B (μM)
TMA	0.81 ± 0.03	50 ± 7	1.2 ± 0.1	7000 ± 2000
ETMA	0.66 ± 0.04	80 ± 10	1.7 ± 0.2	2000 ± 100
DEDMA	0.30 ± 0.03	230 ± 60	1.6 ± 0.2	1000 ± 100
TEMA	0.03 ± 0.01	400 ± 200	1.5 *	500 ± 20
TMP	0.77 ± 0.04	310 ± 50	1.6 ± 0.1	2900 ± 300

* For TEMA, *n* was constrained to 1.5 to obtain estimates. The sensitivity of P_O^{Max} to the value of *n* is evaluated in Table II.2, and the error in P_O^{Max} is the standard deviation of values obtained from the sensitivity analysis.

Table II.2. Sensitivity of TEMA Dose-Response Estimates to the Hill Coefficient n

n	P_O^{Max}	EC_{50} (μM)
1	0.05 ± 0.03	1100 ± 900
1.1	0.04 ± 0.02	800 ± 500
1.2	0.04 ± 0.01	600 ± 400
1.3	0.04 ± 0.01	500 ± 300
1.4	0.03 ± 0.01	500 ± 200
1.5*	0.03 ± 0.01*	400 ± 200*
1.6	0.031 ± 0.005	400 ± 100
1.7	0.030 ± 0.004	400 ± 100
1.8	0.030 ± 0.004	400 ± 100
1.9	0.029 ± 0.004	300 ± 00
2	0.028 ± 0.003	330 ± 90
n	**β_2 (s^{-1})**	**EC_{50} (μM)**
1	200 ± 300	3000 ± 9000
1.1	100 ± 100	2000 ± 2000
1.2	80 ± 60	1000 ± 100
1.3	70 ± 40	800 ± 700
1.4	60 ± 30	700 ± 500
1.5*	60 ± 20*	600 ± 400*
1.6	50 ± 10	500 ± 300
1.7	50 ± 10	500 ± 300
1.8	50 ± 10	400 ± 200
1.9	47 ± 8	400 ± 200
2	45 ± 7	400 ± 200

* For TEMA, *n* was constrained to 1.5 to obtain estimates. Standard deviations of the ranges of values obtained in sensitivity analysis were used as the estimated errors for the respective parameters.

Table II.3. Gating and Closed-State Binding Microscopic Rate Constants and Equilibria										
Agonist	**β_2 (s^{-1})**		**α_2 (s^{-1})**		**Θ_2 (s^{-1})**		**K_D (μM)**		**K_{Gap} (Unitless)**	
TMA	10300	± 500	700	± 70	15	± 2	120	± 20	0.24	± 0.05
ETMA	3400	± 200	1030	± 90	3.3	± 0.4	120	± 10	0.33	± 0.09
DEDMA	380	± 30	1400	± 100	0.27	± 0.03	110	± 20	1.4	± 0.4
TEMA	60	± 40[1]	2000	± 100	0.03	± 0.02	200	± 200	30	[2]
TMP	5200	± 100	900	± 40	5.8	± 0.3	530	± 50	0.22	± 0.08

[1] For TEMA, n was constrained to 1.5 to obtain an estimate. The sensitivity of β_2 to the value of *n* is evaluated in Table II.2, and the error in β_2 is the standard deviation of values obtained from the sensitivity analysis.

[2] For TEMA, K_{Gap} was constrained to 30 to obtain and estimate of K_D, and the error in K_D is the standard deviation of values obtained from sensitivity analysis.

Table II.4. Gating and Closed-State Binding Energies[1]										
Agonist	**Cation-π[2]**		**$+R\cdot T\cdot\ln(\alpha_2)$**		**$-R\cdot T\cdot\ln(\beta_2)$**		**$-R\cdot T\cdot\ln(\Theta_2)$**		**$+R\cdot T\cdot\ln(K_D)$**	
TMA	-28.45	± 0.01	16.3	± 0.3	-22.9	± 0.1	-6.7	± 0.3	-22.3	± 0.4
ETMA	-27.19	± 0.19	17.2	± 0.2	-20.1	± 0.2	-2.9	± 0.3	-22.4	± 0.3
DEDMA	-26.28	± 1.80	18.0	± 0.2	-14.7	± 0.2	3.3	± 0.3	-22.7	± 0.3
TEMA	-23.31	± 1.62	18.8	± 0.1	-10	± 2	9	± 2	-21	± 3
TMP	-26.97	± 0.05	16.9	± 0.1	-21.2	± 0.1	-4.4	± 0.1	-18.7	± 0.2

[1] Energies in kJ/mol and uncertainties are propagated uncertainties. R is the gas constant. T = 298.15K.

[2] Cation-π energies are reported as the mean ± SD for three repeated HF6-31g(d,p)// HF6-31g(d,p) geometry optimizations, except for TEA which is the average of two trials.

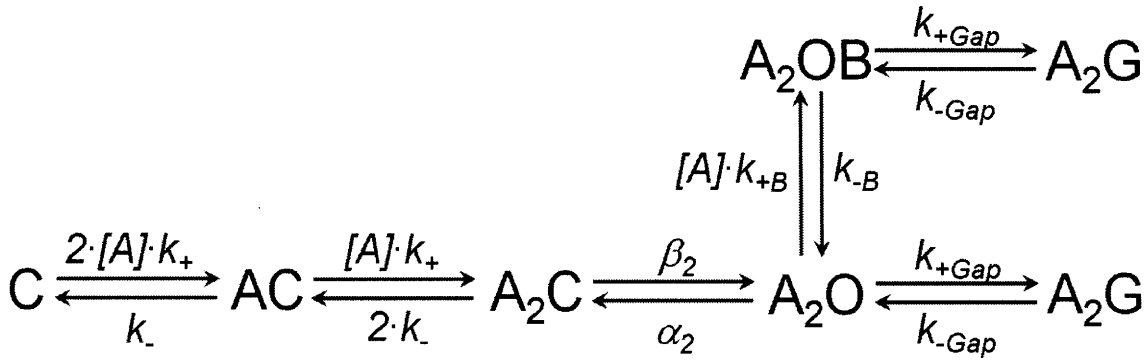

Scheme II.1. An AChR equivalent binding sites model. The closed AChR states are represented by C. The open states are represent by O. The gap states are represented by G. The blocked state is indicated by B. The agonist molecule is denoted A. In the equivalent binding sites scheme, agonist binding to each transmitter binding sites is identical, characterized by the association rate constant k_+ and dissociation rate constant k_-, with dissociation constant $K_D = k_- / k_+$. A statistical factor of 2 is include for the apparent rates of the first binding and unbinding events. The ratio of the diliganded opening rate constant β_2 and closing rate constant α_2 is the gating equilibrium constant Θ_2. The blocking dissociation rate constant is $K_B = k_{-B} / k_{+B}$. The gap equilibrium constant is $K_G = k_{+Gap} / k_{-Gap}$.

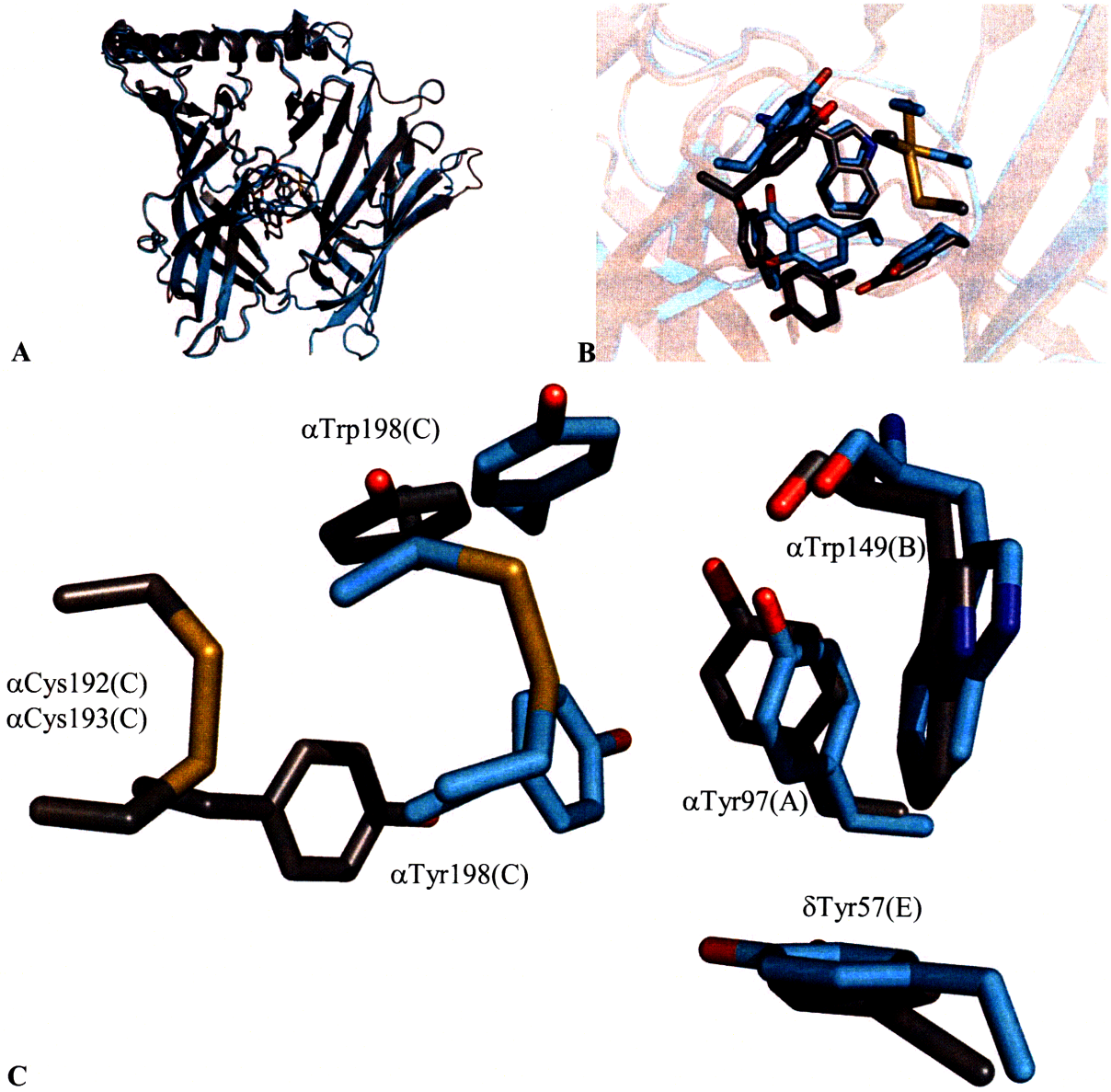

Figure II.1. The aromatic cage in the AChR binding site. (a) An overlay of the apo- (grey) and epibatidine-bound (cyan) AChBP structures (2BYN, 2BYQ). (b) An enlarged view of the aromatic box. (c) Aromatic residues are labels according to the AChR structure. For example, αTrp149(B) indicated the residue equivalent to Trp149 in Loop B of the α-subunit of the muscle-type AChR. Shown for reference, αCys192(C) and αCys193(C) are located at the tip of Loop C. Epibatidine is not shown for clarity.

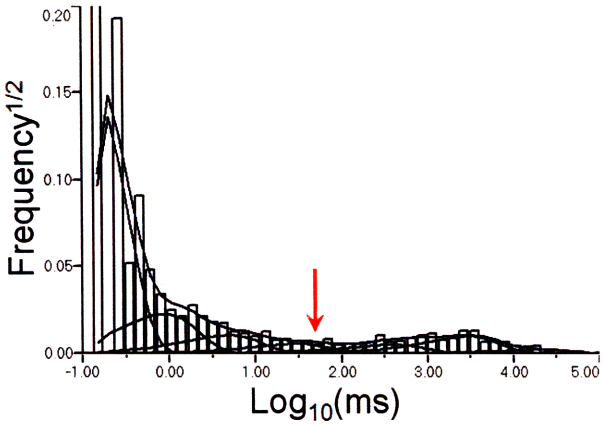

Figure II.2. Choice of t_{crit} for 1 mM TMA. At 1 mM TMA, there is typically a large peak centered at less than 1 ms, representing the bulk of non-desensitized dwells. Desensitized dwells are apparent at greater than 100 ms. For this record, the closed-time distribution was best fit to 7 components: (0.11 ms, 49%); (0.75 ms, 19%); (4.08 ms, 10%); (25.22 ms, 5%); (317.76 ms, 5%); (2461.89 ms, 9%); and (17645.30 ms, 2%). A critical time of approximated 50 ms is calculated (red arrow). Use of this critical time produces clustering that is visually verified (Figure 3). It causes misclassification of 1.7% of events.

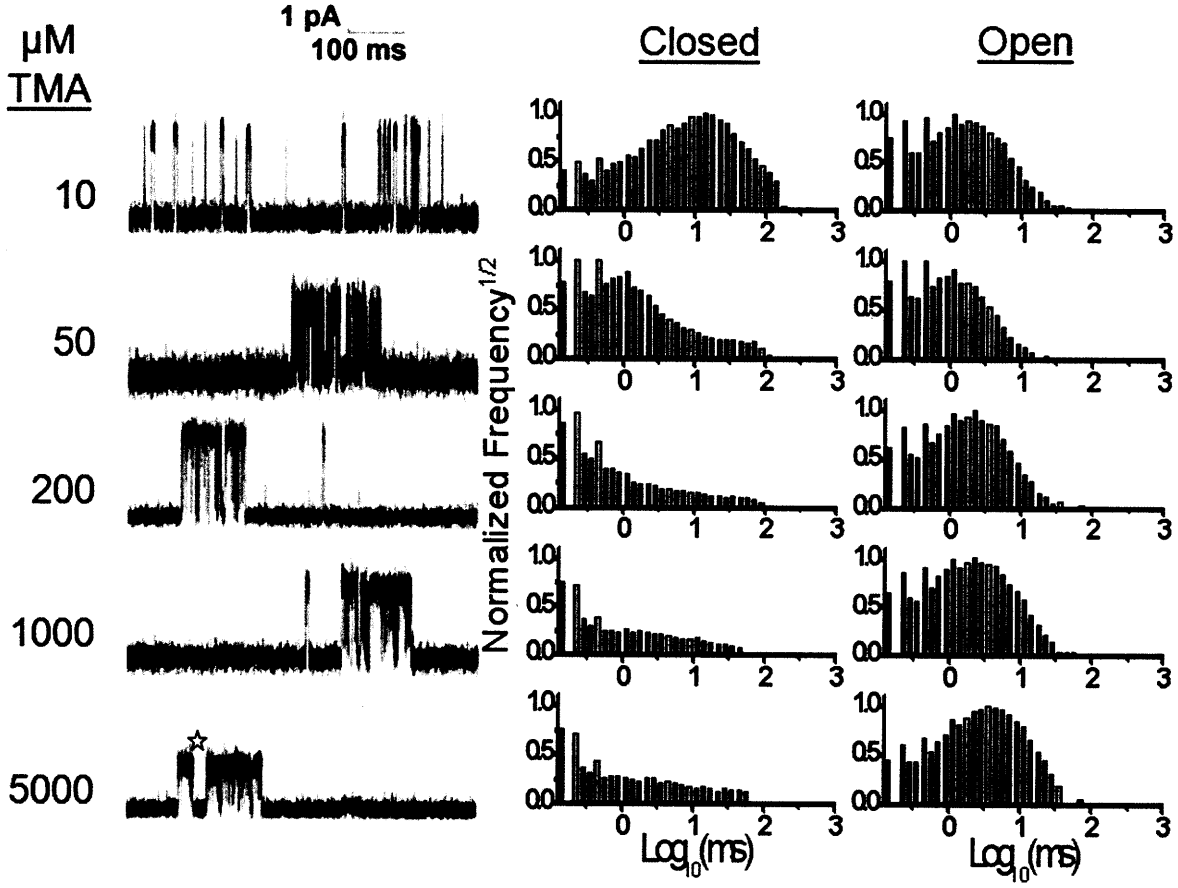

Figure II.3. Single-channel activation of $\alpha^{G153S}{}_2\beta\delta\varepsilon$ AChR receptors by TMA. Examples of single-channel clusters are shown on the left. Openings are upward deflections. An example of a gap sojourn contaminating a high open probability cluster is indicated by the star. The intracluster closed and open dwell-time distributions are shown on the right.

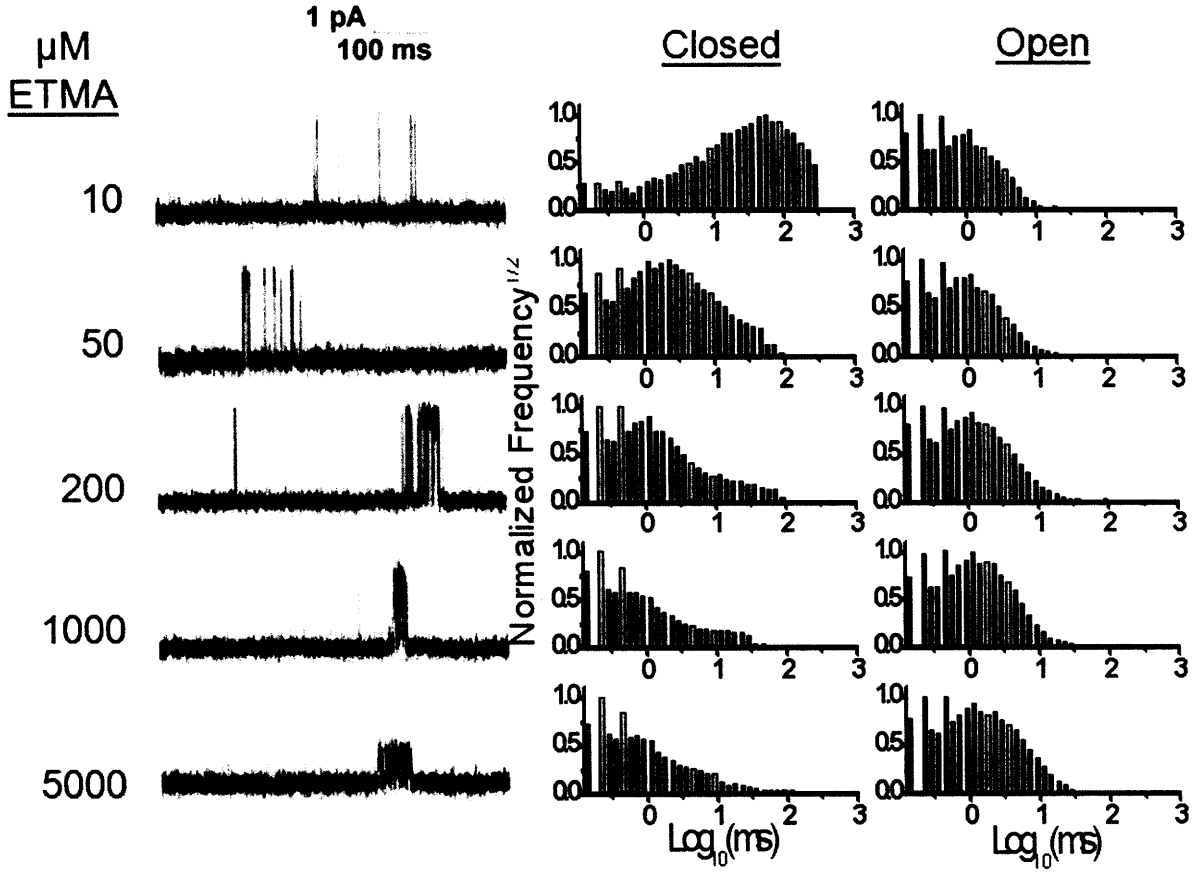

Figure II.4. Single-channel activation of $\alpha^{G153S}{}_2\beta\delta\varepsilon$ AChR receptors by ETMA.

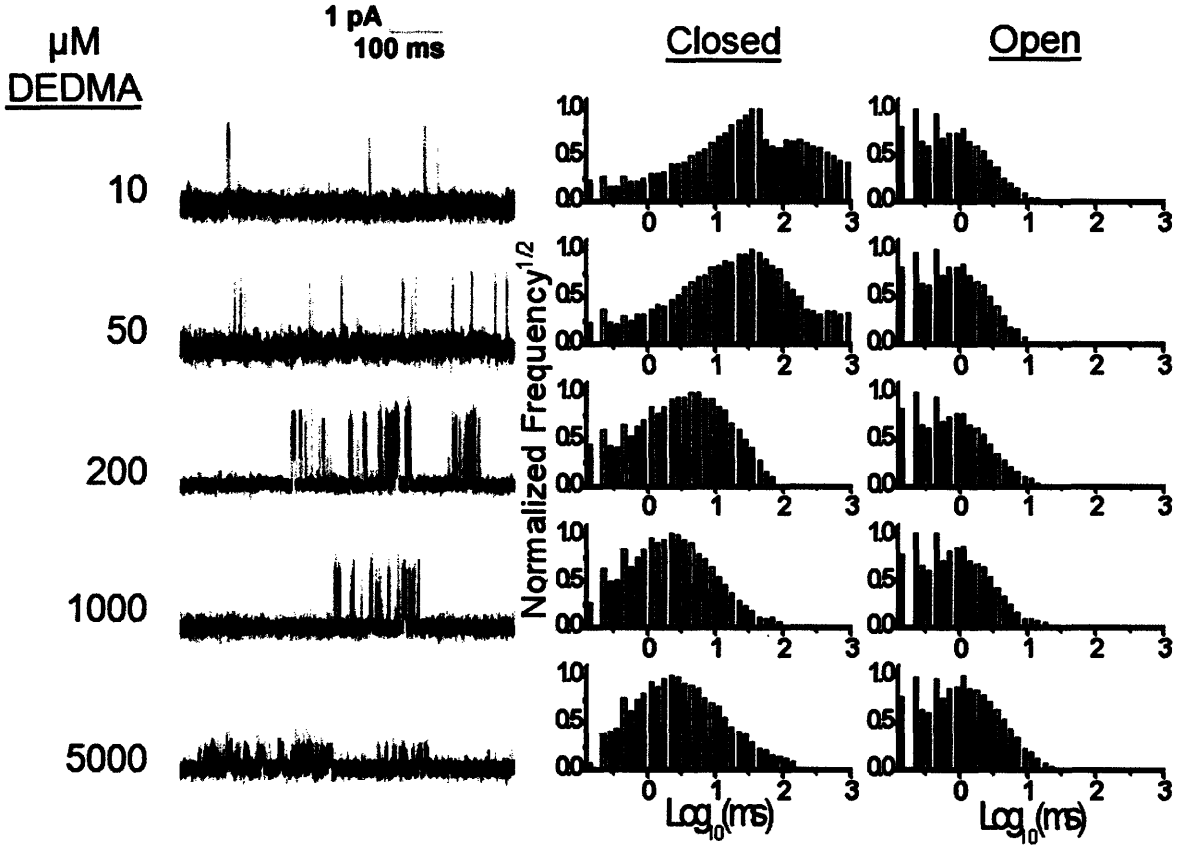

Figure II.5. Single-channel activation of $\alpha^{G153S}{}_2\beta\delta\varepsilon$ AChR receptors by DEDMA.

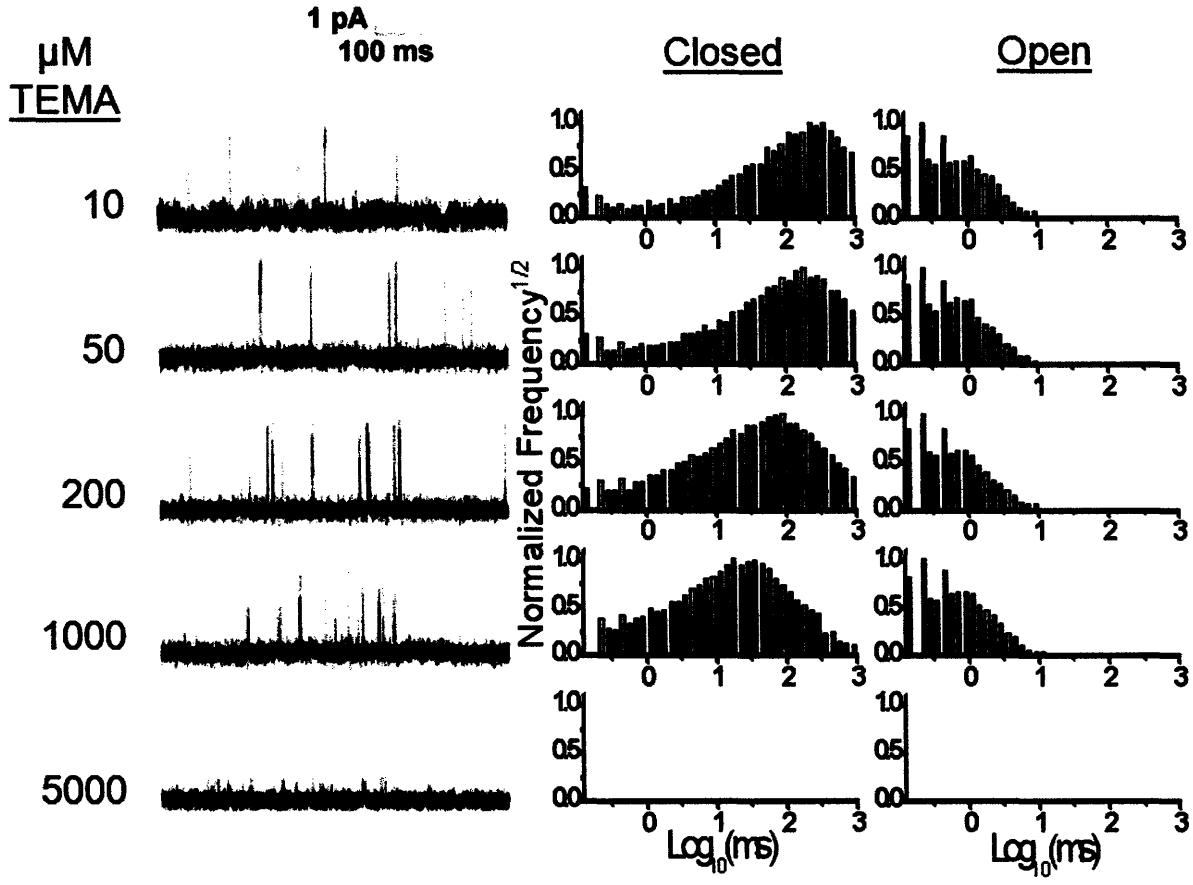

Figure II.6. Single-channel activation of $\alpha^{G153S}{}_2\beta\delta\varepsilon$ AChR receptors by TEMA. Current amplitudes were too low for analysis at 5000 μM TEMA.

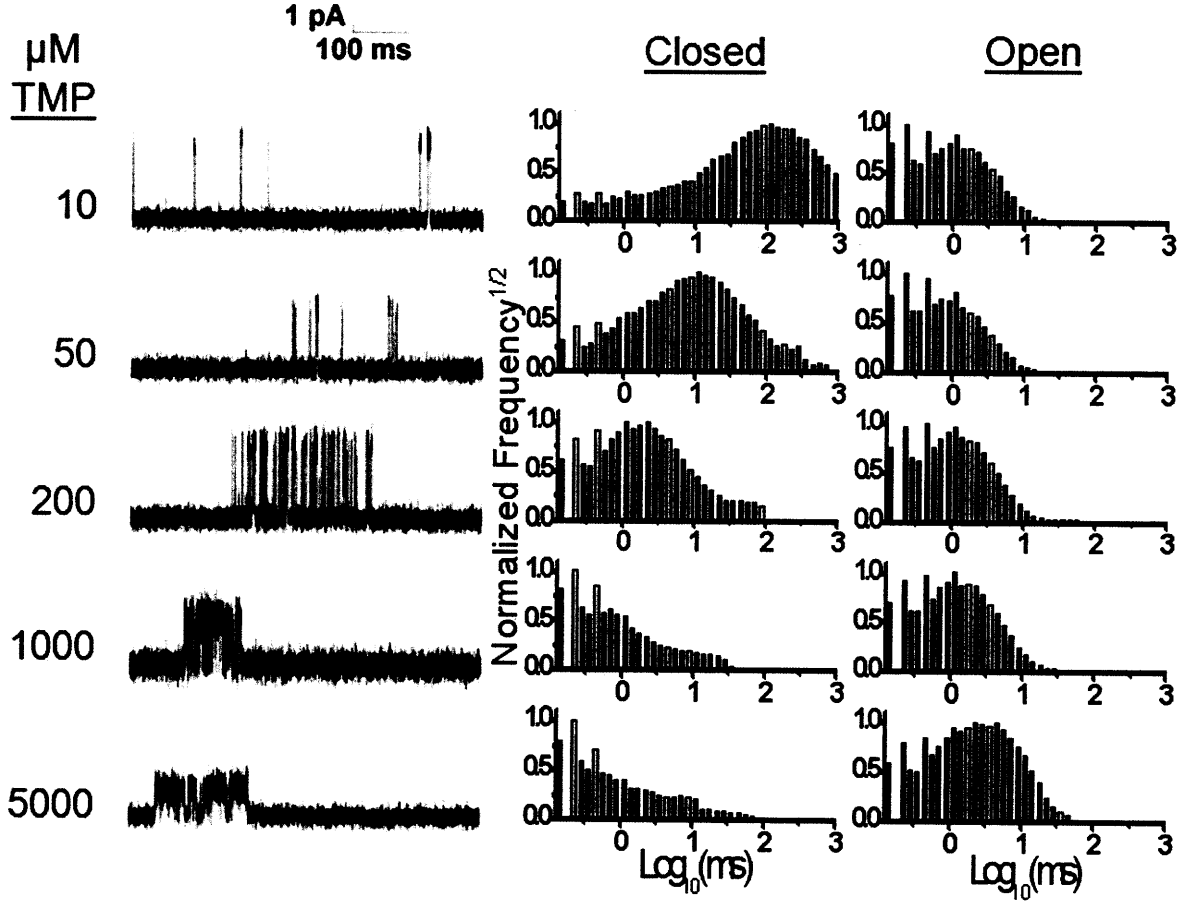

Figure II.7. Single-channel activation of $\alpha^{G153S}{}_2\beta\delta\varepsilon$ AChR receptors by TMP.

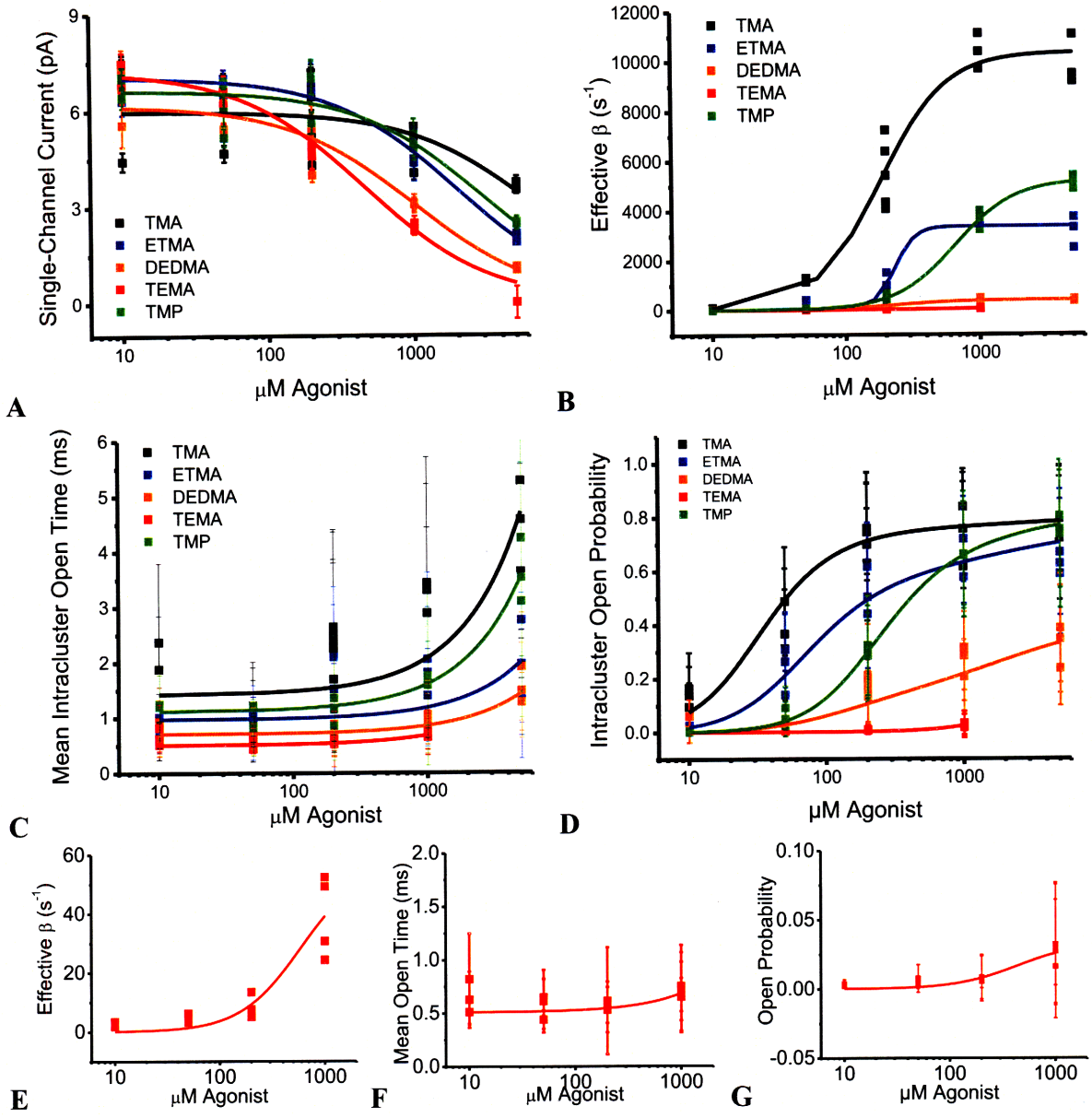

Figure II.8. Analysis of single-channel clusters. (A) Fast, unresolved open-channel block causes a decrease in apparent single-channel current with increasing agonist concentration. (B) The effective opening rate β' approaches the true opening rate β as agonist saturates the receptor. (C) The closing rate is inversely proportional to the unblocked mean open lifetime. (D) Fitting the intracluster open probability using Scheme II.1 provides estimates of the closed-state affinity, K_D. TEMA data are also shown with independent scaling (E–F).

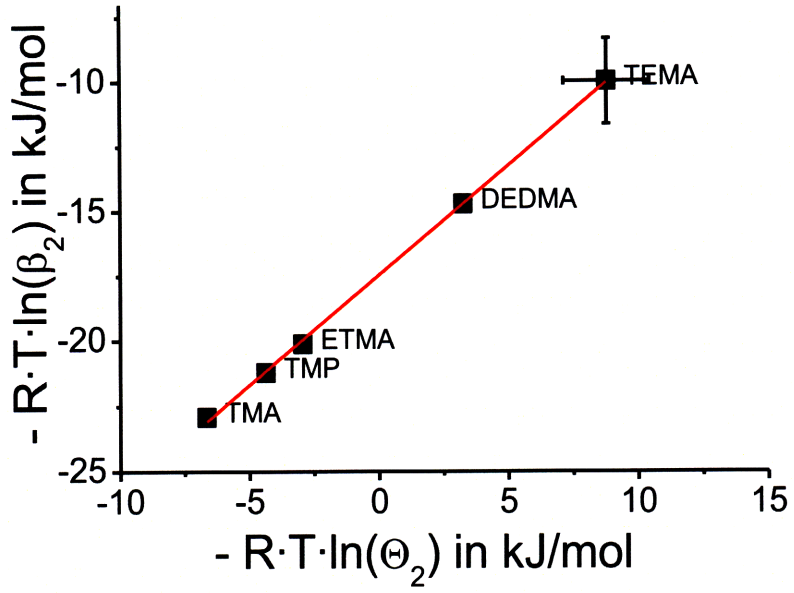

Figure II.9. The rate-equilibrium free energy relationship is linear. The slope is $\Phi = 0.84 \pm 0.01$ ($R^2 = 0.9992$).

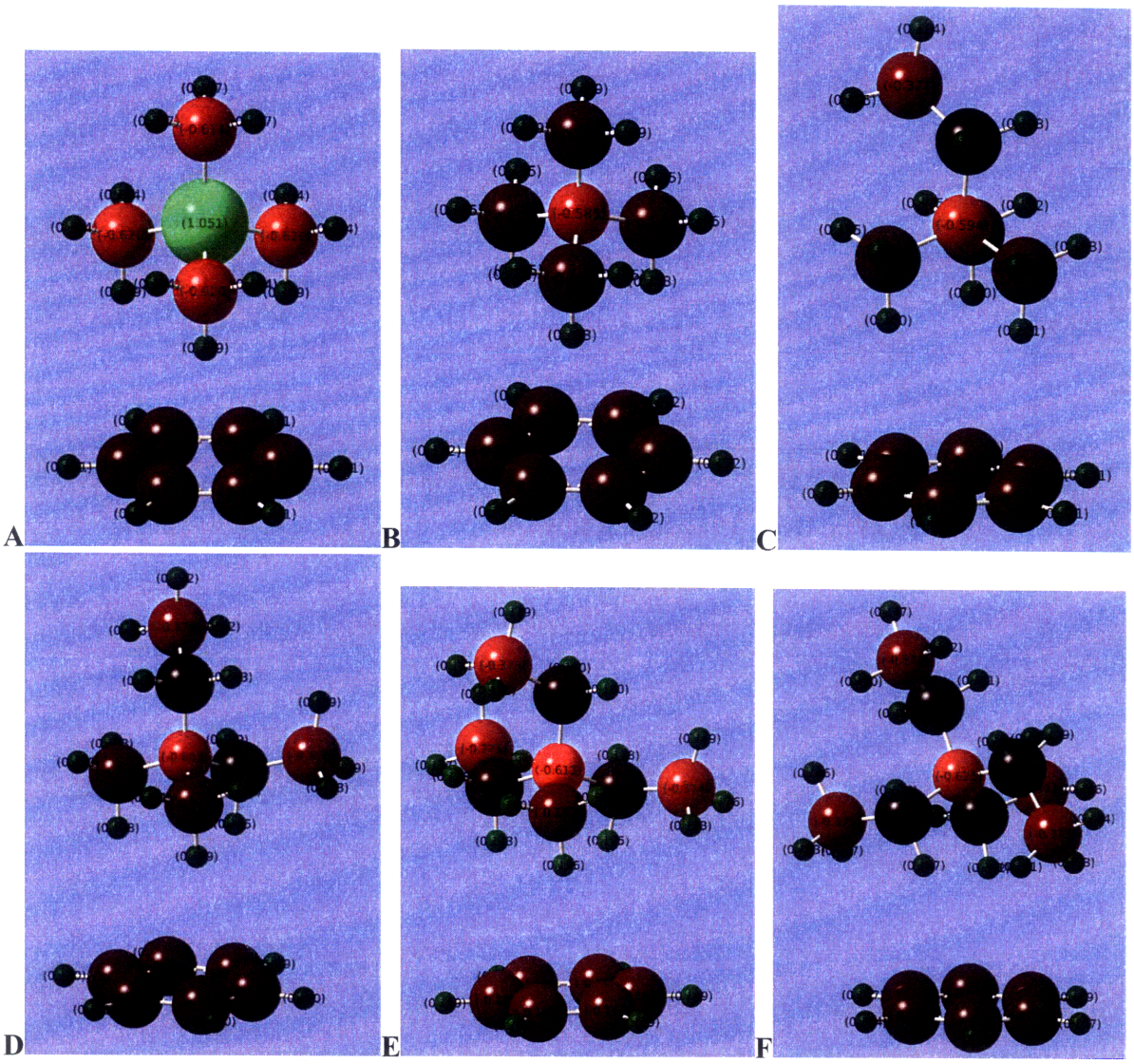

Figure II.10. Energy-optimized conformations produced from HF6-31g(d,p)//HF6-31g(d,p) geometry optimization for benzene in complex with (A) TMP (B) TMA (C) ETMA (D) DEDMA (E) TEMA (F) TEA. Ball and stick representation are shown using van der Waals atomic radii to size spheres. Atoms are colored by charge distribution on a scale of -1 (bright green) to +1 (bright red), with values labeled.

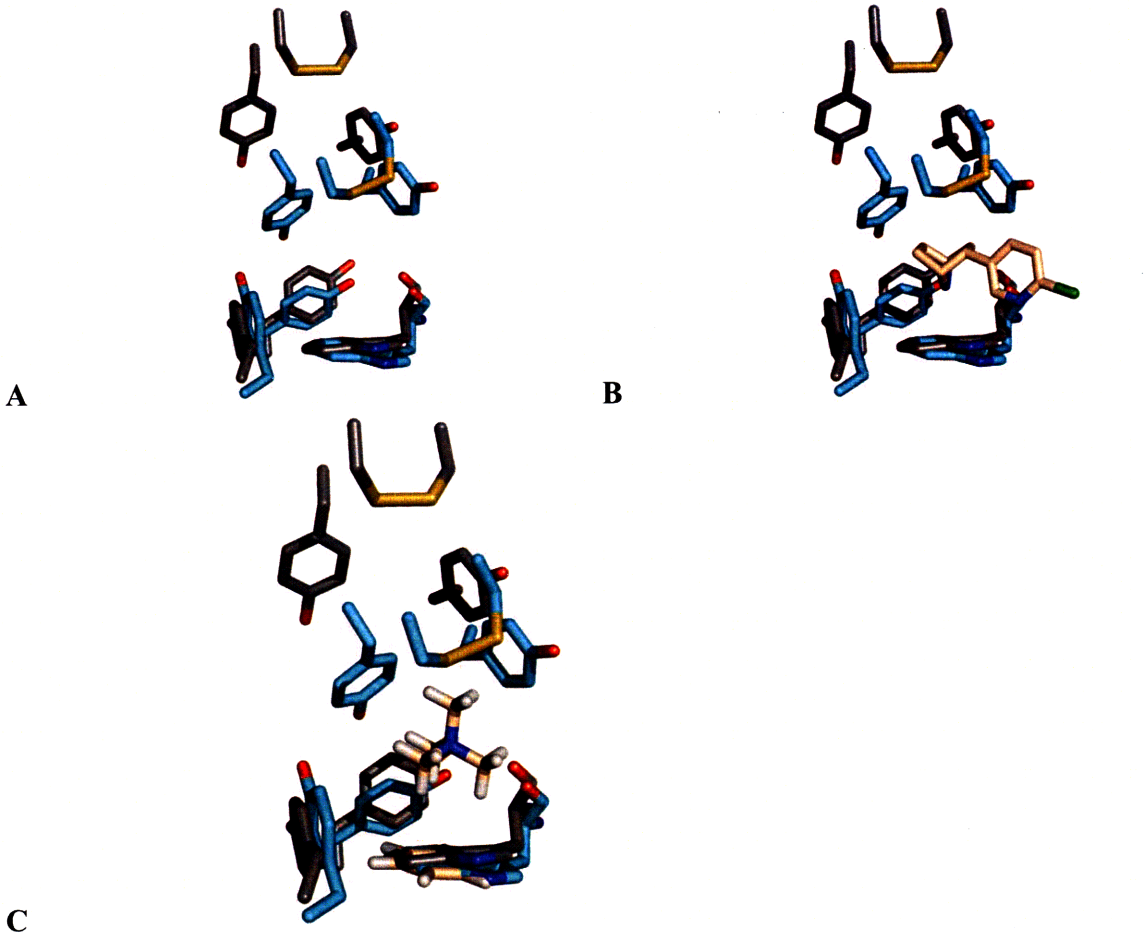

Figure II.11. Overlay of the apo- (grey) and epibatidine-bound (cyan) aromatic box. X-ray structure of the epibatidine-bound AChBP (2BYQ) aromatic box with epibatidine hidden (A) or shown (B). (C) Optimized benzene-TMA complex manually positioned in the aromatic box. The benzene ring was overlaid with the αTrp149. Hydrogens are not shown, except for TMA.

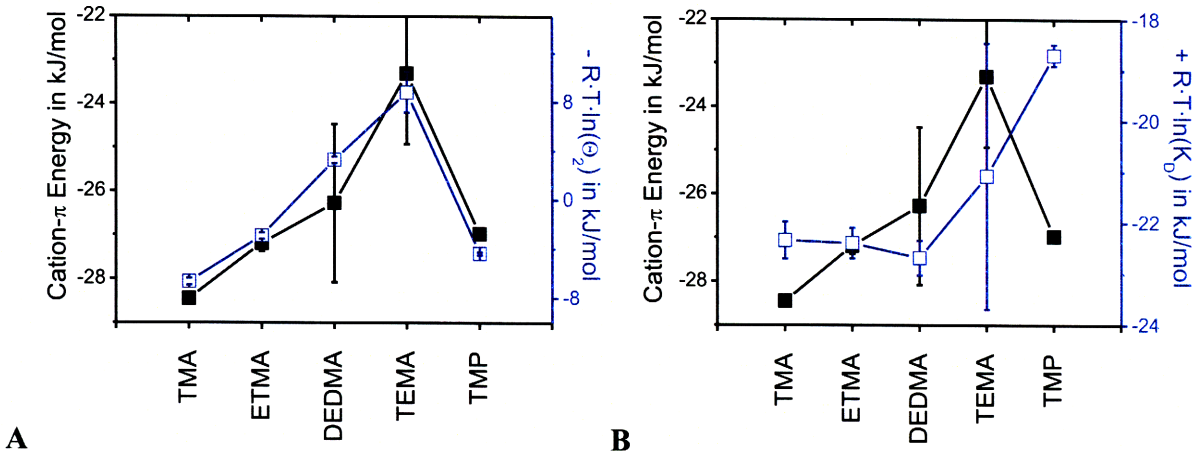

Figure II.12. Trends in the calculated cation-π binding energies, gating energies, and closed-state binding energies. (A) Gating energies (blue) follow the same trend as calculated cation-π binding energies (black). (B) Closed-state binding affinity (blue) is weakly correlated to cation-π binding energies (black).

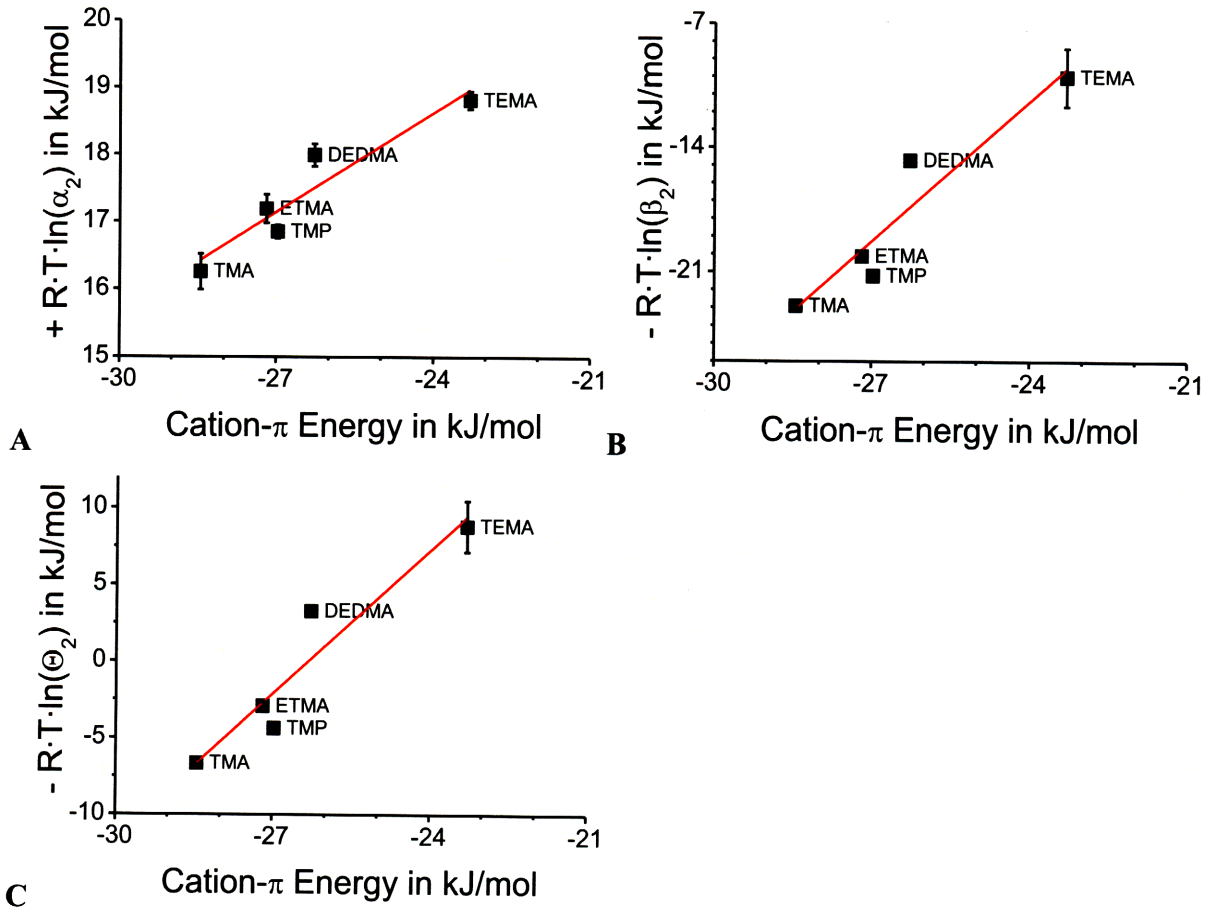

Figure II.13. Calculated cation-π binding energies correlate well with diliganded closing rate constants (A), opening rate constants (B), and gating equilibria (C). Red line, linear fits.

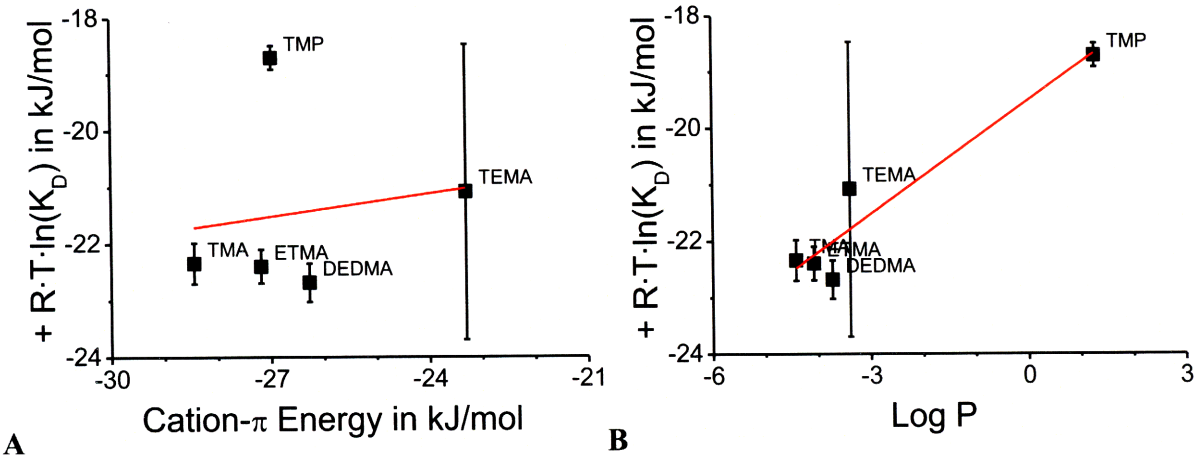

Figure II.14. Correlations with closed-state binding energies. (A) Cation-π binding energy is weakly correlated with closed-state binding affinity. TMP is a clear outlier, and a linear fit (red line) was obtained excluding TMP data with a slope near zero. (B) Log P correlates well with closed-state binding affinity, including TMP data.

Chapter III.

Evidence from single-channel recording that the acetylcholine receptor is more symmetrical in the open than the closed conformation

III.A Summary

One of the central issues in nicotinic acetylcholine receptor (AChR) physiology and pharmacology is the dynamic interaction between ligands and the transmitter binding sites. The α subunits contribute the principal agonist binding determinants at the transmitter binding sites. Structural studies have shown that the closed muscle-type AChR is asymmetric because the α subunits are rotated relative to non-α subunits, and functional studies have shown that the closed-state binding affinities can differ between the two sites. When agonist is bound to the AChR, all subunits overlay well, and the receptor is highly symmetric. Therefore, the increase in structural symmetry may translate to an increase in functional symmetry of the two transmitter binding sites; that is, we hypothesize that the open-state affinities are identical. We tested this hypothesis using single-channel recordings from heterologously-expressed adult mouse, muscle-type α^{G153S} mutant AChRs in the presence of the low-efficacy agonist choline. Both model-independent analyses and maximum-likelihood estimation of microscopic rate constants indicate that the open-state affinities are equivalent and that channel gating leads to an increase in functional symmetry. The two binding sites have non-equivalent closed-state affinities but equivalent open-state affinities, consistent with the hypothesis that the transmitter binding sites' principal faces primarily determine open-state affinity.

II.B Introduction

Understanding the conformation and the dynamics of agonist binding in the closed and open states of the nicotinic acetylcholine receptor (AChR) is a central issue for AChR pharmacology and rational drug design. Biophysical, biochemical, and electrophysiological methods have been used to investigate agonist and antagonist binding to the AChR (*1-6*), but capturing the dynamic molecular details of ligand interactions in the transient open state remains a challenging task. The muscle-type AChR is a ligand-gated ion channel required for synaptic transmission at the mammalian neuromuscular junction (NMJ). It is a pentameric complex made up of two α subunits, one β subunit, one δ subunit, and either one ε or one γ subunit, arranged in

clockwise order αβδαε when viewed from the synaptic cleft. The adult muscle-type AChR's two transmitter binding sites (TBSs) are situated at the α-δ and α-ε subunit interfaces. Cryoelectron microscopy of the intact AChR (*7*) and x-ray crystallography of acetylcholine-binding proteins (AChBPs) (*8, 9*) have provided high-resolution models; however, there are currently no definitive models of the agonist-bound closed or open states (*1*).

The AChR TBSs have been structurally and functionally characterized in the closed and desensitized states. The two TBSs are located in the N-terminal ligand-binding domain of the muscle-type AChR. Each TBS has principal components (Loops A–C) that make up the principal "face" of the binding site, and there are complementary components (Loops D–G) that make up the complementary face. The α subunit contributes the principal components, and the δ or ε subunit contributes the complementary components, depending on the subunit interface. In the closed state, the binding sites are functionally asymmetric; that is, the two sites are characterized by different agonist affinities and kinetics depending on receptor subtype and species (*10-15*). In the desensitized state, ligand-binding and stopped-flow fluorescence experiments indicate that the differences between the two sites are much smaller (*16, 17*). However, information about agonist binding in the transient open state has not been easily accessible in functional studies, and it is not clear what differences there may be between the open and desensitized states.

Two major conformational changes have been proposed to occur when agonists bind the AChR: closure of the Loop C binding determinant over the binding site and rotation of the α subunits. First, in the closed state, the AChR and AChBP models suggest Loop C is "uncapped". This conformation leaves the agonist binding site more open for ligand binding. With agonist bound, Loop C is shifted approximately 10 Å, "capping" the agonist-bound site (*7, 9*). Second, in the closed state, the α subunits overlay well with one another, and the non-α subunits overlay well with one another; however, the α subunits do not overlay well with the non-α subunits (*7*). The α subunits' interior β-sheets are rotated approximately 10°. A 9 Å resolution open-state model suggests the α subunits rotate so that all subunits overlay well, and the AChR becomes highly symmetrical (*18*) (**Figure 1A**). These static models have been of great use in developing structural models for the allosteric closed-to-open conformation change, called gating, but open-state agonist interactions are still not clear.

We propose that the dynamics of open-state agonist binding can be used to investigate the structure-function relationship relating to the symmetry of the TBSs. Single-channel

electrophysiology is one method to directly assay AChR open-state properties. For example, single-channel recording has previously been used to measure the rate of acetylcholine dissociation from open receptors (*19*). From structural studies, it is apparent that the α subunits induce an asymmetry in the closed state which is lost in the symmetric in the open state. We hypothesize that functional symmetry parallels this state-dependent change. Using electrophysiology, we test the hypothesis that the affinities of the TBSs are different in the closed state, but they are equivalent in the open-state. Comparing closed-state versus open-state affinities, the relative open-state contributions of the principal and complementary binding determinants are compared.

In considering the functional symmetry of the AChR, three plausible hypotheses can be put forward (**Figure III.1B**). First, the difference in the TBSs' open-state affinities could be larger than the difference in their closed-state affinities. Because the two TBSs differ structurally in their complementary faces, this observation would suggest that the complementary faces increase their contribution to agonist binding in the open state. Second, the difference in affinities could remain the same in the closed and open states. This observation would suggest increased open-state affinity is due to improved binding to both faces. Third, the difference in open-state affinities could be smaller than the difference in their closed-state affinities. Because the two TBSs have identical principal faces, this observation would suggest that the principal faces increase their contribution to binding in the open-state. Agonist binding is associated with the closure of Loop C and compaction of aromatic residues in Loops A–C. Thus, we expect that the third hypothesis is correct, and the receptor is both structurally and functionally more symmetric in the open state.

The hypothesis was tested using single-channel recordings of heterologously expressed mouse adult muscle AChRs. The low efficacy agonist choline has proven useful for a variety of AChR structure-function studies because it stimulates gating that is not faster than conventional patch-clamp recording bandwidth (*20-22*), while retaining the gating mechanism observed for stronger agonists (*23*). We used the previously characterized αG153S gain-of-function mutant, which primarily increases agonist affinity (*12, 24*). This permits a larger range of activity to be studied. Activation of this mutant using acetylcholine has previously been reported (*11, 12*). In those single-channel studies, closed-state acetylcholine affinities differed by less than 10-fold, and acetylcholine binding kinetics at the two different TBSs differed more substantially; however, the thermodynamics and kinetics of acetylcholine binding to the open state were not

investigated. Previous single-channel kinetic analysis of activation of this mutant with choline has only been conducted assuming equivalent sites, and the thermodynamics and kinetics of choline binding to the open state were not investigated (*24*).

For choline-stimulated αG153S AChR currents, a model-free analysis of open probabilities and dwell times supports the hypothesis that the TBSs are asymmetric in the liganded closed states but symmetric in the open states. Maximum-likelihood model fitting of single-channel activity was used to determine agonist binding, dissociation, channel opening, and closing rate constants. Assuming the AChR obeys detailed balance (*25*), loop balance was applied to the AChR thermodynamic cycle, and open-state affinities were calculated. We demonstrate that the binding sites are functionally asymmetric in the closed state and become symmetric in the open state, consistent with the previously characterized structural changes.

III.C Materials and Methods

Cell culture, electrophysiology, and single-channel analysis carried out using the same methods reported in **Chapter II**.

Materials.

Choline chloride was obtained from Sigma (St. Louis, MO), and cell culture reagents were from Invitrogen (Carlsbad, CA). Plasmids containing the adult mouse muscle acetylcholine receptor subunit cDNAs in the pRGB4 vector were generously provided by Professor Anthony Auerbach (SUNY Buffalo, Buffalo, NY) (*26*). The α subunit contains the previously described V433A background mutation which does not affect channel kinetics and is referred to as wild-type (*11*). The αG153S mutation was engineered by site-directed mutagenesis using a Qiagen QuickChange Kit (Valencia, CA) (*11, 12, 24*). Plasmid sequences were confirmed by dideoxy sequencing at the MIT Biopolymers Laboratory (Cambridge, MA).

Cell Culture.

HEK-293 human embryonic kidney cells (ATCC CRL-1573) were maintained in Dulbecco's Minimum Essential Media (DMEM) supplemented with 10% Fetal Bovine Serum (FBS) at 37°C in a 5% CO_2 humidified atmosphere. Cells were transfected at 40-60% confluency using the method of calcium phosphate precipitation according to previously

published protocols (*11*). For one 35 mm dish, a total of 3.5 μg of plasmid DNA was used in a mass ratio of 2:1:1:1 of α:β:δ:ε subunits. Media was changed 8-30 hours after addition of DNA, and patch-clamp experiments were conducted 24-72 hours after media change.

Justification for Use of the αG153S Mutant

The αG153S mutation has been shown to increase the closed-state affinity of agonists (*12*), and its use allows a range of choline concentrations to be used. Because we use a gain-of-function mutation in these studies, we first justify its use. In this study we are interested in the functional symmetry between the two TBSs and how their symmetry is different in the closed and open states. Because the mutation occurs on the α subunits, it does not change the symmetry of the system because there is one α subunit at each TBS. Therefore, use of this system is still appropriate for comparing principal face and complementary face binding contributions in the closed versus open state.

Justification for Assuming the AChR Obeys Detailed Balance

Detailed balance, or microscopic reversibility, requires that the AChR operate at thermodynamic equilibrium in the absence of a source of additional free energy. For the AChR which has no enzymatic component, this free energy can only come from the ion gradient. If a permeant ion were to bind the pore, this could affect gating and cause violations of detailed balance. However, AChR permeant ion block is not detected in single-channel recordings, suggesting the ion gradient is not coupled to AChR gating. Furthermore, in early studies of the AChR, no temporal asymmetries were detected in bursts of openings, consistent with detailed balance (*25*).

Electrophysiology.

Single-channel recording was performed in the cell-attached mode according to previously published protocols (*27, 28*). Before recording, transfected cells were washed with Dulbecco's Phosphate Buffered Saline (DPBS) containing in mM: 137 NaCl, 0.9 $CaCl_2$, 0.5 mM $MgCl_2$, 2.7 KCl, 1.5 KH_2PO_4, 8.1 Na_2PO_4, pH 7.3. The bath solution was DPBS, and pipette solutions were DPBS supplemented with choline. Pipette resistances were typically 10-20 MΩ, and pipettes were held at a command voltage of -70 mV during recording. Membrane potentials

were usually -30 to -40 mV. Single-channel currents were amplified with an Axopatch 200B (Axon Instruments, Foster City, CA) and recorded through a low-pass Bessel filter at 10 kHz. Data was digitized at a sampling rate of 20-100 kHz using a NI 6040 E Data Acquisition Board (National Instruments, Austin, TX). Data was recorded using QuB software (www.qub.buffalo.edu).

Kinetic Analysis.

Single-channel records were processed using the QuB software suite (*29-32*). Data were idealized using the segmental K-means algorithm. Dwell-time distributions were fitted, and time constants were determined using the maximum-likelihood algorithm in QuB as previously described (**Chapter II**). At high, desensitizing choline concentrations, single-channel activity is clustered, and clusters were identified using a critical time t_{crit} as previously described (**Chapter II**) (*11, 28, 33*). For fitting, clusters of homogeneous activity were used. Homogeneous clusters were used if their activity fell within 1–2 standard deviations (SDs) of the mean current amplitude, mean closed time, and mean open time as has been previously done (*11*). Single-channel clusters recorded at 0.25, 0.5, 1, 2, and 5 mM choline were globally fitted to AChR gating models (**Scheme III.1** and **III.2**), using the maximum interval likelihood algorithm with missed event correction. A dead time of 2.5 times the sampling interval was imposed. Fitting was repeated multiple times (10-50 repetitions) for each model with rate constant perturbations to provide higher confidence that the fitted model did not represent erroneous convergence. An additional gap state has been previously described and used in AChR gating models (*11*); however, a gap state did not significantly improve fitting and in most cases caused non-convergence or poor fitting. Furthermore other models incorporating choline-dependent block or additional diliganded open states also did not improve fitting.

Deterministic Simulation of Macroscopic Behavior.

Macroscopic channel behavior was simulated by calculating time-dependent state occupancies using previously described Q-Matrix methods in MATLAB (The MathWorks, Natick, MA) (*28*). The validity of these simplified calculations were verified by comparing Q-matrix calculated macroscopic currents to previously published experimental and M-Cell simulated synaptic currents (*24*). Previously reported rate constants for wild-type and mutant

acetylcholine activation measured within the same studies were used in order to avoid comparing rate constants measured under different experimental conditions (*12, 34*).

III.D Results

To test the hypothesis that the TBSs have distinct closed-state choline affinities but symmetric open-state affinities, we estimated closed-state and open-state affinities of choline to the αG153S mutant receptor using single-channel kinetic analysis. The activity of single-channels was fitted to a kinetic model which allows for non-equivalent affinities, that is, the agonist binding steps are allowed to be distinct (**Scheme III.1**). This type of model is commonly used to fit AChR activity (*11, 12, 35, 36*). A simplified model which imposes equivalent affinities is also commonly used to fit adult muscle-type AChR kinetics (*37*) (**Scheme III.2**). This scheme is often a good model for adult muscle-type AChR activity because the two TBSs have similar closed-state agonist affinities. However, both models are physically reasonable, and **Scheme III.1** allows for the possibility of non-equivalent affinities. It is important to note that this model does not require non-equivalent affinities. Hence, we used **Scheme III.2** as a more general model which is suitable for testing the hypothesis that the TBSs are functionally asymmetric in the closed state but symmetric in the open state. We take the approach of first making model-independent measurements of gating. We then used these model-independent measurement to constrain fitting of kinetic models, as is commonly done (*11, 37*).

Binding Sites Contribute Unequally to Gating

Initially, we tested the functional equivalence of the binding sites by recording the activity of hybrid channels containing a wild-type and a mutant α subunit, and we find the sites contribute unequally to gating, as observed by others (*38*). Cells were transfected with both the wild-type α and mutant α^{G153S} cDNAs, along with wild-type β, δ, and ε cDNAs. Because muscle-type AChRs contain two α subunits, four populations of AChRs exist when cells express both wild-type and mutant α subunits, differing at the TBSs. Channels can assemble in which both binding sites are wild-type, both sites are mutated, the α-δ site is mutated ($hybrid_\delta$), or the α-ε site is mutated ($hybrid_\varepsilon$) (*38*). Currents were recorded at 20 mM choline to saturate receptors (4 patches) (*39*). Four distinct modes of channel activity were observed, demonstrated in the distribution of open probabilities (**Figure III.2AB**). For equivalent sites that contribute equally

to gating, single-channel activity from the two hybrid populations would be indistinguishable, as has been observed for transmembrane-region mutants (*40-42*). In this case, three modes of activity would be observed: wild-type, hybrid, and mutant. In contrast, for non-equivalent sites that contribute unequally to gating, two distinguishable subsets of hybrid channel activity are predicted (*38, 42*). In this case four modes of activity would be observed. Four modes of activity were observed, and a segmental k-means algorithm was used to fit the open probabilities to four Gaussian curves: wild-type 0.12 ± 0.02, hybrid 0.33 ± 0.04, hybrid 0.54 ± 0.04, mutant 0.80 ± 0.03 (mean ± standard error). Gating rate and equilibrium constants of the four populations were determined (**Table III. I**). As expected, the two transmitter binding sites contribute unequally to gating (*38*).

Although two hybrid activities were observed, the hybrid closing rate constants are equal, consistent with identical open-state TBSs in support of our hypothesis. Only one open lifetime was necessary to fit hybrid openings for the number of fitted events. However, two distinct open lifetimes might be too similar in magnitude to distinguish. The ratio of the two hybrid lifetimes is 1.1 ± 0.1 (mean ± standard error), indicating that if there are two distinct lifetimes, they are unlikely to differ by more than 20-30%.

Because the currents analyzed above were recorded at 20 mM choline to saturate receptors, unresolved fast block prolongs the apparent open events, resulting in underestimation of the diliganded closing rate α_2 by 2-fold (*39*). However, this phenomenon occurs for all four receptor populations and, therefore, does not affect the analysis of binding site independence used here.

We also demonstrate that the αG153S mutations are not coupled between TBSs. Because the AChR is an allosteric protein complex, mutations might be energetically coupled. The binding sites are generally considered independent of one another (*11, 38*), but coupling due to the mutation would make **Scheme III.2** inappropriate for fitting single-channel activity. To address this question, single-channel activity was measured from hybrid channels containing one wild-type and one G153S mutant α-subunit. The kinetic behavior of the hybrid channels is consistent with independent TBSs that contribute unequally to gating.

Thermodynamic mutant cycle analysis indicates that the αG153S mutations at the two TBSs are uncoupled. Because the receptors are saturated, the observed differences in P_o are due to diliganded gating. Gating rate constants for each population were estimated using a

maximum-likelihood algorithm assuming a two-state open-closed model (*38*). For independent perturbations, the change in gating free energy due to the αG153S mutation at each binding site is path-independent. In terms of free energy, the equality $\Delta\Delta G_{gating}$(wild-type to hybrid$_\delta$) + $\Delta\Delta G_{gating}$(hybrid$_\delta$ to mutant) = $\Delta\Delta G_{gating}$(wild-type to hybrid$_\varepsilon$) + $\Delta\Delta G_{gating}$(hybrid$_\varepsilon$ to mutant) should hold (*38*). In terms of diliganded gating equilibrium constants, non-interacting binding sites predicts $\Theta^{WT}\cdot\Theta^{Mut}$ / $\Theta^{Hybrid1}\cdot\Theta^{Hybrid2}$ = 1. We observed that the ratio $\Theta^{WT}\cdot\Theta^{Mut}$ / $\Theta^{Hybrid1}\cdot\Theta^{Hybrid2}$ = 0.9 ± 0.3 (mean ± standard error) is approximately 1, suggesting the energetic contribution of each binding site is independent (**Figure III.2C**).

Using the measured gating rate and equilibrium constants of the four populations, the rate-equilibrium free energy relationship (REFER) for wild-type, hybrid, and mutant activity was also determined. REFER analysis, plotting log β_2 versus log Θ_2, measures the relative position of the transition state along the conformational reaction coordinate, and has been used as an indicator of relative timing of AChR domain motions in the gating conformational change (*23, 43*). If the dynamics of the independent α subunits were asynchronous during the gating reaction, nonlinear curvature in the REFER plot would be expected because each of the hybrid channels would give rise to a different slope in the REFER plot (*42*). In fact, REFER coordinates of the wild-type, mutant, and the hybrid αG153S populations are collinear (R^2 = 0.98 ± 0.01, mean ± standard error), suggesting that the binding sites have similar gating transition state conformations and relative timing of conformational motions (**Figure III.2D**). The slope of the linear REFER is Φ = 0.79 ± 0.03 (mean ± standard). The Φ-value is close to 1, as expected for the transmitter binding sites (*20, 23*). This value suggests choline activation of the αG153S AChR does not utilize an allosteric mechanism unique from wild-type receptors, supporting the use of **Scheme III.2**.

Model-Independent Measurements of the Gating Rate Constants α_1, α_2, β_2

Functional asymmetry of the open-state binding sites predicts that there are four AChR open states, and symmetry of the open-state binding sites predicts that there are three open states. To determine the number of open states and their associated lifetimes, single-channel activity was measured at low choline concentrations (numbers of patches: 1 at 1 nM, 7 at 10 nM, 7 at 100 nM, 5 at 1 μM, 6 at 10 μM, 26 patches total). At low choline concentrations, single-channel activity is not clustered, and closed and desensitized sojourns cannot be distinguished. Thus,

only open dwell-time distributions were analyzed. Sums of exponentials were fitted to the open dwell-time distributions, and time-constant analysis was performed. An example of an open dwell-time distribution observed at 100 nM choline is shown in **Figure III.3A**.

Open events could be classified into short (0.14 ± 0.02 ms, mean ± SD), intermediate (0.6 ± 0.1 ms), and long (1.2 ± 0.2 ms) lifetimes, consistent with symmetric open-state binding sites. The relative amplitudes of these open lifetimes were concentration dependent (**Figure III.3B**). The short-lifetime open state steadily decreased in relative amplitude with increasing concentration. For the intermediate-lifetime open state, the relative amplitude exhibited a bell-shaped concentration dependence with a maximum at ~10^{-5}-10^{-4} M. The long-lifetime open state was absent at very low concentrations and steadily increased in relative amplitude with increasing concentration. The magnitude of the three open lifetimes and the concentration dependences of their relative amplitudes indicate that they correspond to openings of the unliganded, monoliganded, and diliganded αG153S AChR. The shortest lifetime was consistent with the reported unliganded lifetime (*24*) and can be assigned to the unliganded open state. The longest lifetime is consistent with our measurements at saturating choline concentrations (**Table III.I**) and can be assigned to the diliganded open state. The monoliganded open state is unlikely to have a lifetime shorter than the unliganded open state or longer than the diliganded open state. The intermediate open lifetime therefore can be unambiguously assigned to a monoliganded open state. A histogram of the open lifetimes observed in all the low concentration records clearly shows three peaks (**Figure III.3C**). A Gaussian was fitted to each peak, and the channel closing rate constants were determined: the unliganded closing rate constant α_0 (7000 ± 1000 s^{-1}), the monoliganded closing rate constant α_1 (1900 ± 400 s^{-1}), and the diliganded closing rate constant α_2 (1100 ± 200 s^{-1}). It is not surprising that the unliganded and monoliganded open states are easily observable, as other gain-of-function mutants have shown a propensity for opening with fewer than two agonist molecules bound (*44*).

Notably, only one monoliganded open lifetime was observed, consistent with the hypothesis that the open-state TBSs are functionally identical. Additional monoliganded open states were not necessary given the number of events fitted. These data do not rule out the hypothesis that there are two distinct monoliganded open state with lifetimes that differ by 10% or less (as judged by least-squares fitting of the histogram in **Figure III.3C**) and are therefore

not resolved as individual components. However, the existence of two monoliganded lifetimes of similar lifetimes would not impact the model fitting conducted below.

To determine diliganded gating rate constants, single-channel activity was recorded at high concentrations of choline (numbers of patches: 4 at 0.25 mM, 4 at 0.5 mM, 4 at 1 mM, 5 at 2 mM, 4 at 5 mM, 21 total). Single-channel activity was observed as clusters at these concentrations (**Figure III.4A**). The choline dependence of the intracluster open probability was fitted to a Hill equation to estimate the effective concentration for half-maximal activation (EC_{50} = 1.2 ± 0.4 mM) and maximum open probability (P_o^{max} = 0.6 ± 0.1) (**Figure III.4B**). The apparent opening rate, β_2', is the reciprocal of the major intracluster closed-time component that scales with agonist concentration. The dose response of β_2' was fitted to a Hill equation to estimate the true microscopic opening rate constant (β_2 = 2200 ± 700 s^{-1}) (*11, 28, 45*) (**Figure III.4C**).

The diliganded closing rate constant, α_2, was measured from the dose response of the mean open time τ_O, and the gating equilibrium was measured from β_2 and α_2. Choline is useful as a low-efficacy agonist which induces resolvable gating events, but fast open-channel blockade also occurs at high concentrations. When fast blockade is present, the observed mean intracluster open time is $\tau_O = \alpha_2^{-1} + (\alpha_2 \cdot K_{Block})^{-1} \cdot [choline]$ (*28, 46, 47*) (**Figure III.4D**). The diliganded closing rate constant (α_2 = 1300 ± 100 s^{-1}) and choline blocking equilibrium constant ($K_{Block} \sim 10^{-2}$ M) were determined. Fast choline block of the mutant is not different from the wild-type channel (K_{Block} ~ 10 – 20 mM), as expected from the location of residue G153 in the binding site, far from the ion conduction pore. The concentration dependence of τ_o was observed to be shallow and linear, indicating that fast choline block is not severe up to 5 mM. Furthermore, the diliganded closing rate constant determined at high choline concentration is consistent with its estimate at low choline concentration. From the diliganded gating rate constants, we estimate $\Theta_2 = \beta_2/\alpha_2 = 1.7 \pm 0.6$.

Four Closed Dwell-Time Components Suggests Two Distinct Binding Steps

The intracluster closed dwell-time distributions observed at 0.25 mM choline exhibited four closed components, suggesting that there are two binding events with distinct closed-state affinities that can be detected. At 0.25 mM choline single-channel clusters can be isolated, and ensemble averaging does not obscure microscopic steps. At this concentration, the receptors are

not highly saturated, and all the conformational and bound states are sampled. The number of exponential components in the closed dwell-time distribution equals the number of kinetically distinguishable closed AChR states (*28*). For identical binding sites, there are three distinguishable closed states: one unliganded, one monoliganded, and one diliganded closed state. Three closed components would be observed in the closed dwell-time distributions. For non-equivalent binding sites, there are four distinguishable closed states: one unliganded state, two distinguishable monoliganded closed states, and one diliganded closed state. Four closed components would be observed. We observed four closed components at 0.25 mM choline (4 out of 4 patches) (**Figure III.5**). Fits of the distribution to four components were significantly better than fits to three components. Approximately 25000 events were observed for each record, and according the to the Schwartz criterion for this number of events, an increase of 5 in the log-likelihood score is significant (*48*). The log-likelihood score improves by 13 ± 3 (mean ± standard error), a value which is by the Schwartz criterion and also the Likelihood Ratio Test (α=0.001). In contrast, addition of a fifth component only improved the likelihood score by 1.1 ± 0.6, which is not significant. The four closed time components were similar in magnitude, leading to broad distributions and an absence of four well-separated peaks. Thus, they could not be analyzed in a model-independent manner. However, these observations are consistent with asymmetric agonist binding sites in the closed state, indicating that fitting of **Scheme 2** may reveal distinct closed-state affinities.

Maximum-Likelihood Model Fitting and Rate Estimation

Using maximum-likelihood model fitting, **Scheme III.2** was shown to be a statistically better model of αG153S AChR activity than **Scheme III.1**. The clusters of single-channel activity recorded at 0.25, 0.5, 1, 2, and 5 mM choline (**Figure III.4**) were simultaneously fitted to equivalent (**Scheme III.1**) or non-equivalent (**Scheme III.2**) independent binding sites models using the maximum idealized likelihood algorithm in the QuB software suite (http://qub.buffalo.edu) (*11*). The clusters that exhibited stationary and homogeneous single-channel activity were selected for fitting as described in the **Materials and Methods** section (*11*). At each concentration, the clusters from all patches were pooled, and data from all concentrations were fit simultaneous to the models. Unliganded openings are not included in the models because they are extremely rare at the analyzed concentrations. The diliganded gating rate constants were determined in a model-independent manner as described above, and

therefore, they were constrained to $\alpha_2 = 1300 \pm 400\ s^{-1}$ and $\beta_2 = 2200 \pm 700\ s^{-1}$ during fitting. Monoliganded openings still occur frequently at these concentrations, and they are included in the model for fitting. Only one monoliganded lifetime was observed, and its monoliganded closing rate was determined in a model-independent manner as described above. Therefore, α_1 was constrained to $1900 \pm 100\ s^{-1}$ for both monoliganded open states in **Scheme III.2** during fitting.

Using these constraints, the non-equivalent, independent binding sites model (**Scheme III.2**) fitted the data well and was a statistically better descriptor than the equivalent binding sites model (**Scheme III.1**). It is difficult to determine by inspection which model produced calculated probability distributions that better fit the observed dwell-time distributions. (**Figure III.6**) This is consistent with the utility of the equivalent binding sites model in many scenarios where discrimination of the binding sites is not necessarily possible or important to the question at hand. However, the non-equivalent binding model is, for the results in the current study, a significantly better descriptor of the data statistically. The fitted equivalent sites model log-likelihood score is 2543496 compared to the fitted non-equivalent sites model score of 2562432, an increase of 18936 in probability score with only three additional free parameters. This difference is significant by the Schwartz criterion and Likelihood-Ratio Test (α=0.001) (**Table III.2**) (*49*). Therefore, the rate constant estimates from the fitted non-equivalent binding sites model were used for further analysis.

Closed-State Affinities Are Non-Equivalent, Open-State Affinities Are Equal

Rate estimates from fitting **Scheme III.2** show that the two TBSs have distinct closed-state binding and dissociation kinetics and differ in closed-state affinity by 10-fold; however, the estimated open-state affinities are equal (**Table III.2**). For simplicity, the superscript labels "H" and "L" are used to indicate high and low affinity. The kinetics of choline association and dissociation differ substantially. The association rates differ by ~100-fold, with faster association to the low-affinity site ($k_+^H \sim 10^4\ M^{-1}\ s^{-1}$ versus $k_+^L \sim 10^6\ M^{-1}\ s^{-1}$). The dissociation rates differ by 1000-fold, with faster dissociation from the low-affinity site ($k_-^H \sim 10^1\ s^{-1}$ versus $k_-^L \sim 10^4\ s^{-1}$). The high-affinity binding site has a choline closed-state dissociation constant $K_D^H \sim 0.1$ mM, and the low-affinity site has a choline closed-state dissociation constant $K_D^L \sim 1$ mM.

In contrast, we estimate that the open-state choline dissociation constants are equivalent: $J_D^H \sim J_D^L \sim 50$ μM. Open-state association and dissociation rate constants are difficult to measure (*19*) and were not directly observed here. Instead, the open-state dissociation constants, J_D^L and J_D^H, can be determined by applying loop balance, a consequence of detailed balance, to the AChR conformational cycle (**Figure III.6**) (*25*). Invoking loop balance, it follows that $K_D^L \cdot \Theta_1^H \cdot J_D^H = K_D^H \cdot \Theta_1^L \cdot J_D^L$. Using monoliganded gating equilibrium constants, $\Theta_1^L \sim 0.1$ and $\Theta_1^H \sim 0.01$, and closed-state affinities, we find that $J_D^L \sim J_D^H$. Loop balance allows us specifically to write $J_D^L \cdot \Theta_2 = K_D^L \cdot \Theta_1^H$, such that $J_D^L = 40 \pm 20$ μM, and to write $J_D^H \cdot \Theta_2 = K_D^H \cdot \Theta_1^L$, such that $J_D^H = 60 \pm 20$ μM. Hence, the TBSs are more functionally asymmetric in the closed receptor ($K_D^H \sim 10 \cdot K_D^L$) and more symmetric in the open receptor ($J_D^H \sim J_D^L$), at least in terms of binding energy and affinity.

III.E Discussion

State-Dependent Changes in Binding Site Organization

Single-channel kinetic analysis of the αG153S AChR activated by choline has demonstrated that the two TBSs have non-equivalent closed-state affinities but equal open-state affinities. Structural data suggests that the closed AChR has an asymmetric ligand-binding domain because the two α subunits are rotated relative to the non-α subunits (*7*). In contrast, all subunits have equivalent conformations in the open AChR, and the ligand-binding domain is symmetric (*18*). Our results are consistent with the functional predictions of this structural model. Specifically, the binding sites have closed-state choline affinities which differ by 10-fold (~300 μM versus ~3000 μM) but have equivalent open-state choline affinities (~50 μM). This functional information can be used to infer details about changes in the molecular organization of the agonist binding sites upon channel gating.

Regardless of the state of the receptor, the differences in binding affinity and selectivity between the two TBSs may be attributed largely to residues on the complementary face in Loops D–G. Because the principal face is formed by α subunits at both sites, binding interactions between Loops A–C and the agonist are expected to be similar, if not identical, for the two binding sites. The complementary face is formed by the δ subunit at one TBS and the ε subunit at the other TBS. Asymmetry in closed-state agonist affinities indicates that the complementary faces contribute appreciably to ligand-channel interactions. Several residues on the

complementary face have been implicated in determining differential agonist and competitive antagonist affinities and specificities between the two sites in the closed AChR (*13-17, 50, 51*).

We observe that the TBSs have equal open-state affinities, suggesting that their principal faces increase their fractional contributions to agonist binding in the open state compared to the closed state (**Figure III.7**). The fractional contributions of the complementary faces decrease in the open state so that the principal faces primarily determine open-state affinity. Currently, there are no models for the agonist-bound closed and open states. The agonist-bound AChBP structures are thought to mimic the desensitized state, and it is not clear what differences exist between the open-state and desensitized state TBSs. However, our results are consistent with models comparing the agonist-free closed state and agonist-bound desensitized state. In x-ray protein crystal structures of carbamylcholine- or nicotine-bound AChBP, the agonist-buried surface area is approximately 2-fold greater for the principal face than the complementary face, suggesting the agonist makes a larger number of contacts with the principal face (*52*). The bound agonist may also be stabilized by closure of Loop C and compaction of the aromatic "cage", both α subunit components (*7*). Our results therefore also suggest that the TBS is structurally similar in the open and desensitized states, as has been hypothesized (*53*). Both of these states are high affinity conformations with slow rates of agonist dissociation (0.1-10 s^{-1}) (*16, 17, 19*). It has also been previously reported that the binding affinities for the two TBSs in the desensitized state are similar to each other (*16, 17*). While our functional studies suggest that the open-state and desensitized-state conformations of the transmitter binding sites are similar, a definitive answer to the question of open-state binding site conformation must await structural experiments that allow characterization of local residue environments in transient states. It may also be interesting to examine changes in functional symmetry for other agonists. Unlike acetylcholine, choline lacks a carbonyl moiety which has been shown to be a pharmacophore. This may indicate that for quaternary ammonium containing cholinergic agonists, the charged moiety is largely stabilized by the principal face while the complementary face has a larger fractional contribution to stabilization of the carbonyl and non-charged moiety.

Unequal Contributions to the Energetic Driving Force of Gating

The results presented here also confirm that the two binding sites contribute unequally to the total free energy of the gating reaction, as previously reported (*54*). As discussed in the **Results** section, analysis of hybrid channels in previous studies has indicated that the binding

sites contribute unequally to gating (*38*). Our analysis further demonstrates that the difference between closed- and open-state affinities at the high-affinity site is much smaller than the difference in closed- and open-state affinities at the low-affinity site. Therefore, binding at the low-affinity site contributes more to the free energy difference between closed and open states than binding at the high-affinity site. Because the differential binding affinity in closed and open states ultimately provides the driving force for agonist-gated channel opening, agonist binding to the low-affinity site is the major factor in driving the gating reaction. Structurally, the low-affinity site would thus also be expected to undergo a conformational change of commensurately greater magnitude. Interestingly, the choline binding rate constant for the high affinity site is particularly slow ($\sim 10^4\ M^{-1} \cdot s^{-1}$). The high affinity site's slow on-rate might be rationalized by a similarity between its closed state structure and the compact structure of the open state, assuming that the binding and unbinding processes are slower for the more compact states.

It might be argued that the ~10-fold affinity difference associated with functional asymmetry is only a minor contributor to the overall thermodynamics of gating, and thus not mechanistically significant. In terms of thermodynamics, a 10-fold affinity difference translates to an energetic difference of only ~ 5 kJ/mol binding free energy, roughly that of a single weak hydrogen bond and not very large compared to ambient thermal energy (kT). However, effects of this magnitude can be very important in physiological context. Our results demonstrate that the moderate asymmetry in binding affinities is associated with large asymmetries in agonist binding kinetics. In fact, these kinetic asymmetries appear to be the more critical issue when considering synaptic transmission, given the far-from-equilibrium nature of that process. We examine in greater detail the possible physiological implications of the kinetic asymmetry of the binding sites below.

Asymmetric Agonist Binding Site Kinetics Predicts a Dominant αG153S-Associated Phenotype for Slow-Channel Myasthenic Syndromes

The results of this work provide evidence that AChR activity is best described by **Scheme III.2**, in which the closed AChR has functionally asymmetric binding sites, but the open-state binding sites are symmetric. However, the physiological importance of such distinctions is not immediately clear, especially since both symmetric and asymmetric models have been used in various single-channel kinetic analyses throughout the literature. (*12, 34*)

Previous studies have not commented on how these different models might lead to different physiological consequences. To examine the question of physiological relevance we used either symmetric or asymmetric models to simulate AChR activity at the neuromuscular junction and assessed predicted differences in synaptic transmission. We found that symmetry considerations in AChR gating kinetics may be important in understanding not only the molecular-level gating mechanism but also the molecular pathology of slow-channel congenital myasthenic syndromes (SCCMSs).

SCCMSs are associated with impaired neuromuscular transmission and muscle weakness. A large fraction of SCCMS cases are associated with AChR mutations that perturb channel kinetics, and many of these mutations specifically slow down agonist dissociation (*55*). The kinetic distinction between the two agonist binding sites might help explain the dominant inheritance pattern of SCCMS associated with slowed agonist dissociation. The decay of the muscle-type AChR synaptic current is determined by channel gating and fast agonist dissociation from *either* of the two binding sites, since a single dissociation event highly disfavors channel opening. For a SCCMS-associated mutation occurring on the α-subunit, heterozygous patients will have four populations of channels: both binding sites wild-type, both sites mutated, the α-δ site mutated, or the α-ε site mutated. With this mixed population (neglecting possible effects such as decreased channel expression), the ensemble behavior of the two different hybrid $\alpha^{wildtype}/\alpha^{mutant}$ populations could drastically influence the overall phenotype.

The ensemble behavior of the mixed population can be analyzed in the context of either symmetric or asymmetric binding models. The two kinetic models, symmetric versus asymmetric binding, make different predictions about the properties of the two different hybrid $\alpha^{wildtype}/\alpha^{mutant}$ populations and the associated disease phenotype. The symmetric binding model predicts that the synaptic response of hybrid channels is no different from wild-type channels (**Figure III.8A**). Because AChR synaptic current decay is partially determined by fast agonist dissociation and because both sites exhibit fast agonist dissociation, the kinetic symmetry acts as a level of redundancy which can protect against impaired function at just one site. Therefore, the symmetric model predicts that mutation and decreased agonist dissociation at just one site would not cause a delayed synaptic current decay. Fast agonist dissociation from the second wild-type site would still be competent to terminate activity quickly, rescuing the ensemble

phenotype of all hybrid channels at the NMJ. In this scenario, mutation at both sites is required to produce the slow-channel phenotype.

In contrast, if transmitter binding sites are non-identical, mutation in only one site is sufficient to produce the slow-channel phenotype. When binding sites are asymmetric, there is a high-affinity and a low-affinity site. Low affinity is caused primarily by an increased rate of agonist dissociation as seen in our experiments and previous reports with both mammalian and *Torpedo* receptors (*10, 12*). With one "slow" and one "fast" agonist dissociation site, the AChR current decay time course is determined primarily by the site with faster dissociation. Therefore, the slow-channel phenotype is due solely to mutation in the low-affinity site, which slows the fast agonist dissociation step and the rate of synaptic current decay. In this scenario, half the hybrid channels will behave like wild-type channels, and half the hybrid channels will exhibit the slow-channel phenotype because there is no rescue by a second fast site (**Figure III.8B**).

A symmetric model predicts that 25% of the channels at a heterozygous SCCMS patient's NMJ will be dysfunctional, while an asymmetric model predicts that 50% will be dysfunctional; however, whether or not this will lead to an observed difference in synaptic behavior is not immediately obvious. To determine quantitatively whether differences in the hybrid populations might be meaningful in shaping the time course of synaptic currents, two clinically-identified SCCMS-associated mutations were analyzed in simulations. The αN217K and αG153S mutations are slow-channel mutations with similar clinical phenotypes and similar molecular pathologies due to slowed agonist dissociation (*12, 34, 56*). Acetylcholine-induced gating of each mutant has previously been examined at the single-channel level. For the αN217K mutant, acetylcholine activation was characterized with a symmetric binding sites model (**Scheme III.1**) (*34*). For the αG153S mutant, acetylcholine activation was characterized using an independent, asymmetric binding sites model (**Scheme III.2**) (*12*). Given the similarity of the mutations, the disease phenotype and inheritance, predictions of both published symmetric and asymmetric binding models can be analyzed and compared to reported clinical data. Q-matrix methods were used to simulate the macroscopic AChR synaptic currents in response to a 1 mM acetylcholine pulse of duration 0.5 milliseconds (variations of impulse height and width did not affect the predictions) (*28*).

The simulations of AChR synaptic currents using a symmetric binding model predict a mild change in phenotype due to a heterozygous SCCMS-associated mutation, suggesting

recessive inheritance of the phenotype. The previously published microscopic rate constants for the clinically-identified αN217K mutant, obtained assuming a symmetric binding sites model, were used in the simulations (**Table III.3**) (*34*). Synaptic currents due to the wild-type, the single hybrid, and the doubly mutant channel populations were analyzed individually and as the 1:2:1 mixture that might be found at the neuromuscular junction of a heterozygous SCCMS patient. In the simulations, only the doubly mutant receptors display the disease phenotype. Therefore, assuming symmetric binding kinetics in a heterozygous patient, only 25% of the AChR population at the NMJ would be expected to be doubly mutant and have slow-channel characteristics. At the simulated heterozygous NMJ, the total current decays similarly to the wild-type current, suggesting that the phenotype will be inherited as a recessive trait (**Figure III.8C**). However, the αN217K-associated disease is found to be dominantly inherited in clinical studies (*56*), contrary to the prediction from the kinetic simulations that assume a symmetric binding model.

In contrast to the predictions of the symmetric binding model, simulations of AChR synaptic currents demonstrate that the asymmetric binding model predicts a pronounced change in phenotype due to a heterozygous SCCMS-associated mutation, suggesting dominant inheritance. Rate constants for the clinically-identified αG153S mutant, obtained from fits to an asymmetric binding model, have previously been published (**Table III.4**) (*12*). Using these rate constants for simulations, the synaptic currents due to the wild-type, the two distinct hybrids, and the doubly mutant channel populations can be analyzed individually and as the 1:1:1:1 mixture that might be found the neuromuscular junction of a heterozygous SCCMS patient. In these simulations, both hybrid receptors bearing the mutation at its low-affinity/fast-dissociation site and the doubly mutant receptors exhibit the slow-channel phenotype. In a heterozygous patient with asymmetric binding kinetics, 50% of the AChR population is expected to be kinetically defective. This causes a qualitatively pronounced change in synaptic current, increasing the decay time roughly 200% and suggesting a dominant phenotype (**Figure III.8D**). Clinically, the αG153S mutation leads to a dominant disease-associated phenotype (*12*), consistent with the prediction of the kinetic simulations.

Simulations of currents at the neuromuscular junction show that the asymmetric binding sites model established *in vitro* by single-channel kinetic analyses may also help explain the clinical observation that SCCMS are inherited as dominant traits. In addition to the AChR,

many other ligand-gated ion channels exhibit high structural symmetry and multiple ligand binding sites. Similar kinetic analyses and simulations of synaptic currents may therefore prove to be generally useful in explaining and predicting phenotypes of channel mutations for heterozygous genotypes.

III.F Conclusions

We have conducted structure-function studies which support the hypothesis that the AChR has unequal closed-state affinities and equal open-state affinities. Our results suggest that open-state binding affinities are primarily determined by the α subunits, that the transmitter binding sites are structurally similar to one another, and that the open- and desensitized-state TBS structures are not vastly different. Functional studies are complementary to structural models, and we have demonstrated the utility of structure-function studies in assessing conformational dynamics of the transient open state.

III.F References

1. Gay, E. A., and Yakel, J. L. (2007) Gating of nicotinic ACh receptors; new insights into structural transitions triggered by agonist binding that induce channel opening. *J. Physiol. 584*, 727-733.
2. Sine, S. M. (2002) The nicotinic receptor ligand binding domain. *J. Neurobiol. 53*, 431-446.
3. Sine, S. M., and Engel, A. G. (2006) Recent advances in Cys-loop receptor structure and function. *Nature 440*, 448-455.
4. Lester, H. A., Dibas, M. I., Dahan, D. S., Leite, J. F., and Dougherty, D. A. (2004) Cys-loop receptors: new twists and turns. *Trends Neurosci. 27*, 329-336.
5. Zacharias, N., and Dougherty, D. A. (2002) Cation-pi interactions in ligand recognition and catalysis. *Trends Pharmacol. Sci. 23*, 281-287.
6. Arias, H. R. (2000) Localization of agonist and competitive antagonist binding sites on nicotinic acetylcholine receptors. *Neurochem. Internat. 36*, 595-645.
7. Unwin, N. (2005) Refined structure of the nicotinic acetylcholine receptor at 4A resolution. *J. Mol. Biol. 346*, 967-989.
8. Brejc, K., van Dijk, W. J., Klaassen, R. V., Schuurmans, M., van Der Oost, J., Smit, A. B., and Sixma, T. K. (2001) Crystal structure of an ACh-binding protein reveals the ligand-binding domain of nicotinic receptors. *Nature 411*, 269-276.
9. Hansen, S. B., Sulzenbacher, G., Huxford, T., Marchot, P., Taylor, P., and Bourne, Y. (2005) Structures of Aplysia AChBP complexes with nicotinic agonists and antagonists reveal distinctive binding interfaces and conformations. *EMBO J. 24*, 3635-3646.
10. Sine, S. M., Claudio, T., and Sigworth, F. J. (1990) Activation of Torpedo acetylcholine receptors expressed in mouse fibroblasts. Single channel current kinetics reveal distinct agonist binding affinities. *J. Gen. Physiol. 96*, 395-437.
11. Salamone, F. N., Zhou, M., and Auerbach, A. (1999) A re-examination of adult mouse nicotinic acetylcholine receptor channel activation kinetics. *J. Physiol. 516*, 315-330.
12. Sine, S. M., Ohno, K., Bouzat, C., Auerbach, A., Milone, M., Pruitt, J. N., and Engel, A. G. (1995) Mutation of the acetylcholine receptor alpha subunit causes a slow-channel myasthenic syndrome by enhancing agonist binding affinity. *Neuron 15*, 229-239.
13. Blount, P., and Merlie, J. P. (1989) Molecular basis of the two nonequivalent ligand binding sites of the muscle nicotinic acetylcholine receptor. *Neuron 3*, 349-357.
14. Blount, P., and Merlie, J. P. (1991) Characterization of an adult muscle acetylcholine receptor subunit by expression in fibroblasts. *J. Biol. Chem. 266*, 14692-14696.
15. Molles, B. E., Tsigelny, I., Nguyen, P. D., Gao, S. X., Sine, S. M., and Taylor, P. (2002) Residues in the epsilon subunit of the nicotinic acetylcholine receptor interact to confer selectivity of waglerin-1 for the alpha-epsilon subunit interface site. *Biochemistry 41*, 7895-7906.
16. Martinez, K. L., Corringer, P. J., Edelstein, S. J., Changeux, J. P., and Merola, F. (2000) Structural differences in the two agonist binding sites of the Torpedo nicotinic acetylcholine receptor revealed by time-resolved fluorescence spectroscopy. *Biochemistry 39*, 6979-6990.

17. Andreeva, I. E., Nirthanan, S., Cohen, J. B., and Pedersen, S. E. (2006) Site specificity of agonist-induced opening and desensitization of the Torpedo californica nicotinic acetylcholine receptor. *Biochemistry 45*, 195-204.
18. Unwin, N. (1995) Acetylcholine receptor channel imaged in the open state. *Nature 373*, 37-43.
19. Grosman, C., and Auerbach, A. (2001) The dissociation of acetylcholine from open nicotinic receptor channels. *Proc. Natl. Acad. Sci. U.S.A. 98*, 14102-14107.
20. Purohit, P., Mitra, A., and Auerbach, A. (2007) A stepwise mechanism for acetylcholine receptor channel gating. *Nature 446*, 930-933.
21. Purohit, Y., and Grosman, C. (2006) Block of muscle nicotinic receptors by choline suggests that the activation and desensitization gates act as distinct molecular entities. *J. Gen. Physiol. 127*, 703-717.
22. Grosman, C., and Auerbach, A. (2000) Asymmetric and independent contribution of the second transmembrane segment 12 ' residues to diliganded gating of acetylcholine receptor channels - A single-channel study with choline as the agonist. *J.Gen. Physiol. 115*, 637-651.
23. Grosman, C., Zhou, M., and Auerbach, A. (2000) Mapping the conformational wave of acetylcholine receptor channel gating. *Nature 403*, 773-776.
24. Zhou, M., Engel, A. G., and Auerbach, A. (1999) Serum choline activates mutant acetylcholine receptors that cause slow channel congenital myasthenic syndromes. *Proc. Natl. Acad. Sci. U.S.A. 96*, 10466-10471.
25. Colquhoun, D., and Sakmann, B. (1985) Fast events in single-channel currents activated by acetylcholine and its analogues at the frog muscle end-plate. *J. Physiol. 369*, 501-557.
26. Sine, S. M. (1993) Molecular dissection of subunit interfaces in the acetylcholine receptor: identification of residues that determine curare selectivity. *Proc. Natl. Acad. Sci. U.S.A. 90*, 9436-9440.
27. Hamill, O. P., Marty, A., Neher, E., Sakmann, B., and Sigworth, F. J. (1981) Improved patch-clamp techniques for high-resolution current recording from cells and cell-free membrane patches. *Pflug. Arch. 391*, 85-100.
28. Sakmann, B., and Neher, E. (1995) *Single-channel recording*, 2nd ed., Plenum Press, New York.
29. Qin, F. (2004) Restoration of single-channel currents using the segmental k-means method based on hidden Markov modeling. *Biophys. J. 86*, 1488-1501.
30. Qin, F., Auerbach, A., and Sachs, F. (1997) Maximum likelihood estimation of aggregated Markov processes. *Proceedings 264*, 375-383.
31. Qin, F., Auerbach, A., and Sachs, F. (1996) Estimating single-channel kinetic parameters from idealized patch-clamp data containing missed events. *Biophys. J. 70*, 264-280.
32. Qin, F., and Li, L. (2004) Model-based fitting of single-channel dwell-time distributions. *Biophys. J. 87*, 1657-1671.
33. Auerbach, A., and Lingle, C. J. (1986) Heterogeneous kinetic properties of acetylcholine receptor channels in Xenopus myocytes. *J. Physiol. 378*, 119-140.
34. Wang, H. L., Auerbach, A., Bren, N., Ohno, K., Engel, A. G., and Sine, S. M. (1997) Mutation in the M1 domain of the acetylcholine receptor alpha subunit decreases the rate of agonist dissociation. *J. Gen. Physiol. 109*, 757-766.
35. Hatton, C. J., Shelley, C., Brydson, M., Beeson, D., and Colquhoun, D. (2003) Properties of the human muscle nicotinic receptor, and of the slow-channel myasthenic syndrome mutant epsilonL221F, inferred from maximum likelihood fits. *J. Physiol. 547*, 729-760.

36. Akk, G., Zhou, M., and Auerbach, A. (1999) A mutational analysis of the acetylcholine receptor channel transmitter binding site. *Biophys. J. 76*, 207-218.
37. Akk, G., and Auerbach, A. (1999) Activation of muscle nicotinic acetylcholine receptor channels by nicotinic and muscarinic agonists. *Brit. J. Pharmacol. 128*, 1467-1476.
38. Akk, G., Sine, S., and Auerbach, A. (1996) Binding sites contribute unequally to the gating of mouse nicotinic alpha D200N acetylcholine receptors. *J. Physiol. 496*, 185-196.
39. Grosman, C., and Auerbach, A. (2000) Asymmetric and independent contribution of the second transmembrane segment 12' residues to diliganded gating of acetylcholine receptor channels: a single-channel study with choline as the agonist. *J. Gen. Physiol. 115*, 637-651.
40. Cadugan, D. J., and Auerbach, A. (2007) Conformational dynamics of the alphaM3 transmembrane helix during acetylcholine receptor channel gating. *Biophys. J. 93*, 859-865.
41. Mitra, A., Bailey, T. D., and Auerbach, A. L. (2004) Structural dynamics of the M4 transmembrane segment during acetylcholine receptor gating. *Structure 12*, 1909-1918.
42. Mitra, A., Cymes, G. D., and Auerbach, A. (2005) Dynamics of the acetylcholine receptor pore at the gating transition state. *Proc. Natl. Acad. Sci. U.S.A. 102*, 15069-15074.
43. Auerbach, A. (2007) How to turn the reaction coordinate into time. *J. Gen. Physiol. 130*, 543-546.
44. Milone, M., Wang, H. L., Ohno, K., Fukudome, T., Pruitt, J. N., Bren, N., Sine, S. M., and Engel, A. G. (1997) Slow-channel myasthenic syndrome caused by enhanced activation, desensitization, and agonist binding affinity attributable to mutation in the M2 domain of the acetylcholine receptor alpha subunit. *J. Neurosci. 17*, 5651-5665.
45. Auerbach, A. (1993) A statistical analysis of acetylcholine receptor activation in Xenopus myocytes: stepwise versus concerted models of gating. *J. Physiol. 461*, 339-378.
46. Auerbach, A., and Akk, G. (1998) Desensitization of mouse nicotinic acetylcholine receptor channels. A two-gate mechanism *J. Gen. Physiol. 112*, 181-197.
47. Elenes, S., and Auerbach, A. (2002) Desensitization of diliganded mouse muscle nicotinic acetylcholine receptor channels *J. Physiol. 541*, 367-383.
48. Schwarz, G. (1978) Estimating Dimension of a Model. *Ann. Stat. 6*, 461-464.
49. Prince, R. J., Pennington, R. A., and Sine, S. M. (2002) Mechanism of tacrine block at adult human muscle nicotinic acetylcholine receptors. *J. Gen. Physiol. 120*, 369-393.
50. Karlin, A. (2002) Emerging structure of the nicotinic acetylcholine receptors. *Nat. Rev. Neurosci. 3*, 102-114.
51. Prince, R. J., and Sine, S. M. (1996) Molecular dissection of subunit interfaces in the acetylcholine receptor. Identification of residues that determine agonist selectivity. *J. Biol. Chem. 271*, 25770-25777.
52. Celie, P. H., van Rossum-Fikkert, S. E., van Dijk, W. J., Brejc, K., Smit, A. B., and Sixma, T. K. (2004) Nicotine and carbamylcholine binding to nicotinic acetylcholine receptors as studied in AChBP crystal structures. *Neuron 41*, 907-914.
53. Stewart, D. S., Chiara, D. C., and Cohen, J. B. (2006) Mapping the structural requirements for nicotinic acetylcholine receptor activation by using tethered alkyltrimethylammonium agonists and antagonists. *Biochemistry 45*, 10641-10653.
54. Jackson, M. B. (1989) Perfection of a synaptic receptor: kinetics and energetics of the acetylcholine receptor. *Proc. Natl. Acad. Sci. U.S.A. 86*, 2199-2203.
55. Engel, A. G., Ohno, K., and Sine, S. M. (2003) Sleuthing molecular targets for neurological diseases at the neuromuscular junction. *Nat. Rev. Neurosci. 4*, 339-352.

56. Engel, A. G., Ohno, K., Milone, M., Wang, H. L., Nakano, S., Bouzat, C., Pruitt, J. N., 2nd, Hutchinson, D. O., Brengman, J. M., Bren, N., Sieb, J. P., and Sine, S. M. (1996) New mutations in acetylcholine receptor subunit genes reveal heterogeneity in the slow-channel congenital myasthenic syndrome. *Hum. Mol. Genet. 5*, 1217-1227.

Table III.1 Maximum Likelihood Rate Estimation of Hybrid Activity

	Θ_2	β_2 (s^{-1})	α_2 (s^{-1})
Wild-type	0.15 ± 0.01	130 ± 40	900 ± 300
Hybrid	0.46 ± 0.04	250 ± 60	500 ± 100
Hybrid	1.1 ± 0.1	500 ± 100	500 ± 100
Mutant	2.8 ± 0.2	1300 ± 400	500 ± 200

Table III.1. Maximum-likelihood fitting of single-channel activity recorded at 20 mM choline. Diliganded rate constants β_2 and α_2 are in s^{-1} and gating equilibrium constants Θ_2 are unitless. Mean ± standard error, 4 patches.

Table III.2 Maximum Interval Likelihood Rate Estimation

Equivalent Binding Sites		Non-Equivalent Binding Sites	
k_-	1140000 ± 20000	k_-^L	2090000 ± 30000
k_+	1790 ± 20	k_+^L	5900 ± 100
		k_+^H	26000 ± 600
		k_-^H	9.3 ± 0.2
β_1	346 ± 4	β_1^L	524 ± 6
α_1	1900 ± 400*	α_1^L	1900 ± 400*
		β_1^H	50 ± 1
		α_1^H	1900 ± 400*
β_2	2200 ± 700*	β_2	2200 ± 700*
α_2	1300 ± 100*	α_2	1300 ± 100*
K_D	1560 ± 30	K_D^L	2820 ± 60
		K_D^H	360 ± 10
Θ_1	0.18 ± 0.04	Θ_1^L	0.28 ± 0.06
		Θ_1^H	0.026 ± 0.006
Θ_2	1.7 ± 0.6	Θ_2	1.7 ± 0.6
LL	2543496	LL	2562125
	Events		482898
	Clusters		9003

Table III.2. Rate estimates obtained from maximum-likelihood fitting of Schemes III.1 and III.2. Association rate constants are in $M^{-1}\cdot s^{-1}$, and all other rate constants are s^{-1}. Dissociation constants are in μM, and equilibrium gating constants are unitless. Standard errors are fitting error estimates given by the QuB fitting software. *These rates were fixed according to estimates explained in the **Results** section.

Table III.3 Simulation: Symmetric Model Rate Constants			
	Wildtype	Hybrid	Mutant
k_{+1}	1.29E+08	1.29E+08	1.16E+08
k_{-1}	21900	21900	1890
k_{+2}	-	1.16E+08	-
k_{-2}	-	1890	-
β_2	48900	39185	31400
α_2	1660	1204	873
$k_{+desensitize}$	30	30	30
$k_{-desensitize}$	0.01	0.01	0.01

Table III.3. Previously reported rate constants used for simulating activity of wildtype, hybrid, and mutant channel activity for the αN217K slow-channel mutant (*34*). Association rates are in $M^{-1}\cdot s^{-1}$, and all other rates are in s^{-1}.

Table III.4 Simulation: Asymmetric Model Rate Constants				
	Wildtype	Hybrid (High Affinity)	Hybrid (Low Affinity)	Mutant
k_{+1}	8.40E+07	7.88E+08	8.40E+07	7.88E+08
k_{-1}	210	1267	210	1267
k_{+2}	1.80E+07	1.80E+07	9.50E+07	9.50E+07
k_{-2}	16457	16457	970	970
β_2	60000	50000	50000	44965
α_2	2288	1500	1500	883
$k_{+desensitize}$	30	30	30	30
$k_{-desensitize}$	0.01	0.01	0.01	0.01

Table III.4. Previously reported rate constants used for simulating activity of wildtype, hybrid, and mutant channel activity for the αG153S slow-channel mutant (*12*). Association rates are in $M^{-1}\cdot s^{-1}$, and all other rates are in s^{-1}. Parentheses indicate which agonist binding site is mutated.

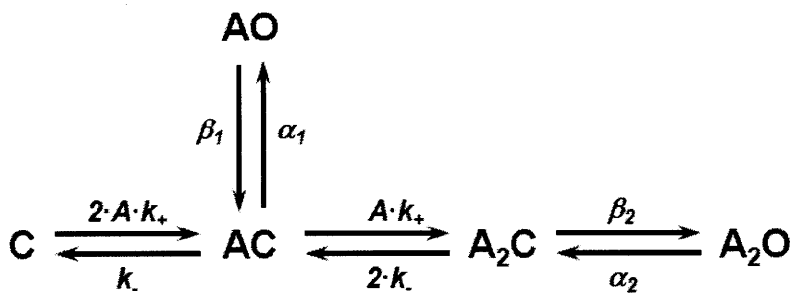

Scheme III.1. AChR kinetic model with identical binding sites. Closed-state agonist association and dissociation are identical at both binding sites. Kinetic states: "C", closed; "O", open; "A" represents bound agonist. Rate constants are in s^{-1} except where noted: β_1, monoliganded opening; β_2, diliganded opening; α_1, monoliganded closing; α_2 diliganded closing; k_+, agonist association ($M^{-1} \cdot s^{-1}$); k_, agonist dissociation.

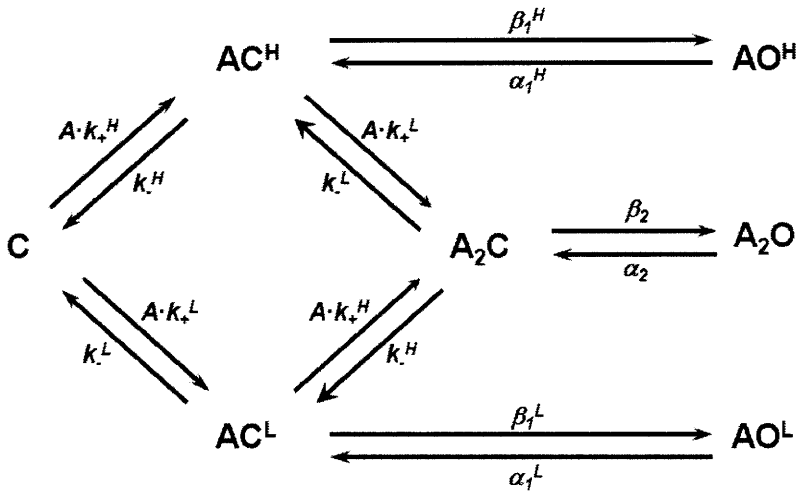

Scheme III.2. AChR kinetic model with potentially non-identical binding sites. Closed-state agonist association and dissociation are not constrained to be identical at both binding sites. This model is more general than Scheme III.1. Note that the closed-state kinetics and affinities are not required to be different, they are simply allowed to be different. Kinetic states and rate constants are labeled as in Scheme III.1. Low and high affinity sites and associated rate constants are denoted by superscript "L" and "H", respectively.

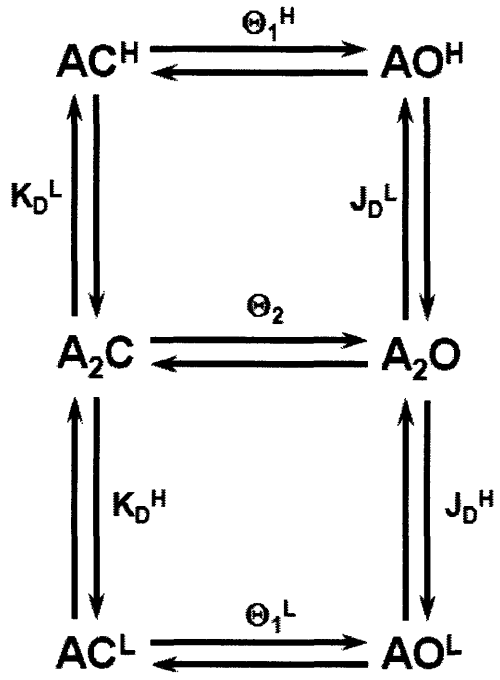

Scheme III.3. AChR conformational model showing thermodynamic loops that obey detailed balance. J_D^H and J_D^L are the open-state agonist dissociation constants. Derived loop balance equations: outer loop, $K_D^L \cdot \Theta_1^H \cdot J_D^H = K_D^H \cdot \Theta_1^L \cdot J_D^L$; top loop, $J_D^L \cdot \Theta_2 = K_D^L \cdot \Theta_1^H$; bottom loop, $J_D^H \cdot \Theta_2 = K_D^H \cdot \Theta_1^L$.

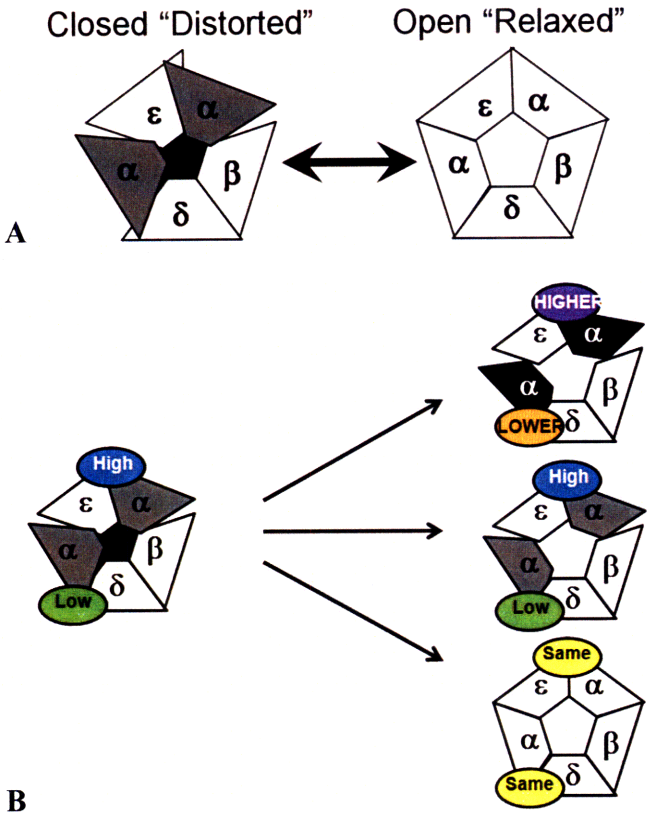

Figure III.1. AChR symmetry. (A) A simplified representation of the change in structural symmetry as proposed from structural data. (B) Representation of the hypothesis tested in this work with transmitter binding sites represented as ovals. The AChR has non-equivalent closed-state affinities represented by the ovals labeled "High" and "Low". Upon gating, there are three predicted outcomes: top, the open-state affinities become more different represented by the ovals labeled "Higher" and "Lower"; middle, the open-state affinities increase or decrease equivalently; bottom, the open-state affinities can become equivalent represented by the ovals labeled "Same".

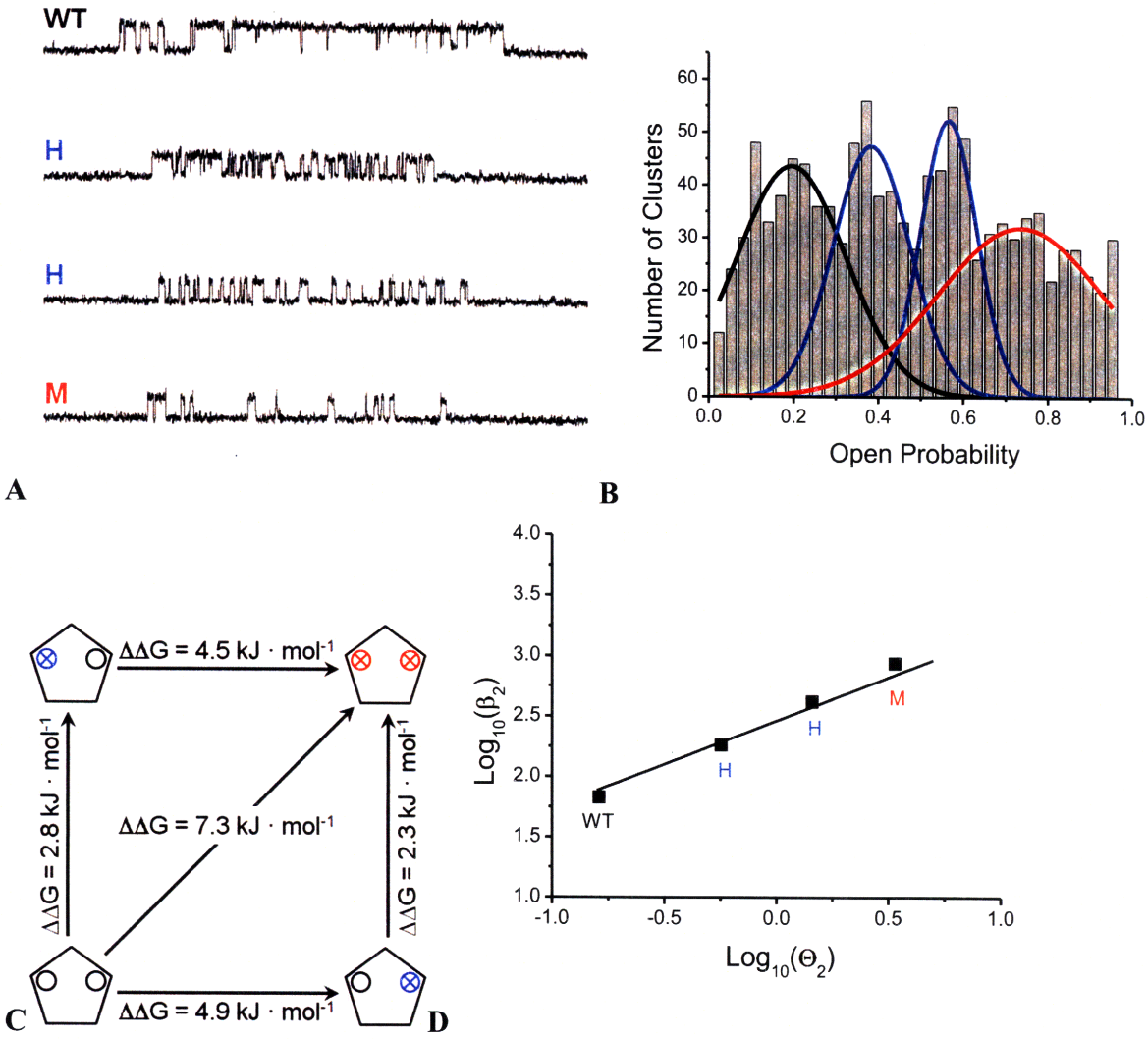

Figure III.2. Hybrid activity from mixtures of wild-type and the G153S mutant α-subunits. (A) Example clusters of the four modes of activity from wild-type (WT), hybrid (H), and mutant (M) channels elicited at saturating 20 mM choline. (B) Example of four modes of activity shown in a histogram of intracluster open probabilities from one patch. A segmental k-means algorithm was used to fit four Gaussian curves to the wild-type (black), hybrid (blue), and mutant (red) open probabilities. (C) Mutant cycle analysis shows the αG153S mutations at the two binding sites are independent. (D) An example of a REFER plot from the activity of one patch with a Φ-value of approximately 0.8.

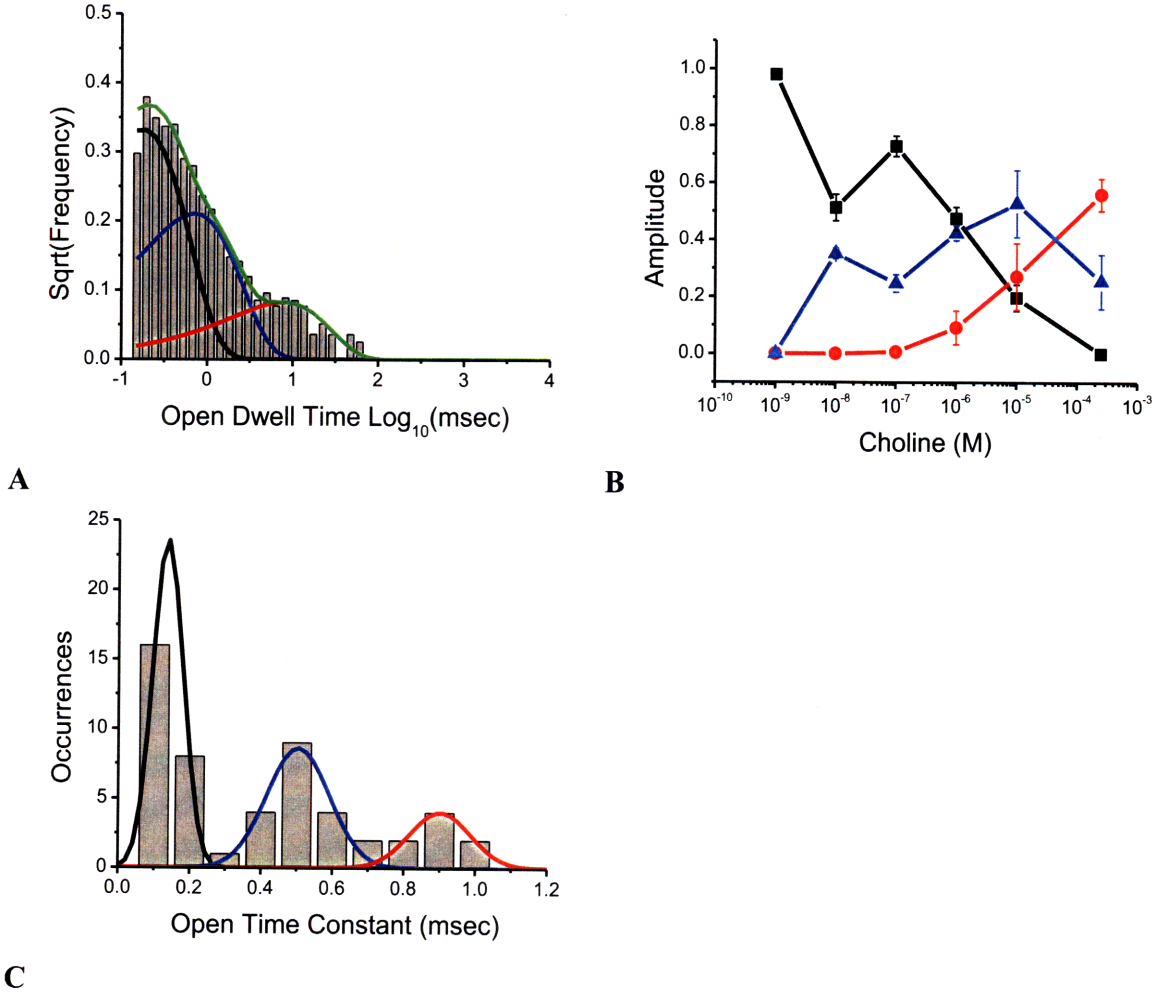

Figure III.3. Estimation of channel closing rate constants at low choline concentrations for the αG153S mutant. (A) An example open dwell-time distribution obtained at 100 nM choline. The distribution was best fit by three exponential components, also referred to as time constants. (B) Concentration dependence of the amplitudes for time constants assigned to unliganded (black squares), monoliganded (blue triangles), and diliganded (red circles) openings. (C) A histogram of observed open time constants shows three distinct peaks assigned to unliganded (black), monoliganded (blue), and diliganded (red) openings.

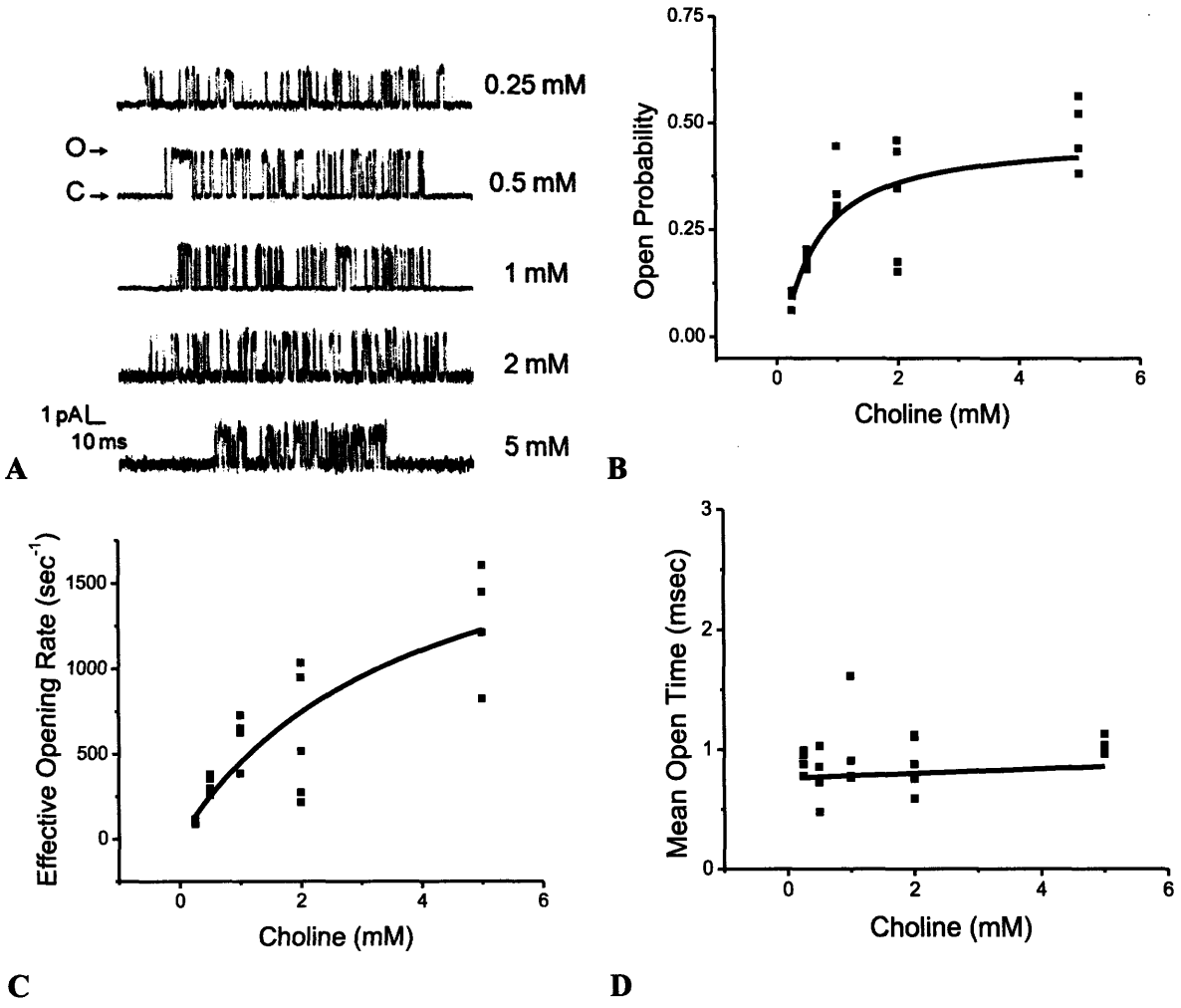

Figure III.4. Estimation of diliganded channel gating at high choline concentrations for the αG153S AChR. (A) Examples of single-channel clusters recorded at 0.25, 0.5, 1, 2, and 5 mM choline, shown at 10 kHz filtering with open events shown as upward deflections. (B) The intracluster open probability concentration dependence was fit (solid line) to a Hill equation: EC_{50} = 1.2 ± 0.4 mM and P_{open}^{max} = 0.6 ± 0.3. (C) From fitting (solid line) the concentration dependence of the effective opening rate, β_2 = 2200 ± 700 s^{-1}. (D) From a linear fit (solid line) of the concentration dependence of intracluster mean open time, α_2 = 1300 ± 100 s^{-1} and K_{block} ~ 10^{-2} M^{-1}.

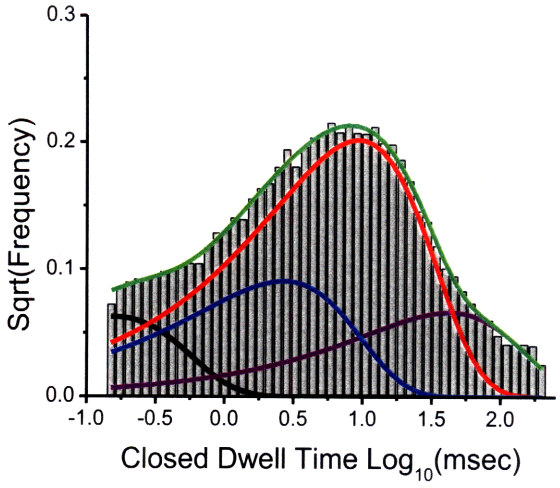

Figure III.5. Closed dwell-time distributions at 0.25 mM choline were best fit by four closed components (black, blue, red, purple) suggesting that two distinct binding events are detectable. Fitting to 4 closed components versus 3 was statistically better, but fitting to 5 components versus 4 was not. The superposition of all calculated distributions is shown in green.

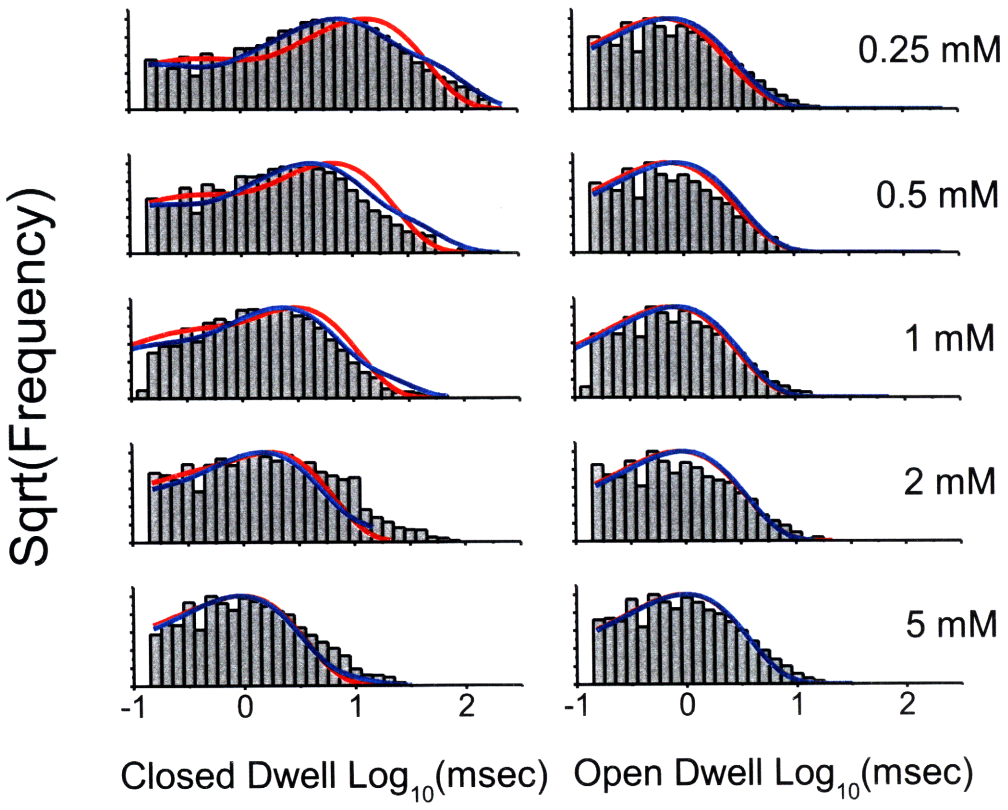

Figure III.6. Intracluster closed (left) and open (right) dwell-time distributions at 0.25, 0.5, 1, 2, and 5 mM choline. Maximum-interval likelihood was used to fit the data to Scheme III.1 (red) versus Scheme III.2 (blue). Scheme III.2 was a statistically better model.

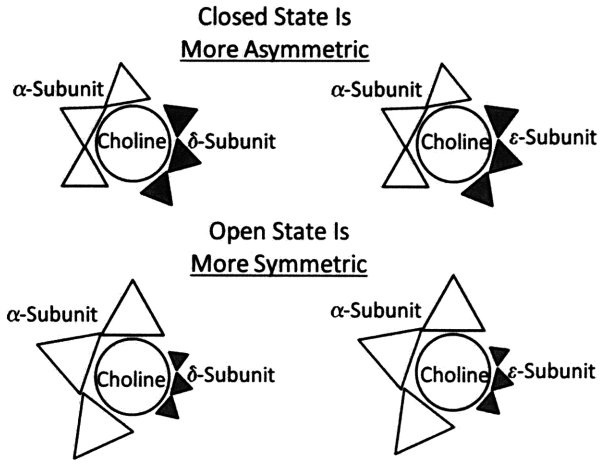

Figure III.7. Fractional contributions of the principal (unfilled triangles) and complementary faces (shaded triangles) change with gating. In the closed state, TBSs' affinities differ because interactions with the complementary faces are significant. In the open state, the TBSs' affinities are equal because the principal face is largely responsible for open-state binding.

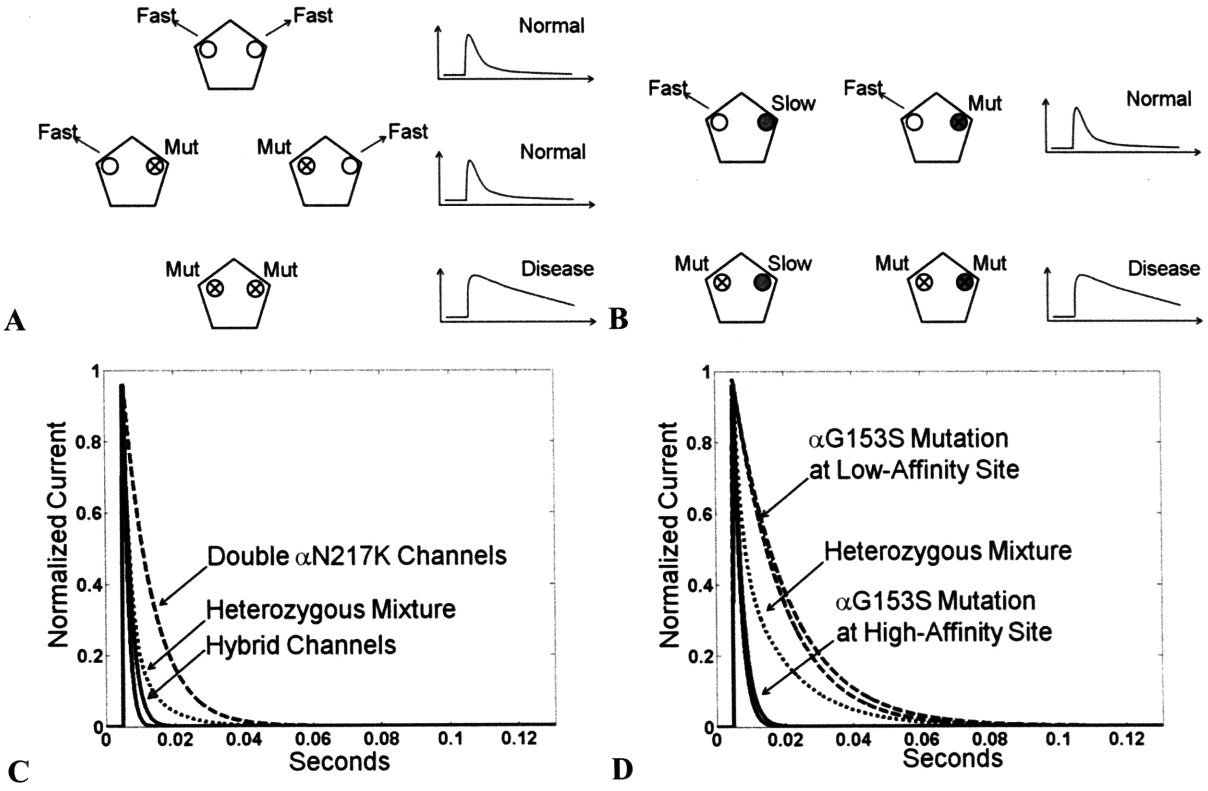

Figure III.8. Kinetic symmetry considerations may be useful in understanding slow-channel congenital myasthenic syndromes. (A) Identical closed-state binding sites (Scheme III.1) suggests the disease is more likely recessive. Left: pentagon, AChR; open circle, wild-type TBS; crossed circle, SCCMS mutant TBS. Top right: predicted wild-type synaptic current. Middle right: predicted heterozygous current. Bottom right: predicted homozygous SCCMS current. (B) Non-equivalent closed-state binding sites (Scheme III.2) suggests the disease is more likely dominant. (C) Deterministic simulation of the αN217K SCCMS mutant using literature-reported rate constants quantitatively predicts a recessive phenotype, but clinically the associated disease is dominant. Only the homozygous SCCMS simulated current (dashed line) is significantly slowed in decay time. (D) Deterministic simulation of the αG153S SCCMS mutant using literature-reported rate constants quantitatively predicts a dominant phenotype, correlating with clinical observation that the associated disease is dominant. Both the homozygous (dashed line) and heterozygous (dotted line) are significantly slowed in decay time.

Chapter IV.

Development of a Trifunctional Probe Suitable for Activity-Dependent Protein Profiling of the Acetylcholine Receptor

IV.A Summary

Activity-based protein profiling (ABPP) has been used extensively to characterize enzymes involved in cellular signaling pathways, but its use has not yet been extended to ion channels. We have synthesized a state-dependent photoaffinity probe for the nicotinic acetylcholine receptor (nAChR) as a proof of concept that ABPP can be applied to ion channels. The candidate probe named BPyneTEA comprises nAChR binding functionality, a benzophenone group for photolabeling, and an alkyne group for biotinylation via "click chemistry", permitting selective purification. Electrophysiological measurements at the single-molecule level show that BPyneTEA blocks both the closed and open states of receptor with similar affinity and kinetics. Covalent photolabeling studies indicate that BPyneTEA labels the activatable closed state selectively over the inactive desensitized state. Thus, BPyneTEA shows promise as a probe for non-desensitized nAChRs, and may be useful in studying the physiological roles of nAChR desensitization in addiction and neuromuscular disorders. The results suggest that ion channel pores, like enzyme active sites, will be a broadly useful target for ABPP probes.

IV.B Introduction

Activity-based protein profiling (ABPP) is rapidly becoming one of the essential experimental approaches in understanding biological processes at the systems level (*1*). The ABPP approach involves the use of chemical reagents that selectively target an active state of a protein. It provides a direct method for interrogating signaling processes that involve activation or inactivation of an already-expressed protein. Because of the importance of such processes in biology (e.g., cascades of protease or kinase activation), ABPP has proven to be useful in a broad range of biological applications (*2-4*). ABPP reagents have been prepared for a number of important enzyme classes, including serine proteases (*5*), kinases (*6*), and histone deacetylases (*7*), and the strategy is likely to be useful for many additional classes of enzyme active sites.

Ion channels are one important class of proteins for which ABPP probes have not been previously reported. Although ion channels typically do not incorporate enzyme active sites, they exist in different conformations with different associated activities. A probe molecule that selectively labels a subset of the different activation states of the channel could thus be used as an activity-based probe. Activation and deactivation of ion channels are central to some of the most important processes in neurobiology, such as neuronal excitability and synaptic plasticity (*8*). Development of ABPP probes for ion channels would therefore have the potential to provide useful tools for the study of neurobiology at the systems level.

An affinity reagent that both reacts differentially with an ion channel in different conformational states and contains a bioorthogonal reactive group (e.g., azide or alkyne) for affinity labeling and purification (*9*) would allow ABPP studies of the target channel. Reagents with a subset of these features have been developed, but channel-directed ABPP probes with all of the required functionality have not yet been reported. Many ion channel inhibitors exhibit a pronounced binding preference for closed or open conformations of the target channel (*10-13*). A photoactivated state-dependent inhibitor of AMPA receptors (*14*) has proven to be a valuable tool for measurements of AMPA receptor trafficking in neurons, but similar compounds that allow isolation and detection of the inactivated receptors are not yet available.

The nicotinic acetylcholine receptor (nAChR) is an ion channel in the Cys-Loop family that becomes cation-permeable upon binding the neurotransmitter acetylcholine. The state-dependent pharmacology of nAChR blockers has been used to design chemical probes that bind selectively to different activation states of the channel, allowing differential covalent labeling (*15-18*). However, probes suitable for proteomic applications have not yet been characterized. A channel-selective photoaffinity probe containing a biotin group has been synthesized (*19*), but its ability to mediate state-dependent labeling has not been tested.

Because the nAChR exhibits dramatic changes in pore structure on switching from active to inactive states, this channel is a promising target for the design of a channel-directed ABPP probe. Like other neurotransmitter-gated channels, nAChRs typically undergo desensitization: a transition into a long-lived inactive state in response to prolonged exposure to acetylcholine (*20, 21*). In contrast to closed states of nAChRs which predominate in the absence of neurotransmitter, desensitized states typically have very high affinities for acetylcholine and nicotine (*22-25*) and predominate in the presence of neurotransmitter. Site-directed cysteine

accessibility experiments suggest that desensitization involves a collapse of the intracellular end of the ion permeation pore (*26*). As often observed in ion channel permeation pores (*27*), the nAChR pore contains charged and hydrophilic functional groups for cation solvation as well as hydrophobic pore-lining regions (*28, 29*). Collapse of the pore on desensitization might therefore have a substantial effect on the binding of a charged and/or hydrophobic probe molecule, allowing ABPP studies of closed, activatable versus desensitized nAChRs in vivo.

ABPP probes for nicotinic acetylcholine receptors (nAChRs) might be used to help characterize the roles that desensitization and re-activation of these receptors play in neuronal excitability and the pathogenesis of neuromuscular disorders. For example, nicotine, an nAChR agonist, is present at desensitizing concentrations in the serum of tobacco smokers, and nAChR activation (*30, 31*) and desensitization (*21, 32*) in reward-sensing areas of the brain have been implicated in tobacco addiction. Similarly, altered desensitization of the muscle-type nAChR has recently been proposed to contribute to the impaired neuromuscular transmission that causes muscle weakness in patients with slow-channel myasthenic syndromes (*33*). Using selective labeling of non-desensitized receptors, non-desensitized and desensitized receptors could be separately isolated with their associated proteins. Post-translational modifications and protein-protein interactions in non-desensitized and desensitized receptor populations could then be compared. We demonstrate in this work that this goal is achievable by developing a probe that preferentially photolabels non-desensitized nAChRs.

We synthesized a candidate ABPP probe for state-dependent binding and photolabeling of nAChRs. The candidate probe, known as BPyneTEA (benzophenone-alkyne-triethylammonium), contains a terminal alkyne moiety, permitting bioorthogonal conjugation to azide-functionalized biotin (*34*), and an core benzophenone, permitting covalent photolabeling (**Figure IV.1**) (*35*). Benzophenone itself has previously been shown to act as a weak blocker and to exhibit state-dependent nAChR covalent labeling, selectively labeling the closed channel in the M2 pore-lining segment (*36*). BPyneTEA also includes a terminal triethylammonium (TEA) group to direct the probe to the ion permeation pore and decrease membrane permeability. Tetraalkylammoniums are known nAChR open pore blockers (*37*), and attaching TEA to the BPyne core provides additional structural similarity to the local anesthetic and open-pore blocker QX-314 (N-ethyl lidocaine) (*11*). Because our candidate probe combines features of several "parent" state-selective structures, we characterized its action on nAChRs both

electrophysiologically and biochemically to assess the effect of combining these features in a single structure. Electrophysiological characterization of this candidate probe at the single-molecule level indicates that it binds both the closed and open states of the nAChR, suggesting that the probe exhibits some of the binding properties of the parent structures. Use of the candidate probe to photolabel nAChRs in living cells shows that covalent labeling is selective for closed over desensitized channels. These results demonstrate that the probe is suitable as an ABPP reagent, and that ABPP is amenable for application to ion channels, where the ion conducting pore may act as a reactive site analogously to an enzyme active site.

IV.C Materials and Methods

BPyneTEA was synthesized by Wan-Chen Lin as a part of her doctoral thesis. Cell culture, electrophysiology, and single-channel analysis were carried out using the same methods described in **Chapter II**.

Synthesis of the Biotin-Azide Reagent

To a cooled (0 °C) mixture of biotin (122 mg, 0.5 mmol), *N*-ethyl-*N'*-(3-dimethyl-aminopropyl)carbodiimide hydrochloride (EDC, 144 mg, 0.75 mmol), and HOBT (101 mg, 0.75 mmol) in anhydrous DMF (5 mL) was added 1-amino-11-azido-3,6,9-trioxaundecane (55 mg, 0.25 mmol, diluted in 1 mL of anhydrous DMF) dropwise. The reaction mixture was stirred at 0 °C for 0.5 h and was then allowed to warm to ambient temperature. The mixture was stirred at room temperature for 24 h, concentrated by rotary evaporation, and then diluted with MeOH/$CHCl_3$ (5:95, 15 mL). The organic phase was washed with 1 N HCl (aq) (5 × 10 mL); the resulting aqueous phase was neutralized with saturated $NaHCO_3$ (aq) (3 × 10 mL), and re-extracted with $CHCl_3$ (5 × 10 mL). The combined organic phases was washed with brine (5 × 10 mL saturated sodium chloride aqueous solution), dried over anhydrous Na_2SO_4, concentrated by rotary evaporation, and purified by silica gel chromatography ($CHCl_3$ → 17:83 MeOH:$CHCl_3$) to give biotin-N_3 (101 mg, 91%) as a white solid. TLC (1:5 MeOH:$CHCl_3$) R_f 0.40; ^{1}H NMR (CD_3OD, 300 MHz): δ 4.50 (m, 1H), 4.31 (dd, J = 8.0, 4.4 Hz, 1H), 3.72–3.58 (m, 10H), 3.54 (t, J = 5.4 Hz, 2H), 3.46–3.32 (m, 4H), 3.21 (m, 1H), 2.93 (dd, J = 12.6, 5.0 Hz, 1H), 2.71 (d, J = 12.6 Hz, 1H), 2.22 (t, J = 7.4 Hz, 2H), 1.80–1.54 (m, 4H), 1.52–1.48 (m, 2H); ^{13}C NMR (CD_3OD, 75 MHz): δ 176.2, 166.2, 71.8 (2 peaks), 71.7, 71.4, 71.3, 70.7, 63.5, 61.8, 57.2, 51.9,

41.2, 40.5, 36.9, 29.9, 29.6, 27.0; HRMS–ESI (*m/z*) calcd for $C_{18}H_{32}N_6NaO_5S$ $[M + Na]^+$: 467.2047; found: 467.2045. NMR spectra were obtained by Mathew Tantama and interpreted by Wan-Chen Lin. MS was obtained by Wan-Chen Lin.

Electrophysiology

HEK 293 cells were transiently transfected with a 2:1:1:1 mass ratio of adult mouse muscle α, β, δ, and ε AChR cDNAs using the method of calcium phosphate precipitation (*22, 38*). Single-channel patch-clamp recordings were obtained in the cell-attached mode (*39*). The pipette and bath solutions were Dulbecco's phosphate buffered saline (DPBS, in mM): 137 NaCl, 2.7 KCl, 0.9 $CaCl_2$, 0.5 $MgCl_2$, 6.6 Na_2HPO_4, 1.5 KH_2PO_4, pH 7.3. For experiments at low acetylcholine concentration, 1 μM acetylcholine (serially diluted from a 1M stock) and varying amounts of BPyneTEA were included in the pipette solution from 0 to 500 μM concentrations. For experiments at high choline concentration, the α subunit contained the gain-of-function G153S mutation (*38, 40*), and the pipette solution included 1 mM choline and varying amounts of BPyneTEA. Single-channel currents were recorded with an Axopatch 200B (Axon Instruments, Foster City, CA) through a low-pass Bessel filter at 10 kHz, and data were digitized at a sampling rate of 20 kHz using a NI 6040 E Data Acquisition Board (National Instruments, Austin, TX). The membrane potential was usually -30 to -40 mV. For recordings at 1 mM choline, the command potential was held at -70 mV. To measure voltage dependence, the command potential was varied from 0 to 200 mV during recording. Single-channel currents were not observed in the presence of BPyneTEA and the absence of agonist.

Single-channel Analysis

The QuB software suite (www.qub.buffalo.edu) (*41-45*) was used to adjust for baseline drift, to idealize events, to analyze dwell-time distributions, and to determine clusters as in **Chapter II** (*43, 46, 47*). OriginLab (OriginLab Corporation, Northampton, MA) and Matlab (The Mathworks, Natick, MA) were also used for non-linear least squares fitting and figure preparation.

Analysis of Single-Channel Clusters

BPyneTEA exhibits the characteristics of a slow open-channel blocker. Open-channel blockers can be classified as fast, intermediate, or slow blockers according to the magnitude of their unblocking rate constants (with association rate constants typically $10^6 - 10^8$ $M^{-1} \cdot s^{-1}$). For fast blockers, the unblocking rate constant is fast compared to the sampling frequency of the recording, so that the mean residence time in the blocked state is short, even shorter than the time resolution of the experiment. As a result, when the channel opens, several blocking and unblocking events occur before the channel closes, leading to a net decrease in the observed open-channel current amplitude. BPyneTEA does not exhibit this phenotype. For intermediate blockers, the unblocking rate constant is of similar magnitude as channel opening and closing. As a result, when the channel opens, several blocking and unblocking events occur *and* are resolvable, causing a burst of shortened single-channel openings within the overall cluster of openings. However, BPyneTEA does not cause resolvable bursts within clusters of activity and does not exhibit this phenotype. Instead, BPyneTEA acts as a slow blocker.

For slow blockers, the unblocking rate constant is slow compared to channel opening, resulting in long sojourns in the closed blocked state that are indistinguishable from desensitized sojourns. As a result, an additional path is available to terminate clustered activity, resulting in shortening of clusters (**Scheme IV.1**). Because the probability of blockade is proportional to the time a channel spends open, longer open events are more likely to be blocked. This leads to a net decrease in the observed mean open time within a cluster, that is $\langle t_{open} \rangle = (\alpha + k_{+desensitize} + k_{+block}^{open} \cdot [blocker])^{-1} \sim (\alpha + k_{+block}^{open} \cdot [blocker])^{-1}$ since $k_{+desensitize} << \alpha$, where α is the channel closing rate constant, $k_{+desensitize}$ is the desensitization rate constant, k_{+block}^{open} is the rate constant for block (association of the blocker) to the open state.

The same argument can be applied to blockade of the closed state within in a cluster, and closed-state blockade leads to a net decrease in the closed time: $\langle t_{closed} \rangle = (\beta' + k_{+block}^{closed} \cdot [blocker])^{-1}$, where β' is the apparent opening rate constant, k_{+block}^{closed} is the rate constant for block (association of the blocker) to the closed state. In the case of closed-state blockade, a complication is introduced when dealing with clusters. Because clusters are defined by sojourns in the long-desensitized state, sojourns in a fast-desensitized or "gap" state, shorter-than-average sojourns in the long-desensitized state and shorter-than-average sojourns in the blocked state may contaminate the clusters. The closed time component which decreases in magnitude as

blocker concentration increases is therefore the closed component of interest for determining blockade rate constants.

Kinetic simulations illustrate how a blocker that binds to both the open and the closed states affects the open and closed time distributions. The following parameters were used for kinetic simulations: $k_{+block}^{closed} = 5 \times 10^6\ M^{-1}\ s^{-1}$, $k_{-block}^{closed} = 50\ s^{-1}$, $\beta = \alpha = 1000\ s^{-1}$, $k_{+block}^{open} = 1 \times 10^6\ M^{-1}\ s^{-1}$, $k_{-block}^{open} = 50\ s^{-1}$, $k_{+desensitize} = k_{-desensitize} = 100\ s^{-1}$. The results of the simulation show the decrease in both closed and open dwell times with increasing blocker concentration (**Figure IV.2**) and the appearance of a long-lived closed component.

As mentioned above, slow blockade terminates clustered single-channel activity early, but shorter-than-average sojourns in the blocked state may contaminate clusters. Therefore, the longest-lived closed component in clusters represents an underestimate of the actual blockade lifetime. Because the unblocking rate constant is inversely proportional to the mean blockade lifetime, the long-lived closed component provides an upper bound for the total unblocking rate constant, a function of unblocking rate constants for both the open and closed states. Ideally, this component would increase in amplitude as blocker concentration increases; however, because of the presence of contaminating desensitized sojourns this is likely not to be the case in practice with a limited sample of clusters. Still, this complication does not preclude estimation of an upper bound, with the caveat that, by definition, the upper bound may overestimate the true unblocking rate constant, leading to an upper bound for the blocking dissociation constant that overestimates the true dissociation constant. It might be possible to deconvolve the open-state and closed-state unblocking rate constants from dwell-time correlation analysis, but this would require a very large data set and is beyond the scope of the analysis performed in this work.

Analysis of Unclustered Single-Channel Activity and Voltage-Dependent Block

For a simple open-channel blockade model, the mean open time is inversely proportionally to the sum of rate constants leaving the open state (**Scheme IV.2**). We can write the mean open time as $\langle t_{open} \rangle = (\alpha + k_{+block} \cdot [blocker])^{-1}$. It has been shown previously that the closing rate constant (α) is voltage-dependent (*48*). The mean open time increases with hyperpolarization (the transmembrane voltage used in the current experiments range from 0 to -200 mV) according to the relationship $\alpha(V) = \alpha^0 \cdot \exp(z_\alpha \cdot \delta_\alpha \cdot F \cdot V/R \cdot T)$ where F is Faraday's

constant, R is the gas constant, T is the temperature, z is the gating charge, and δ is the electrical distance or the percent of the transmembrane electric field sensed by the gating charge.

For open-channel blockade by a charged group, the voltage dependence of the blockade association rate constant can be similarly described using the Woodhull model (*49*). In this analysis, we neglect permeation of the blocker as a rare event, meaning that increasing hyperpolarization increases blockade according to the relationship $k_{+block}(V) = k_{+block}^{0} \cdot \exp(-z_{block} \cdot \delta_{block} \cdot F \cdot V/RT)$. For BPyneTEA, $z_{block} = +1$. Hence, we can write $\langle t_{open} \rangle = [\alpha^{0} \cdot \exp(z_{\alpha} \cdot \delta_{\alpha} \cdot F \cdot V/R \cdot T) + k_{+block}^{0} \cdot \exp(-\delta_{block} \cdot F \cdot V/RT)]^{-1}$. From experiments at 1 μM acetylcholine using the wild-type receptor, we have a range of $\langle t_{open} \rangle$ as a function of concentration and voltage. Initial fitting of the 3-dimensional surface using non-linear least squares fitting in Matlab (The Mathworks, Natick, MA) did not lead to a stable solution. Therefore, we fit $\langle t_{open} \rangle$ as a function of [BPyneTEA] at each voltage, providing estimates of α and k_{+block} as a function of voltage. The voltage dependence was then fitted to the appropriate equations from the Woodhull model, providing estimates of the electrical distance, the fractional distance from the extracellular membrane face within the transmembrane electric field.

Photolabeling and Western Blotting

AChR-expressing HEK 293 cells were grown in 35 mm dishes. Cells were washed with DPBS prior to addition of 1 mL DPBS containing BPyneTEA with or without 0.2 μM acetylcholine. According to previously published protocols, cells were irradiated for 1 hour at 4°C at 365 nm wavelength using a UVL-56 (UVP) handheld lamp at a distance of 5 cm and intensity of 1350 $\mu W/cm^2$ (*34*). The labeling solution was removed, and cells were gently dissociated and collected in 2 mL DPBS. For each experimental condition, cells from four 35 mm dishes were typically pooled. Cells were pelleted for 10 minutes at 1000 x g, and the supernatant was aspirated. Cells were lysed for 3 hours with gentle agitation at 4°C in 500 μL lysis buffer (50 mM HEPES, pH 8, 150 mM NaCl, 1% Triton-X100, 1X Roche EDTA-free protease inhibitor cocktail) (*50*). Lysates were pelleted for 5 minutes at 10000 x g to remove insoluble material, and cleared lysates were split into equal aliquots.

As a control for variability in expression levels, solubilized receptors from one aliquot of cleared lysate were captured with α-bungarotoxin-functionalized Sepharose beads for 20 hours at 4°C. α-bungarotoxin (Biotium, Hayward, CA) was coupled to CNBr-activated Sepharose (GE

Healthcare, Piscataway, NJ) according to the manufacturer's instructions. Following capture, beads were washed with wash buffers containing 50 mM HEPES, pH 8, 1% Triton-X100, 0.1 mg/mL BSA and NaCl at increasing concentrations of 150, 250, 500, and 1000 mM. Beads were eluted with SDS loading buffer (*51*) for 1 hour at 25°C for SDS-PAGE and Western blotting.

To assess photolabeling, a second aliquot of cleared lysate was brought to 0.1% SDS, 5% t-butanol, 100 μM tris[(1-benzyl-1H-1,2,3-triazol-4-yl)methyl]amine (Sigma, St. Louis, MO), 1 mM tris-(2-carboxyethyl)phosphine, 100 μM biotin-azide reagent, 1 mM $CuSO_4$ and subjected to click chemistry conditions for 3 hours at 25°C with stirring (*52*). Following the click reaction, lysates were dialyzed in 4 liters of 50 mM HEPES, pH 8, 150 mM NaCl, 0.1% SDS, 1% Triton-X100 for 3 hours with one dialysis buffer change to remove excess biotin-azide reagent. Biotinylated, soluble receptors were then captured with streptavidin-functionalized agarose beads (Thermo Scientific, Rockford, IL) for 12 hours at 4°C. Following capture, beads were washed with wash buffers containing 50 mM HEPES, pH 8, 0.1% SDS, 1% Triton-X100, 0.1 mg/mL BSA and NaCl at increasing concentrations of 150, 250, 500, and 1000 mM. Beads were eluted with reducing SDS loading buffer (2% SDS) (*51*) for 20 minutes at 25°C followed by 5 minutes at 65°C, and the supernatant was removed while hot. Two additional elutions were carried out, and the eluates were pooled. Following SDS-PAGE of the pooled eluates on a 10% gel, protein was transferred to nitrocellulose, and protein transfer was quantified by reversible Ponceau S staining. The protein transfer to nitrocellulose was carried out in a Biorad tank transfer apparatus using transfer buffer consisting of 25 mM Tris, 192 mM Glycine, 0.1% SDS, 20% methanol in deionized water pre-chilled at 4°C. The gels were first equilibrated in transfer buffer for 30 minutes, and nitrocellulose membranes were equilibrated for 15 minutes, both at room temperature. Protein was then transferred for 50–60 minutes at 500 V, and the entire apparatus was placed in an ice-bath to reduce heating.

Western blotting was conducted at room temperature using a primary mouse anti-AChR α subunit antibody (Clone 26, BD Biosciences, San Jose, CA) at 1:250 dilution and a secondary horseradish peroxidase-conjugated goat anti-mouse antibody (BioRad, Hercules, CA) at 1:15000 dilution. Blots were blocked with 3% BSA in tris-buffered saline containing 0.1% Tween-20 (TBST) for 1 hour with agitation. Blots were incubated with primary antibody diluted in blocking solution for 1 hour with agitation. Blots were washed 3 x 10 minutes in 50 mL TBST. Blots were incubated with secondary antibody diluted in blocking solution for 1 hour with

agitation. Blots were washed 3 x 10 minutes in 50 mL TBST and then 1 x 5 minutes in 50 mL tris-buffered saline without detergent. SuperSignal West (Thermo Scientific) substrate was used for chemiluminescent detection. Blots were incubated in 7.5 mL substrate for 5 minutes, and then placed in plastic wrap for imaging. Blots were imaged, and densitometry was conducted using a CCD imaging system (Alpha Innotech, San Leandro, CA). Bands were background subtracted, and photolabeling levels were normalized for expression levels. To perform the background subtraction, the area of interest around a given band was defined and pixel density quantified. Then, an equal area of background immediately above and immediately below was quantified, the two background estimates averaged, and the background value subtracted from the band of interest. The background-subtracted band from the streptavidin eluate, representing the photolabeled protein, was normalized by dividing it by the background-subtracted expression-control band (**Figure IV.5**). For any given blot, 2 to 7 exposures were typically taken and densitometry conducted in order to assess the variability in quantification for a single blot.

IV.D Results

Electrophysiological Characterization: BPyneTEA Blocks Both the Closed and Open AChR

Patch-clamp recordings of individual ion channel openings allow measurement of state-dependent binding and blockade. Quaternary ammonium blockers such as tetraethylammonium and QX-314 often block nAChRs by binding the open pore. Small hydrophobic blockers such as benzophenone can bind the nAChR in the closed conformation (*53*), and, in fact, binding of benzophenone to the channel pore is highly selective for the closed nAChR over the desensitized nAChR (*36*). Since BPyneTEA incorporates both benzophenone and TEA/QX-314-like structural elements, it is likely that BPyneTEA can bind the nAChR pore in both the open and closed states.

Single channel patch-clamp current recordings were used to test the hypothesis that BPyneTEA can block both open and closed nAChRs. To ensure that both open and closed states were observable, single-channel currents were recorded from a gain-of-function nAChR mutant, αG153S (*40*), activated using the weak agonist choline. The combination of the gain-of-function mutation and the weak agonist extends both channel openings and channel closings, making them long-lived enough to be easily resolved (*54*). In addition, fast blockade by choline itself is negligible at the concentration of choline used here (1 mM) (*55*). Channel activity in the absence

of a blocker is therefore observable as clusters of openings and closings that are terminated by entry into long-lived desensitized states. In the presence of BPyneTEA, however, a cluster of activity may be terminated early by blockade (**Figure IV.3AB**). Blockade of either closed or open states might terminate a cluster.

Direct observation of individual BPyneTEA blockade events at the single-molecule level supports the hypothesis that this candidate probe binds both the open and closed states. Individual association rate constants were measured for BPyneTEA binding to both closed and open conformations. To determine the association rate constant for open-state blockade, the distribution of nAChR open durations was measured as a function of BPyneTEA concentration (**Figure IV.3C**). Blockade of the open state truncates open intervals within a cluster, decreasing the mean open time (*11, 56*) (**Figure IV.3D**). The association rate constant for open state blockade was determined from the BPyneTEA concentration-dependent decrease of the observed open time (*56*) and is $1.3\pm0.7 \times 10^6\ M^{-1} \cdot s^{-1}$ (mean ± standard error, nonlinear least squares fitting). The distribution of closed durations within a cluster was used to determine the association rate constant for BPyneTEA binding to the closed nAChR. Like open-state blockade, binding of BPyneTEA to the closed state is expected to truncate closings, decreasing the observed mean closed times (**Materials and Methods**). In this case, there are multiple kinetic components in the closed time distribution, but only one that decreases in a BPyneTEA-dependent fashion; this represents the lifetime of the closed, blocker-free state. The association rate constant for binding to the closed state was determined from the BPyneTEA concentration-dependent decrease of the fastest closed time component and is $5\pm2\times10^6\ M^{-1} \cdot s^{-1}$ (mean ± standard error, nonlinear least squares fitting) (**Figure IV.3E**). Both open and closed states thus bind BPyneTEA with an association rate constant of $\sim1\times10^6\ M^{-1}\ s^{-1}$; the difference in blockade rate constants between the open and closed states is not statistically significant (unpaired, two-sided t-test, $p=0.068$).

The affinity of BPyneTEA for the closed and open states can also be estimated from the single-channel measurements. The observation that BPyneTEA terminates clusters of activity (**Figure IV.3B**) shows that its average residence time in the channel is long compared to the normal closed and open states. The closed time kinetic component corresponding to the BPyneTEA-bound state(s) is therefore not expected to be directly observable among the closed components within a cluster of nAChR activity (**Materials and Methods**). Nonetheless, the

slowest component in the intracluster closed time distribution sets a lower limit on the true residence time of BPyneTEA; only BPyneTEA blockade events that are shorter than average can be observed within clusters of activity (**Materials and Methods**). The average duration of these intracluster blockade events (**Figure IV.3C**) can be used to put a lower limit on the residence of the candidate probe and an upper limit on the dissociation rate constant. This slow component has a mean time of ~10 ms, corresponding to a dissociation rate constant of ~100 s^{-1}. Using this dissociation rate constant as an upper limit, upper limits for the closed and open blockade dissociation constants can be obtained using the association rate constants: <~20 μM for the closed state and <~80 μM for the open state.

Electrophysiological Characterization: BPyneTEA Binds Within the Transmembrane Electrical Field

To estimate how BPyneTEA is situated in the transmembrane electric field when binding to the nAChR, we measured the voltage dependence of open-state blockade. For these experiments, single-channel currents from wild-type nAChRs activated by acetylcholine were recorded. This set of conditions both allows the observation of large numbers of channel openings and permits the open-state to be observed selectively. At low acetylcholine concentration (1 μM), the nAChR is open for >95% of the observed bursts (*57*). The observed open duration was measured as a function of both BPyneTEA concentration and transmembrane voltage, allowing the association rate constant to be measured as a function of voltage (**Figure IV.4**). The Woodhull model (*49*) (**Materials and Methods**), which describes channel pore interactions with charged blockers, defines an electrical distance ($0 \leq \delta_b \leq 1$) to the kinetic barrier for binding within the transmembrane electrical field. The more deeply this barrier resides within the transmembrane electric field, the more sensitive the association rate constant will be to transmembrane voltage (*49*) and the larger δ_b will be. The measured electrical distance is δ_b = 0.2 ± 0.1 (mean ± standard error). Assuming that blockade is due to binding within the open pore, and approximating the transmembrane field as uniform through the pore, this electrical distance corresponds to a barrier to blockade situated about 8 Å deep in a 40 Å channel pore. However, it is also possible that BPyneTEA blocks the nAChR by binding an allosteric site exterior to the pore within the transmembrane field.

State-Dependent Labeling of AChRs in Living Cells

To test whether BPyneTEA selectively labels the non-desensitized states of the nAChR compared to the inactive desensitized state, we carried out photolabeling of nAChRs expressed in live, intact HEK293 cells in the presence or absence of the desensitizing agonist acetylcholine. The results of the electrophysiological experiments described above indicate that BPyneTEA binds to both closed and open non-desensitized states. However, it is possible that the candidate probe also binds with appreciable affinity to desensitized nAChRs. Photolabeling using BPyneTEA was carried out on nAChR-expressing HEK-293 cells in the absence or presence of acetylcholine in order to determine the probe's selectivity for resting and desensitized states, respectively (**Figure IV.6**). Copper(I)-catalyzed [3+2] cycloaddition (i.e., "click" chemistry) of an azide-functionalized biotin was carried out to biotinylate the photolabeled ion channels (**Scheme IV.3**) (*9*). Biotinylated ion channels were captured on streptavidin-coated beads, and nAChRs were visualized by Western blotting with an antibody against the nAChR α-subunit. Quantification of the captured nAChRs (normalized for expression levels) shows that the resting state is labeled more efficiently than the desensitized state by a factor of 1.95 ± 0.37 (n=3, mean ± SD, p = 0.047 two-sided t-test) (**Figure IV.6A**). BPyneTEA is therefore a selective covalent label for closed, non-desensitized nAChRs.

Photolabeling at low probe concentrations is desirable in order to minimize the possibility of non-specific effects of the probe on cells. Experiments on the dose-dependence of BPyneTEA labeling show that labeling can be effective at BPyneTEA concentrations of <100 μM (**Figure IV.6B**). At a BPyneTEA concentration of 50 μM, selective labeling of closed, non-desensitized nAChRs is observed: a factor of 1.80 ± 0.26 (n=3, weighted mean ± SD, p = 0.034, two-sided t-test). The selectivity at the lower concentration is comparable to that observed at 250 μM BPyneTEA. At 10 μM BPyneTEA, weak labeling is observed, but its state selectivity is not statistically significant (1.24 ± 0.19, n=3, p = 0.16, two-sided t-test). Labeling was not observed in the absence of BPyneTEA or in the absence of UV irradiation (**Figure IV.6C**).

IV.E Discussion

Taken together, electrophysiological and covalent photolabeling results support the hypothesis that BPyneTEA binds selectively to the non-desensitized nAChR compared to the desensitized receptor. Single-channel current measurements show that BPyneTEA binds the

non-desensitized open and closed states with similar kinetics and affinities, while BPyneTEA is observed to photolabel the non-desensitized closed state with higher affinity than the desensitized state in whole cells. The results provide a proof of concept that BPyneTEA can be used for state-dependent labeling of non-desensitized nAChRs in live cells, and they suggest more broadly that ABPP can be applied to ion channel pores as it has been to enzyme active sites.

Covalent photolabeling is more efficient in the absence of acetylcholine, indicating that BPyneTEA can be used for selective covalent labeling of closed, non-desensitized nAChRs. Structural differences in the pore region may account for the differential labeling of resting and desensitized states (**Figure IV.7**). On the basis of electrophysiological (*28, 58*) and solvent accessibility (*26*) studies, the constriction in the pore (or "gate") that occludes ion access differs structurally for closed and desensitized states. The gate is deep within the pore in the closed state, but shallower and closer to the extracellular face of the membrane in the desensitized state. The results of the Woodhull analysis of the voltage-dependence of BPyneTEA open-channel blockade suggest that the dominant barrier to blockade is not far from the extracellular side of the channel. This observation provides a possible explanation for the similarity of blockade affinities in closed and open states and the lower affinity in the desensitized state compared to the closed state. If BPyneTEA binds within the nAChR transmembrane pore at a shallow site near the desensitization gate, then BPyneTEA binding to the non-desensitized states would be unobstructed by the closed-state gate, but constriction of the desensitization gate would disfavor binding to the desensitized state. The data do not rule out the possibility that the probe binds the open and/or closed channel outside the conduction pore. However, the hypothesis of shallow pore blockade provides a straightforward explanation for the observation that BPyneTEA rapidly binds both closed and open states of the channel. Further structural and functional studies will be required to test this hypothesis and determine which specific residues are labeled by BPyneTEA.

Selectivity for closed states compared to desensitized states is likely to be a crucial parameter in determining the utility of probes for investigation of nAChR desensitization *in vivo*. Because desensitization occurs primarily from the open state and is the thermodynamic minimum for the agonist-bound channel(*59*), only channel populations that spend most of their time in the closed state will remain activatable. For example, in the course of normal physiological stimuli, nAChRs at the neuromuscular junction are closed > 95% of the time (*57*).

One factor that could decrease selectivity for the closed state is binding of the probe to the nAChR at different sites in different channel conformations. Previous work has shown that benzophenone binds within the closed nAChR pore, but at non-pore sites in the desensitized nAChR (*36*). Optimization of the blocker and benzophenone moieties may allow improved selectivity for the closed state; the modular design of the molecule is expected to enable facile synthesis of second-generation probes.

Labeling with BPyneTEA and similar probes is expected to be compatible with the biological processes of interest. Four of the most important factors in evaluating the utility of the probe for biological experiments are accessibility of cells to the reagent, level of state-selectivity, timescale of the photochemical reaction, and protein selectivity of labeling. Like other techniques based on photochemistry, labeling with BPyneTEA is likely to be most useful for physiological preparations that can be thoroughly illuminated and perfused, such as neuronal cultures or thin brain slices. The selectivity of BPyneTEA for closed over desensitized conformations is modest (~ 2-fold), but high enough that comparison of subproteomes using mass spectrometry is expected to be feasible. The use of trypsin-catalyzed ^{18}O labeling of peptides for relative quantification of subproteomes by mass spectrometry (*60*) has allowed enrichments/depletions of < 2-fold to be detected (*61*). Photolabeling over tens of minutes is compatible with the timescales of many of the biological questions of greatest interest, such as long-term neuronal plasticity associated with nicotine addiction. In addition, this technology may be adaptable to faster timescales after further optimization, since benzophenone probes have been used to conduct structure-function studies of voltage-gated ion channels using sub-millisecond UV flashes (*62*) and of nAChRs using seconds-long UV exposures (*15*). Finally, although the relatively high extracellular concentration of BPyneTEA (50 μM) may lead to non-specific labeling of other channels or membrane proteins, selective detection of the target channel by Western blotting or mass spectrometry is expected to allow accurate target profiling even when off-target labeling is significant, as has previously been observed in ABPP studies (*2*).

IV.F Conclusions

The potential utility of a channel-targeted ABPP strategy depends on whether it will be generalizable to a large number of structurally distinct channels. Large changes in pore structure (as judged by accessibility to reactive probes in solution) have been observed for other Cys-Loop

receptors such as the serotonin receptor (*63*), as well as glutamate receptors (*64*), potassium channels (*65*), and sodium channels (*66*). Channel pores and surrounding regions typically contain both hydrophobic and charged groups (*27*), providing diverse functionality for interaction with small molecules. The single-molecule techniques available for direct observation of small molecule-channel interactions make testing state-dependent binding straightforward for a variety of channels. In addition, the many characterized state-selective channel blockers and inhibitors offer a rich set of potential pore-binding groups for ion channel-targeted ABPP probes. Ion channels as a class thus share many of the advantages of enzyme active sites as ABPP targets, and appear likely to be a generally useful target for ABPP techniques.

IV.G References

1. Jessani, N., and Cravatt, B. F. (2004) The development and application of methods for activity-based protein profiling. *Curr. Opin. Chem. Biol. 8*, 54-59.
2. Jessani, N., Liu, Y. S., Humphrey, M., and Cravatt, B. F. (2002) Enzyme activity profiles of the secreted and membrane proteome that depict cancer cell invasiveness. *Proc. Natl. Acad. Sci. U.S.A. 99*, 10335-10340.
3. Greenbaum, D. C., Baruch, A., Grainger, M., Bozdech, Z., Medzihradszky, K. F., Engel, J., DeRisi, J., Holder, A. A., and Bogyo, M. (2002) A role for the protease falcipain 1 in host cell invasion by the human malaria parasite,. *Science 298*, 2002-2006.
4. Barglow, K. T., and Cravatt, B. F. (2004) Discovering disease-associated enzymes by proteome reactivity profiling. *Chem. Biol. 11*, 1523-1531.
5. Liu, Y. S., Patricelli, M. P., and Cravatt, B. F. (1999) Activity-based protein profiling: The serine hydrolases. *Proc. Natl. Acad. Sci. U.S.A. 96*, 14694-14699.
6. Yee, M., Fas, S. C., Stohlmeyer, M. M., Wandless, T. J., and Cimprich, K. A. (2005) A cell-permeable, activity-based probe for protein and lipid kinases. *J. Biol. Chem. 280*, 29053-29059.
7. Salisbury, C. M., and Cravatt, B. F. (2008) Optimization of activity-based probes for proteomic profiling of histone deacetylase complexes. *J. Am. Chem. Soc. 130*, 2184-2194.
8. Hille, B. (2001) *Ion channels of excitable membranes*, 3rd ed., Sinauer, Sunderland, Mass.
9. Speers, A. E., Adam, G. C., and Cravatt, B. F. (2003) Activity-based protein profiling in vivo using a copper(I)-catalyzed azide-alkyne 3+2 cycloaddition. *J. Am. Chem. Soc. 125*, 4686-4687.
10. Chen, H. S. V., Pellegrini, J. W., Aggarwal, S. K., Lei, S. Z., Warach, S., Jensen, F. E., and Lipton, S. A. (1992) Open-Channel Block of N-Methyl-D-Aspartate (Nmda) Responses by Memantine - Therapeutic Advantage against Nmda Receptor-Mediated Neurotoxicity. *J. Neurosci. 12*, 4427-4436.
11. Neher, E., and Steinbach, J. H. (1978) Local anesthetics transiently block currents through single acetylcholine-receptor channels. *J. Physiol. 277*, 153-176.
12. Zhorov, B. S., and Tikhonov, D. B. (2004) Potassium, sodium, calcium and glutamate-gated channels: pore architecture and ligand action. *J. Neurochem. 88*, 782-799.
13. Jackson, A. C., and Bean, B. P. (2007) State-dependent enhancement of subthreshold a-type potassium current by 4-aminopyridine in Tuberomammillary nucleus neurons. *J. Neurosci. 27*, 10785-10796.
14. Chambers, J. J., Gouda, H., Young, D. M., Kuntz, I. D., and England, P. M. (2004) Photochemically knocking out glutamate receptors in vivo. *J. Am. Chem. Soc. 126*, 13886-13887.
15. Leite, J. F., Blanton, M. P., Shahgholi, M., Dougherty, D. A., and Lester, H. A. (2003) Conformation-dependent hydrophobic photolabeling of the nicotinic receptor: Electrophysiology-coordinated photochemistry and mass spectrometry. *Proc. Natl. Acad. Sci. U.S.A. 100*, 13054-13059.
16. Bixel, M. G., Krauss, M., Liu, Y., Bolognesi, M. L., Rosini, M., Mellor, I. S., Usherwood, P. N. R., Melchiorre, C., Nakanishi, K., and Hucho, F. (2000) Structure-activity relationship and site of binding of polyamine derivatives at the nicotinic acetylcholine receptor. *Eur. J. Biochem. 267*, 110-120.

17. White, B. H., and Cohen, J. B. (1992) Agonist-Induced Changes in the Structure of the Acetylcholine-Receptor M2 Regions Revealed by Photoincorporation of an Uncharged Nicotinic Noncompetitive Antagonist. *J. Biol. Chem. 267*, 15770-15783.
18. Akabas, M. H., Stauffer, D. A., Xu, M., and Karlin, A. (1992) Acetylcholine receptor channel structure probed in cysteine-substitution mutants. *Science 258*, 307-310.
19. Hashimoto, M., Liu, Y., Fang, K., Li, H. Y., Campiani, G., and Nakanishi, K. (1999) Preparation and biological properties of biotinylated PhTX derivatives. *Bioorg. Med. Chem. 7*, 1181-1194.
20. Quick, M. W., and Lester, R. A. J. (2002) Desensitization of neuronal nicotinic receptors. *J. Neurobiol. 53*, 457-478.
21. Giniatullin, R., Nistri, A., and Yakel, J. L. (2005) Desensitization of nicotinic ACh receptors: shaping cholinergic signaling, *Trends Neurosci. 28*, 371-378.
22. Sine, S. M., Quiram, P., Papanikolaou, F., Kreienkamp, H. J., and Taylor, P. (1994) Conserved Tyrosines in the Alpha-Subunit of the Nicotinic Acetylcholine-Receptor Stabilize Quaternary Ammonium Groups of Agonists and Curariform Antagonists. *J. Biol. Chem. 269*, 8808-8816.
23. Heidmann, T., Bernhardt, J., Neumann, E., and Changeux, J. P. (1983) Rapid Kinetics of Agonist Binding and Permeability Response Analyzed in Parallel on Acetylcholine-Receptor Rich Membranes from Torpedo-Marmorata. *Biochemistry 22*, 5452-5459.
24. Neubig, R. R., Boyd, N. D., and Cohen, J. B. (1982) Conformations of Torpedo Acetylcholine-Receptor Associated with Ion-Transport and Desensitization. *Biochemistry 21*, 3460-3467.
25. Corringer, P. J., Bertrand, S., Bohler, S., Edelstein, S. J., Changeux, J. P., and Bertrand, D. (1998) Critical elements determining diversity in agonist binding and desensitization of neuronal nicotinic acetylcholine receptors. *J. Neurosci. 18*, 648-657.
26. Wilson, G. G., and Karlin, A. (2001) Acetylcholine receptor channel structure in the resting, open, and desensitized states probed with the substituted-cysteine-accessibility method. *Proc. Natl. Acad. Sci. U.S.A. 98*, 1241-1248.
27. Tikhonov, D. B., Mellor, I. R., and Usherwood, P. N. R. (2004) Modeling noncompetitive antagonism of a nicotinic acetylcholine receptor. *Biophys. J. 87*, 159-170.
28. Leonard, R. J., Labarca, C. G., Charnet, P., Davidson, N., and Lester, H. A. (1988) Evidence That the M2 Membrane-Spanning Region Lines the Ion Channel Pore of the Nicotinic Receptor. *Science 242*, 1578-1581.
29. Unwin, N. (2005) Refined structure of the nicotinic acetylcholine receptor at 4 Å resolution. *J. Mol. Biol. 346*, 967-989.
30. Ji, D., Lape, R., and Dani, J. A. (2001) Timing and location of nicotinic activity enhances or depresses hippocampal synaptic plasticity. *Neuron 31*, 131-141.
31. Mansvelder, H. D., Keath, J. R., and McGehee, D. S. (2002) Synaptic mechanisms underlie nicotine-induced excitability of brain reward areas. *Neuron 33*, 905-919.
32. Wang, H., and Sun, X. L. (2005) Desensitized nicotinic receptors in brain. *Brain Res. Rev. 48*, 420-437.
33. Elenes, S., Ni, Y., Cymes, G. D., and Grosman, C. (2006) Desensitization contributes to the synaptic response of gain-of-function mutants of the muscle nicotinic receptor. *J. Gen. Physiol. 128*, 615-627.
34. Salisbury, C. M., and Cravatt, B. F. (2007) Activity-based probes for proteomic profiling of histone deacetylase complexes. *Proc. Natl. Acad. Sci. U.S.A. 104*, 1171-1176.

35. Dorman, G., and Prestwich, G. D. (1994) Benzophenone Photophores in Biochemistry. *Biochemistry 33*, 5661-5673.
36. Garcia, G., Chiara, D. C., Nirthanan, S., Hamouda, A. K., Stewart, S., and Cohen, J. B. (2007) [H-3]Benzophenone photolabeling identifies state-dependent changes in nicotinic acetylcholine receptor structure. *Biochemistry 46*, 10296-10307.
37. Akk, G., and Steinbach, J. H. (2003) Activation and block of mouse muscle-type nicotinic receptors by tetraethylammonium. *J. Physiol. 551*, 155-168.
38. Salamone, F. N., Zhou, M., and Auerbach, A. (1999) A re-examination of adult mouse nicotinic acetylcholine receptor channel activation kinetics. *J. Physiol. 516*, 315-330.
39. Hamill, O. P., Marty, A., Neher, E., Sakmann, B., and Sigworth, F. J. (1981) Improved Patch-Clamp Techniques for High-Resolution Current Recording from Cells and Cell-Free Membrane Patches. *Pflug. Arch. 391*, 85-100.
40. Sine, S. M., Ohno, K., Bouzat, C., Auerbach, A., Milone, M., Pruitt, J. N., and Engel, A. G. (1995) Mutation of the Acetylcholine-Receptor Alpha-Subunit Causes a Slow-Channel Myasthenic Syndrome by Enhancing Agonist Binding-Affinity. *Neuron 15*, 229-239.
41. Qin, F. (2004) Restoration of single-channel currents using the segmental k-means method based on hidden Markov modeling. *Biophys. J. 86*, 1488-1501.
42. Qin, F., Auerbach, A., and Sachs, F. (1996) Estimating single-channel kinetic parameters from idealized patch-clamp data containing missed events. *Biophys. J. 70*, 264-280.
43. Qin, F., Auerbach, A., and Sachs, F. (1996) Idealization of single-channel currents using the segmental K-means method. *Biophys. J. 70*, Mp432-Mp432.
44. Qin, F., Auerbach, A., and Sachs, F. (1997) Maximum likelihood estimation of aggregated Markov processes. *Proceedings 264*, 375-383.
45. Qin, F., and Li, L. (2004) Model-based fitting of single-channel dwell-time distributions. *Biophys. J. 87*, 1657-1671.
46. Qin, F., Auerbach, A., and Sachs, F. (1996) Estimating single-channel kinetic parameters from idealized patch-clamp data containing missed events. *Biophys. J. 70*, 264-280.
47. Qin, F., Auerbach, A., and Sachs, F. (1997) Maximum likelihood estimation of aggregated Markov processes. *Proc. Roy. Soc. Lond. B Bio. 264*, 375-383.
48. Auerbach, A., Sigurdson, W., Chen, J., and Akk, G. (1996) Voltage dependence of mouse acetylcholine receptor gating: Different charge movements in di-, mono- and unliganded receptors. *J. Physiol. 494*, 155-170.
49. Woodhull, A. M. (1973) Ionic Blockage of Sodium Channels in Nerve. *J. Gen. Physiol. 61*, 687-708.
50. Keller, S. H., Kreienkamp, H. J., Kawanishi, C., and Taylor, P. (1995) Molecular Determinants Conferring Alpha-Toxin Resistance in Recombinant DNA-Derived Acetylcholine-Receptors. *J. Biol. Chem. 270*, 4165-4171.
51. Gallagher, S. R. (1999) Analysis of Proteins, in *Short Protocols in Molecular Biology* (Ausubel, F. M., Brent, R., Kingston, R. E., Moore, D. D., Seidman, J. G., Smith, J. A., and Struhl, K., Eds.) Fourth Edition ed., pp 10-10, John Wiley & Sons, Inc., New York.
52. Speers, A. E., and Cravatt, B. F. (2004) Profiling enzyme activities in vivo using click chemistry methods. *Chem. Biol. 11*, 535-546.
53. Arias, H. R., Bhumireddy, P., and Bouzat, C. (2006) Molecular mechanisms and binding site locations for noncompetitive antagonists of nicotinic acetylcholine receptors. *Int. J. Biochem. Cell. B 38*, 1254-1276.

54. Zhou, M., Engel, A. G., and Auerbach, A. (1999) Serum choline activates mutant acetylcholine receptors that cause slow channel congenital myasthenic syndromes. *Proc. Natl. Acad. Sci. U.S.A. 96*, 10466-10471.
55. Grosman, C., and Auerbach, A. (2000) Asymmetric and independent contribution of the second transmembrane segment 12′ residues to diliganded gating of acetylcholine receptor channels: a single-channel study with choline as the agonist. *J. Gen. Physiol. 115*, 637-651.
56. Colquhoun, D., and Hawkes, A. G. (1995) The principles of the stochastic interpretation of ion channel mechanisms, in *Single-Channel Recording* (Sakmann, B., and Neher, E., Eds.), pp 397-482, Plenum Press, New York.
57. Edmonds, B., Gibb, A. J., and Colquhoun, D. (1995) Mechanisms of Activation of Muscle Nicotinic Acetylcholine-Receptors and the Time-Course of End-Plate Currents, *Ann. Rev. Physiol. 57*, 469-493.
58. Purohit, Y., and Grosman, C. (2006) Block of muscle nicotinic receptors by choline suggests that the activation and desensitization gates act as distinct molecular entities, *J. Gen. Physiol. 127*, 703-717.
59. Auerbach, A., and Akk, G. (1998) Desensitization of mouse nicotinic acetylcholine receptor channels - A two-gate mechanism, *J. Gen. Physiol. 112*, 181-197.
60. Yao, X. D., Freas, A., Ramirez, J., Demirev, P. A., and Fenselau, C. (2001) Proteolytic O-18 labeling for comparative proteomics: Model studies with two serotypes of adenovirus. *Anal. Chem. 73*, 2836-2842.
61. Ramos-Fernandez, A., Lopez-Ferrer, D., and Vazquez, J. (2007) Improved method for differential expression proteomics using trypsin-catalyzed O-18 labeling with a correction for labeling efficiency. *Mol. Cell. Proteomics. 6*, 1274-1286.
62. Ding, S., and Horn, R. (2001) Slow photo-cross-linking kinetics of benzophenone-labeled voltage sensors of ion channels. *Biochemistry 40*, 10707-10716.
63. Panicker, S., Cruz, H., Arrabit, C., and Slesinger, P. A. (2002) Evidence for a centrally located gate in the pore of a serotonin-gated ion channel. *J. Neurosci. 22*, 1629-1639.
64. Sobolevsky, A. I., Beck, C., and Wollmuth, L. P. (2002) Molecular Rearrangements of the extracellular vestibule in NMDAR channels during gating. *Neuron 33*, 75-85.
65. Liu, Y., Jurman, M. E., and Yellen, G. (1996) Dynamic rearrangement of the outer mouth of a K+ channel during gating. *Neuron 16*, 859-867.
66. Yang, N. B., George, A. L., and Horn, R. (1996) Molecular basis of charge movement in voltage-gated sodium channels. *Neuron 16*, 113-122.

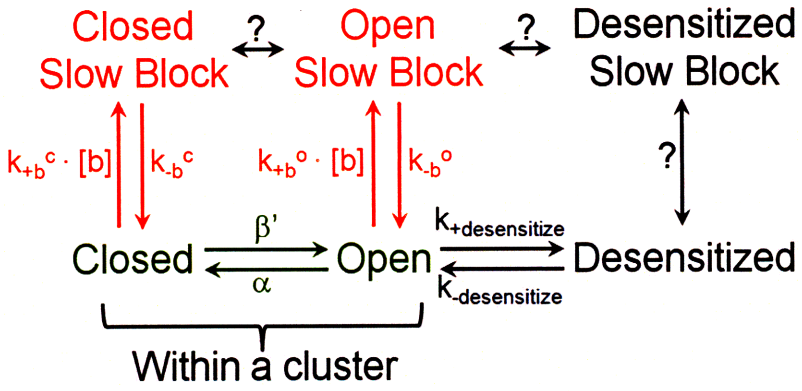

Scheme IV.1. A kinetic model describe BPyneTEA block of the AChR. Using clustered single-channel activity, we can determine if BPyneTEA blocks the closed state and if BPyneTEA blocks the open state. Rate constants: $k_{+b}^{c(o)}$, block association rate constant to the closed (open) state, M^{-1} s^{-1}; β', channel opening; α, channel closing; $k_{+desensitize}$, desensitization; $k_{-desensitize}$, recovery from desensitization.

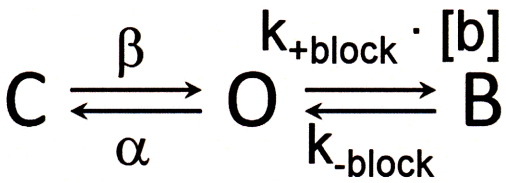

Scheme IV.2. A kinetic model for only open-channel block. Using unclustered single-channel activity, we can quantify open-channel block and its voltage dependence, but we cannot interpret closed event unambiguously. "C", closed; "O", open; "B", block; [b], BPyneTEA concentration.

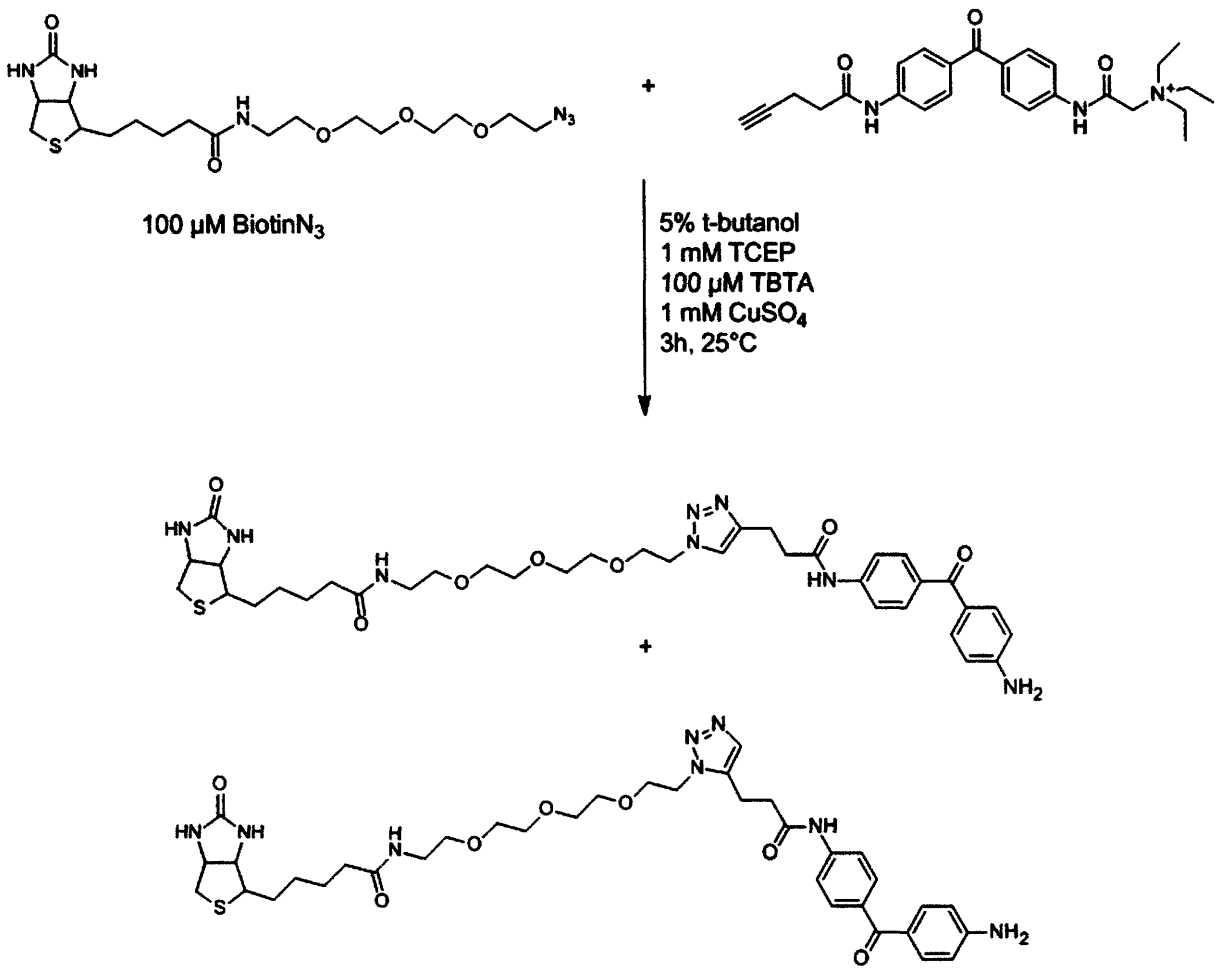

Scheme IV.3. Click reaction between BPyneTEA and the biotin-azide reagent.

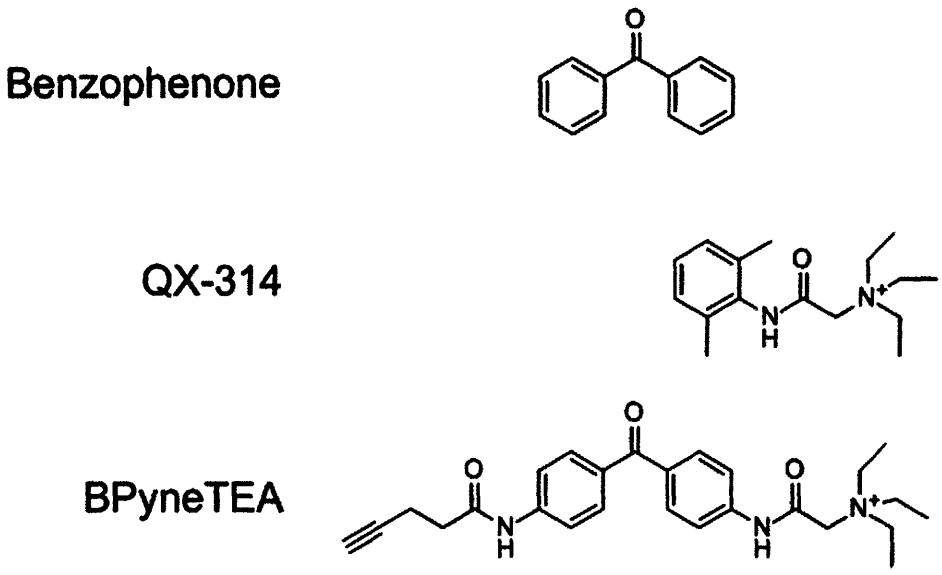

Figure IV.1. The structure of the candidate probe BPyneTEA synthesized in this study compared to the structurally related blockers benzophenone and QX-314.

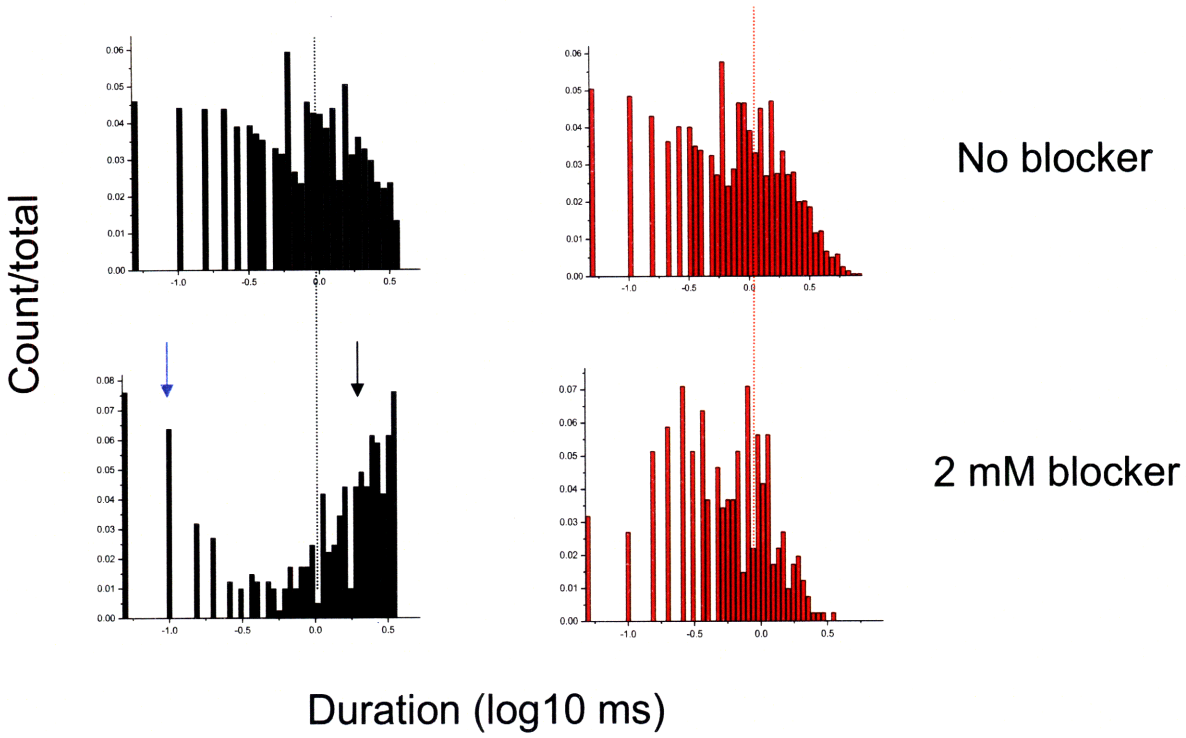

Figure IV.2. Simulated effect of slow closed-channel block on the intracluster closed dwell-time distribution. Closed (left) and open (right) dwell-time distributions are shown. Dotted lines mark the mean closed and open times in the absence of blocker. Blue arrow: short closed component. Black arrow: long closed component due to blockade events.

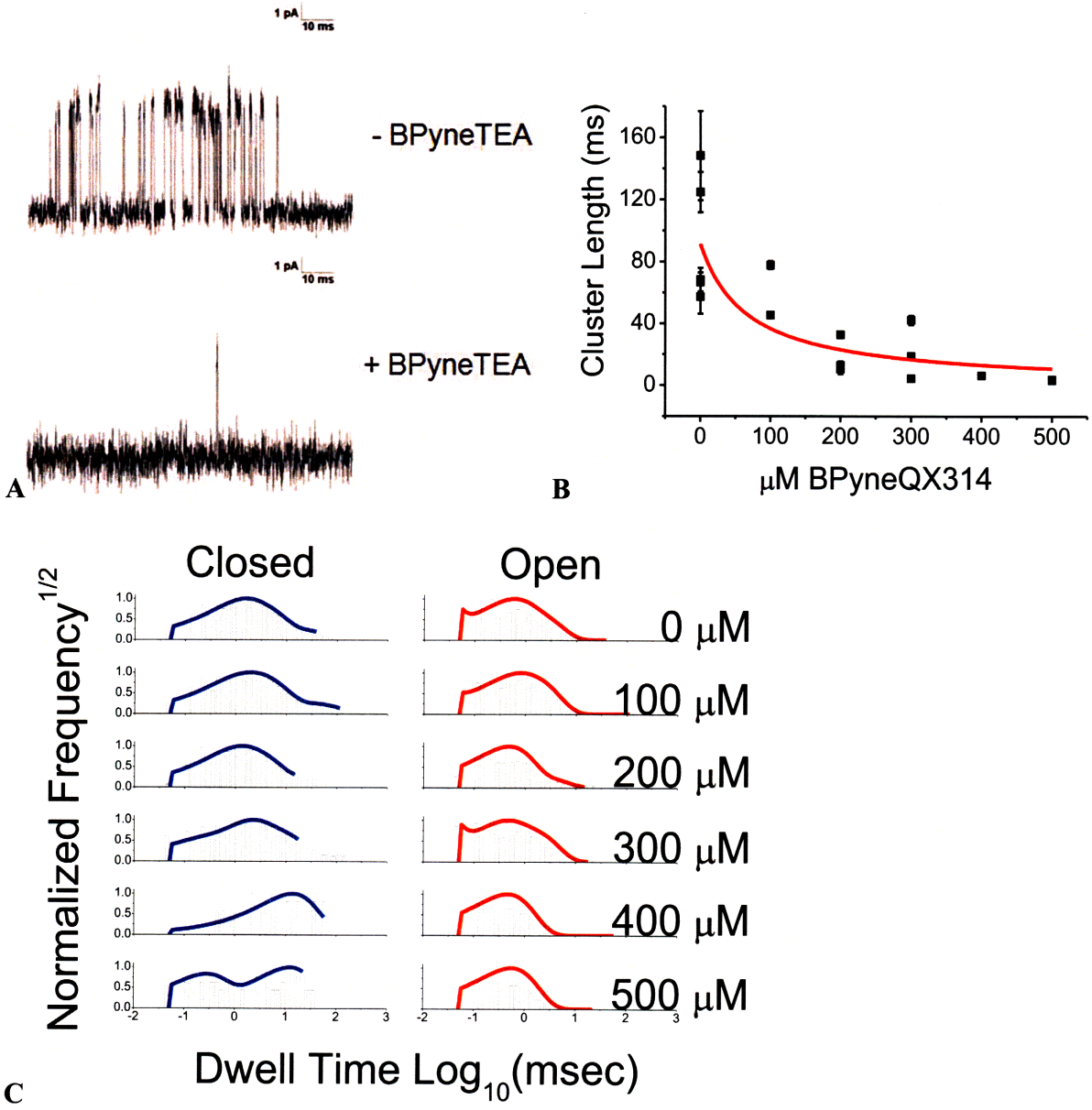

Figure IV.3. BPyneTEA blocks both closed and open nAChRs. (A) Single-channel currents from αG153S nAChRs activated by choline (1 mM) in the absence (top) or presence (bottom) of BPyneTEA (500 μM). (B) BPyneTEA blockade terminates clusters of openings. (c) Histograms of intracluster closed (left) and open (right) duration distributions as a function of BPyneTEA concentration. (continued next page)

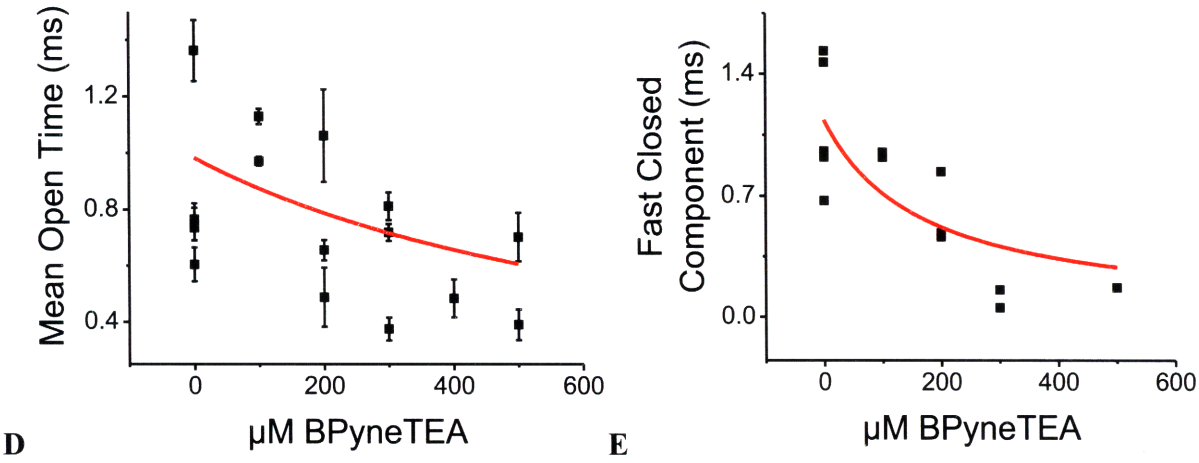

Figure IV.3 (continued). BPyneTEA blocks both closed and open nAChRs. (D) BPyneTEA induces a decrease in mean intracluster open times, indicating open-state binding. (E) BPyneTEA induces a decrease in the mean lifetime of a short-duration closed time component, indicating closed-state binding.

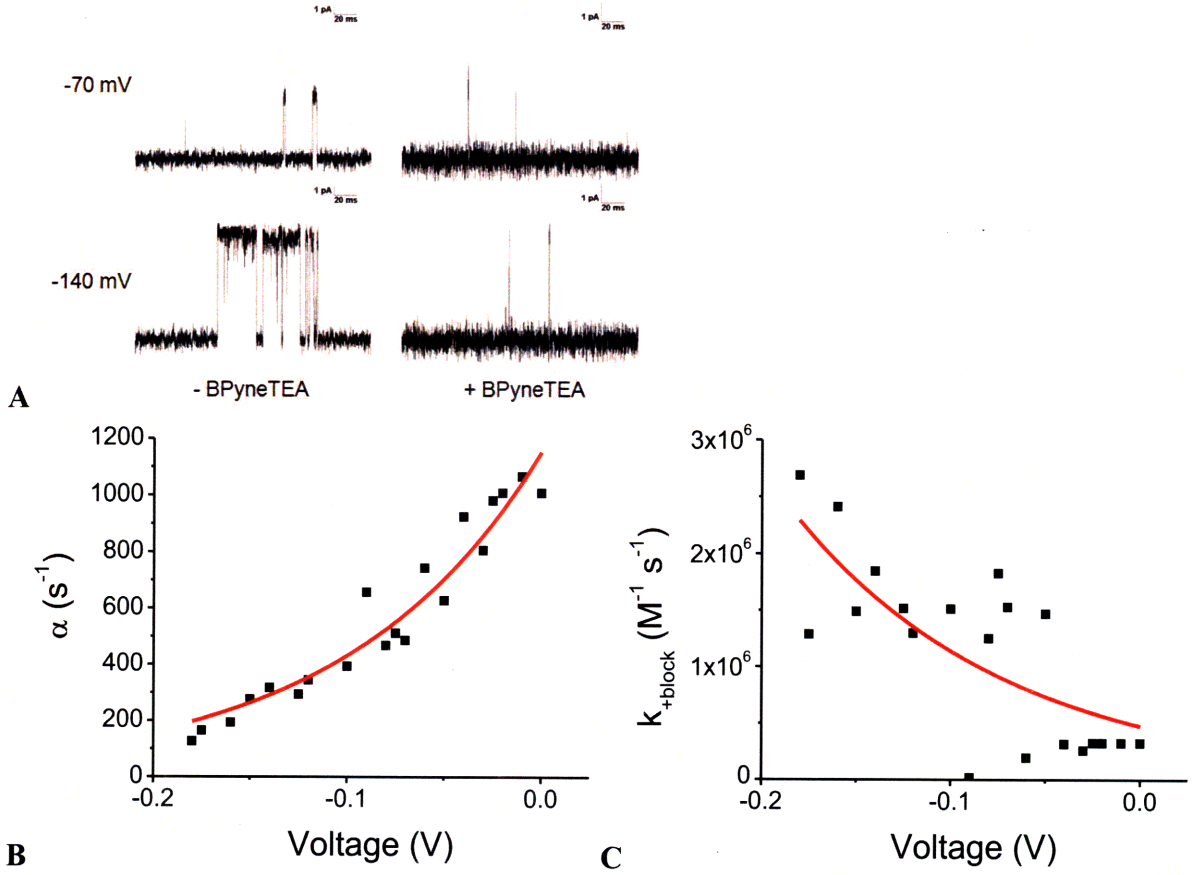

Figure IV.4. The transmembrane electric field affects BPyneTEA binding. (A) Single-channel currents from wild-type nAChRs activated by acetylcholine (1 μM) in the presence of BPyneTEA (500 mM) at -70 mV (top) and -140 mV (bottom). Hyperpolarization increases the rate of blockade. (B) The voltage dependence of α: $\alpha_0 = 1150 \pm 50\ s^{-1}$, $\delta_\alpha = 0.25 \pm 0.02$ (mean ± standard error from nonlinear least squares fitting). (C) Voltage dependence of the association rate constant for TEA blockade: $k_{+block}^{0} = 5 \pm 1 \times 10^5\ M^{-1} \cdot s^{-1}$, $\delta_{block} = 0.2 \pm 0.1$. The sensitivity of the association rate constant to voltage corresponds to the charged blocker being influenced by 20 ± 10% of the total transmembrane electric field.

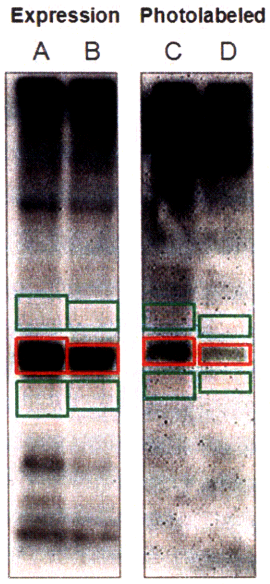

Figure IV.5. Densitometry and normalization of Western Blots. An example blot of samples tested at 250 μM BPyneTEA. Blots were probed with an primary anti-AChR α subunit mouse antibody, followed by a secondary anti-mouse goat antibody with conjugated horseradish peroxidase. Chemiluminescence was used for signal detection. The pixel densities of AChR α subunit bands (red boxes) were background subtracted using regions of interest of equal area above and below the band (green boxes). Bands representing photolabeling levels were normalized to the level of AChR expression: absence of acetylcholine (closed channels), lane C divided by lane A; presence of acetylcholine (desensitized receptors), lane D divided by lane B.

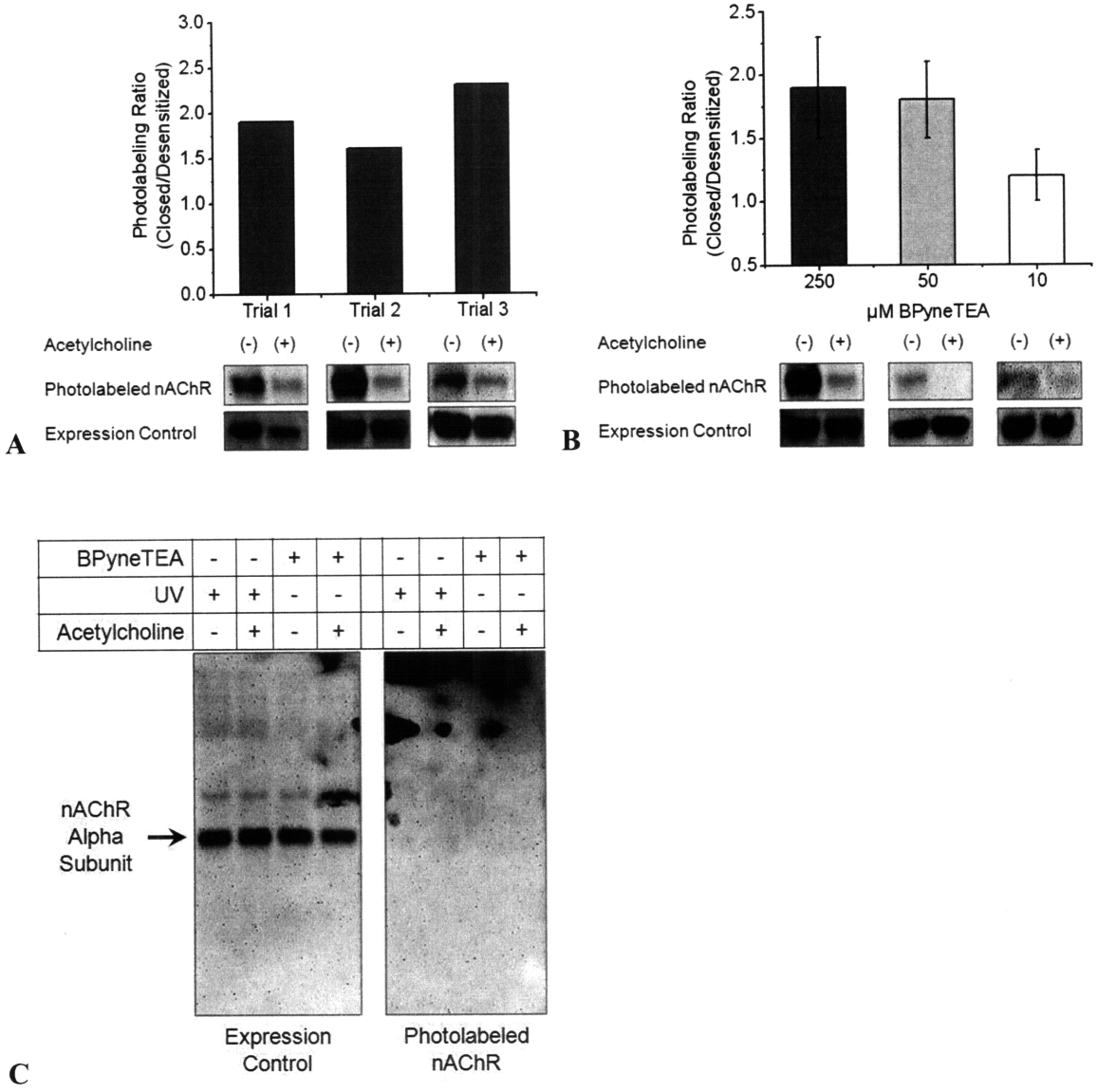

Figure IV.6. State-dependent photolabeling of nAChRs in live cells. (A) Closed nAChRs (absence of acetylcholine) were labeled two-fold more efficiently than desensitized nAChRs (presence of acetylcholine) using 250 μM BPyneTEA. (B) Using either 250 or 50 μM BPyneTEA, closed nAChRs were labeled two-fold more efficiently than desensitized nAChRs. At 10 μM BPyneTEA, no difference could be detected. Bars are means of three trials, error bars are standard errors. (C) Control experiments in the absence of UV or BPyneTEA did not show photolabeling.

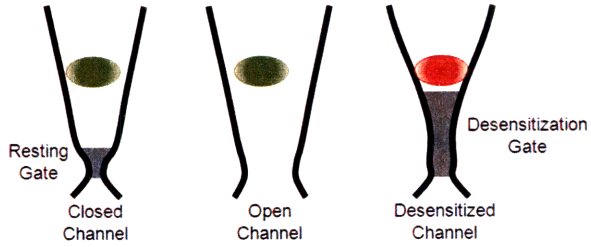

Figure IV.7. A hypothesis for a binding site within the channel pore, explaining BPyneTEA blockade characteristics. Additional study is required to determine the actual locus because the block by BPyneTEA could occur by an allosteric mechanism rather than direct occlusion of the ion conduction pathway. Black lines, AChR pore lining; green ovals, BPyneTEA able to block; red oval, BPyneTEA block is inhibited by structural changes near the desensitization gate.

Mathew C. Tantama

Education

Massachusetts Institute of Technology — Cambridge, MA
Ph.D. Candidate, Department of Chemistry

University of North Carolina at Chapel Hill — Chapel Hill, NC
B.S., Chemistry and B.S., Mathematics, 2001

Research Experience

MIT Department of Chemistry — Cambridge, MA
Graduate Research Assistant (2003 – 2008)
Thesis Advisor: Professor Stuart Licht

MIT Lincoln Laboratory Biodefense Systems Group — Lexington, MA
Assistant Staff (2001 – 2003)
Supervisors: Dr. Bernadette Johnson, Dr. Christina Rudzinski

UNC Program for Molecular Biology and Biotechnology — Chapel Hill, NC
Undergraduate Technician (1999 – 2001)
Principal Investigator: Professor Terry Van Dyke

GlaxoWellcome Virology Department — RTP, NC
Summer Intern (1999, 2000)
Supervisor: Dr. Phiroze Sethna

Miami Project to Cure Paralysis, UM Medical School — Miami, FL
Summer Intern (1997, 1998)
Principal Investigator: Professor John Bethea

Publications

"Testing for Violations of Microscopic Reversibility in ATP-Sensitive Potassium Channel Gating." K.-H. Choi, M. Tantama, S. Licht. *J. Phys. Chem. B. Accepted.*

"$p19^{ARF}$ is Dispensable for Oncogenic Stress-Induced p53-Mediated Apoptosis and Tumor Suppression In Vivo." D. Tolbert, X. Lu, C. Yin, M. Tantama, T. Van Dyke. *Molecular and Cellular Biology*. 2002. 22, 370 - 7.

Teaching Experience

MIT Department of Chemistry — Cambridge, MA
Teaching Assistant (2003 – 2004)

Honors

National Defense Science and Engineering Graduate Fellow 2004 – 2007
Outstanding Teaching Assistant, 2004
MIT Robert T. Haslam Presidential Graduate Fellow, 2003 – 2004
MIT Lincoln Laboratory Team Excellence Award, 2003
Barry M. Goldwater Scholarship, 1999 – 2001
UNC James Johnston Scholarship, 1997 – 2001
Phi Beta Kappa National Honor Society
Pi Mu Epsilon National Mathematics Honor Society